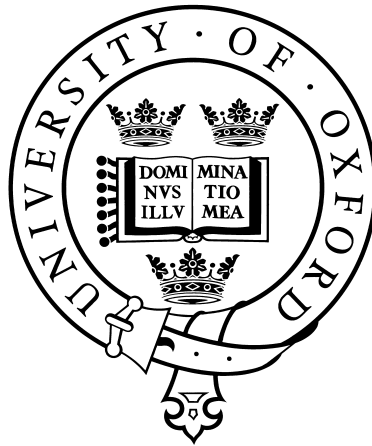


# Generation of Heralded Single Photons in Pure Quantum States

Peter J. Mosley  
Hertford College, Oxford



Submitted for the degree of Doctor of Philosophy  
Trinity Term 2007

Supervised by  
Prof. Ian A. Walmsley

Clarendon Laboratory  
University of Oxford  
United Kingdom



To my parents, Cathy and Jim

*sine qua non*



# Generation of Heralded Single Photons in Pure Quantum States

Peter J. Mosley  
Hertford College, Oxford

Submitted for the degree of Doctor of Philosophy  
Trinity Term 2007

## Abstract

Single photons — discrete wavepackets of light — are one of the most fundamental entities in physics. In recent years, the ability to consistently create and manipulate both single photons and pairs of photons has facilitated everything from tests of quantum theory to the implementation of quantum-enhanced precision measurements. These activities all fall within the scope of the rapidly-growing field of quantum information — the exploitation of the properties of quantum states (and specifically their capability to exist in superpositions) to accomplish tasks that would not be possible with classical objects.

One stated goal of research in quantum information is to build a device consisting of a network of quantum logic gates that can evaluate quantum algorithms. The photonic implementation of individual logic gates has already been demonstrated. However, partly due to standard methods of preparing single photons, current schemes have severe limitations in terms of scaling up from a single logic gate to multiple concatenated operations. Until now it has not been proven that single photons can be generated in pure and indistinguishable quantum states, something upon which the successful operation of optical quantum logic gates relies.

This thesis presents an experimental demonstration of simultaneous generation of almost identical single photons in highly pure states from two independent sources based on parametric downconversion. This is a process of photon pair generation during the passage of a light beam through a nonlinear crystal; one photon from the resulting pair is detected to herald the other. The work herein describes, refines, and implements a technique that minimises the strong quantum correlations usually present within each pair by spectral engineering of the source. This allows the heralded single photons to be in pure states, a property that is confirmed by observing a high-visibility two-photon interference effect without spectral filtering.



## Acknowledgements

This thesis and the work that it contains would not have been possible without the support and guidance provided by those around me, and especially by my supervisor, Prof. Ian Walmsley. Firstly, I would like to thank him wholeheartedly for giving me the opportunity to be a member of his research group and benefit from his vast knowledge and seemingly limitless intellect. The last four years have been not only extremely interesting and a great learning experience, but also very enjoyable! There are several other things that I am grateful to Ian for, among them his uncanny ability to find grant money with which to pay students, the fact that he can take a joke (“A Physics Carol” springs to mind...), and the fantastic group of people that he has always managed to assemble to work on an exciting array of projects.

This brings me to my second vote of thanks, to all the postdocs that I have worked with over the years of my D.Phil. Upon my arrival in the group Christine Silberhorn was a brilliant mentor and helped me to get things under way at the beginning of the project. Subsequently, Piotr Wasylczyk taught me everything I know about titanium:sapphire oscillators and amplifiers — I hope that one day I might be as good at lab work as he is! Over the past year or so it has been a pleasure to work with Jeff Lundeen, and during the last six months Brian Smith, both of whom have given me invaluable advice on all things quantum mechanical. I hope that the KDP sources continue to give you good service after I have gone! I must also mention Rob Davies — it was a fun to sit next to you and listen to your musings on the double slit experiment, and thanks for introducing me to “the trampoline” as a physical concept!

Thirdly I would like to thank all the Ultrafast Group members who have helped me and kept me going during my degree. Initially the Rochester students, especially Alfred U'Ren for taking the time to teach me about downconversion and the idea of factorable state generation in KDP, Laura Corner for getting the new lab up and running, and the first Oxford Ultrafast students, Matthijs (your trousers are not red!) and Daryl (even though you're not a real physicist any more Achilles!). My own cohort, Lijian for putting up with my constant habit of stealing his CCD camera, Alex for the librarian, and Adam for laughing at my attempts to write Matlab code even half as good as his. The Walmsley Empire is now too large to mention everyone (we all used to fit in one office, honest!), but my thanks go to all of you. A few special mentions: Josh for tea and a better Jeremy Clarkson accent than the man himself, Hendrik — thanks for keeping me entertained in Torino and

good luck with your experiments making use of the pure photons, Felix for nearly asphyxiating me while on the skiing trip, Tobi for coffee and your pink T-shirt, Phil for getting take-away last night (“I will not rest!”), and Offir for his boundless enthusiasm — I hope the factorable states from fibre work out for you, just don’t get too excited about it.

Hertford College has been a massive part of my life for the last eight years, and the MCR for the latter half of that. I think I owe what remains of my sanity to the bar, the tea room, the choir, and the football team — thanks to everyone who has been part of any or all of the above. Particular thanks go to Ryan (“It’s not even funny any more!” Actually, it was), Dave (the most entertaining MCR president by far, enjoy counting the beans), Rude Adam (I’m glad you never made me cry), Bruce (hopefully I’ll make it to Toronto again soon!), PJ (the best footballer ever, as long as it rains. Really hard), Steve (enjoy Neighbours), Sarah, Lisa, Corin, Marina, Beast (for being at Hertford longer than me!), and others too numerous to mention. Thanks to all the residents of 3, Chester Street. It was a fun place to live for two years.

Extra special thanks go to Gemma for being there for the last two years. I hope I haven’t been too difficult to live with over the last few weeks!

Finally, my eternal gratitude goes to my parents, to whom this thesis is dedicated, and the rest of my family. Thanks for giving me the best possible start in life — if it weren’t for you I would not be where I am today. I am especially grateful to you for nurturing in me the interest in physics that has inspired me along the way and I’m sure will continue to do so in the future.

# Contents

<b>1</b>	<b>Introduction</b>	<b>1</b>
1.1	Overview and motivation . . . . .	1
1.2	What is a photon? . . . . .	3
1.3	Pure states and mixed states . . . . .	8
1.4	An ideal single photon source: The photon gun . . . . .	9
1.5	Methods of single photon generation . . . . .	10
1.5.1	Single emitters . . . . .	11
1.5.2	Multiple emitters . . . . .	14
1.6	Parametric downconversion . . . . .	17
1.7	Quantum correlations in PDC . . . . .	23
1.8	Hong-Ou-Mandel interference . . . . .	25
1.9	The state of the art in photonic QIP . . . . .	31
1.10	Thesis outline . . . . .	33
<b>2</b>	<b>Parametric Downconversion</b>	<b>37</b>
2.1	Theory of parametric downconversion . . . . .	40

---

2.2	Phasematching in birefringent media . . . . .	47
2.2.1	The physics of phasematching . . . . .	48
2.2.2	More complex phasematching conditions . . . . .	54
2.3	The form of the two-photon state . . . . .	60
2.3.1	Type-I phasematching . . . . .	63
2.3.2	Type-II phasematching . . . . .	64
<b>3</b>	<b>Two-Photon State Engineering</b>	<b>67</b>
3.1	Factorability and purity . . . . .	73
3.1.1	A brief note on notation . . . . .	76
3.2	Calculating photon pair correlations . . . . .	77
3.2.1	The Schmidt decomposition . . . . .	77
3.2.2	The singular value decomposition . . . . .	79
3.3	Correlated two-photon states and filtering . . . . .	80
3.4	Generation of factorable states . . . . .	87
3.4.1	KDP and factorable two-photon states . . . . .	101
3.4.2	Additional methods of group velocity matching . . . . .	104
<b>4</b>	<b>Experimental Demonstration of Factorable State Generation</b>	<b>107</b>
4.1	Experimental factors affecting factorability . . . . .	112
4.1.1	Pump focusing . . . . .	112
4.1.2	Fibre coupling collection angle . . . . .	120
4.1.3	Spatial chirp . . . . .	123

---

4.2	Numerical modelling . . . . .	126
4.2.1	Measurements of angular distributions . . . . .	131
4.2.2	Results of the model . . . . .	137
4.3	Joint spectral measurements . . . . .	146
4.4	Second order coherence measurement . . . . .	158
<b>5</b>	<b>Multiple source interferometry: A purity test</b>	<b>165</b>
5.1	Twin-source HOMI calculation . . . . .	166
5.2	Resolving distinguishability and purity . . . . .	173
5.3	Twin-source HOMI experiment . . . . .	176
5.3.1	Experimental apparatus . . . . .	176
5.3.2	Alignment procedure . . . . .	181
5.3.3	Mode matching and marginal spectra . . . . .	184
5.3.4	Interference of e-ray photons . . . . .	190
5.3.5	Interference of o-ray photons . . . . .	191
5.4	Heralding efficiency . . . . .	193
<b>6</b>	<b>Conclusion</b>	<b>197</b>
6.1	Summary . . . . .	198
6.2	Outlook . . . . .	201
6.2.1	Future work with the KDP sources . . . . .	201
6.2.2	Factorable state generation in other media . . . . .	206
<b>A</b>	<b>A recipe for purity</b>	<b>213</b>



# List of Figures

1.1	A schematic representation of type-II parametric downconversion . . .	18
1.2	Definitions of e-ray and o-ray polarisations in a nonlinear crystal . . .	20
1.3	An illustration of the variation of e- and o-ray refractive indices in a birefringent crystal . . . . .	21
1.4	Emission patterns for different types of PDC . . . . .	22
1.5	An illustration of the input and output modes of a beamsplitter . . .	26
1.6	A pictorial representation of single photon interference at a 50:50 beamsplitter . . . . .	29
1.7	A Hong-Ou-Mandel interference dip . . . . .	31
2.1	Collinear phasematching in a crystal without either dispersion or bire- fringence . . . . .	51
2.2	Phasematching in a crystal with normal dispersion but without bire- fringence . . . . .	52
2.3	Phasematching in a crystal with both normal dispersion and birefrin- gence . . . . .	53

2.4	Collinear type-I phasematching in a negative uniaxial crystal . . . . .	57
2.5	Collinear type-II phasematching in a negative uniaxial crystal . . . . .	58
2.6	Noncollinear type-II phasematching in a negative uniaxial crystal . . . . .	59
2.7	Intensity distributions of various pump functions . . . . .	62
2.8	Collinear type-I phasematching in BBO . . . . .	64
2.9	Collinear type-II phasematching in BBO . . . . .	65
3.1	Demonstration of the effects of filtering only the e-ray from a collinear type-II BBO PDC source . . . . .	84
3.2	Demonstration of the effects of filtering both arms of a collinear type- II BBO PDC source . . . . .	85
3.3	Factorable state generation in BBO . . . . .	97
3.4	Magnitudes of the first eight Schmidt coefficients for two approximate states generated by collinear type II BBO . . . . .	101
3.5	Factorable state generation in KDP . . . . .	103
3.6	Magnitudes of the first eight Schmidt coefficients for the approximate state generated by collinear type II KDP pumped at 415 nm . . . . .	104
4.1	The effects of truncating the wavevector mismatch on the exponential approximation to the joint state . . . . .	108
4.2	Exact state for collinear type-II KDP . . . . .	110
4.3	Illustration of spatial and temporal walkoff during collinear downcon- version in KDP . . . . .	114

---

4.4	Illustration of focusing in a Gaussian beam . . . . .	116
4.5	Change in degenerate collinear phasematching wavelength with angle in KDP . . . . .	117
4.6	Pump focusing angles . . . . .	118
4.7	Illustration of how changing the pump angle of noncollinear KDP affects the phasematching function . . . . .	119
4.8	Noncollinear output angles . . . . .	121
4.9	Illustration of how changing the e-ray emission angle of noncollinear KDP affects the phasematching function . . . . .	122
4.10	Illustration of how pump spatial chirp can affect the joint spectrum in the case of a focused pump in KDP . . . . .	125
4.11	Definition of angles in the numerical model . . . . .	128
4.12	Pump beam data and associated intensity distribution . . . . .	132
4.13	Spatial chirp data . . . . .	134
4.14	Collected mode data and associated intensity distribution . . . . .	137
4.15	Predicted joint spectral intensities for a range of pump and collection angles for positive spatial chirp . . . . .	142
4.16	Predicted joint spectral intensities for a range of pump and collection angles for negative spatial chirp . . . . .	143
4.17	Numerical optimisation plots for pump centre wavelength and FWHM pump angle against spatial chirp . . . . .	144

---

4.18 Numerical optimisation plots for crystal length against central phase-matching angle . . . . .	145
4.19 Apparatus for measurement of joint spectra . . . . .	149
4.20 Data demonstrating the resolutions of the two spectrometers . . . . .	151
4.21 Calibration data for the spectrometers . . . . .	152
4.22 Numerically calculated joint spectra alongside measured joint probability distributions . . . . .	154
4.23 Correlation between e- and o-ray photons from measured spectra . . . . .	156
4.24 Correlation between e- and o-ray photons from calculated spectra . . . . .	156
4.25 Temporal structure of the two-photon state . . . . .	157
4.26 Marginal distributions of measured joint spectra . . . . .	159
4.27 Apparatus for $g^{(2)}(0)$ measurement . . . . .	163
5.1 Schematic representation of the twin-crystal HOMI experiment . . . . .	167
5.2 Interference dips plotted for pure heralded photons . . . . .	171
5.3 Dependence of HOMI visibility on beamsplitter reflectivity . . . . .	173
5.4 Apparatus for two-crystal HOMI experiment . . . . .	178
5.5 Twofold interference effect . . . . .	189
5.6 Data for alignment interference used in HOMI experiment . . . . .	190
5.7 Interference of the unfiltered heralded e-ray photons . . . . .	192
5.8 Spectral overlap of two e-ray photons . . . . .	193
5.9 Interference of the unfiltered heralded o-ray photons . . . . .	194

# Chapter 1

## Introduction

### 1.1 Overview and motivation

Ever since its inception, quantum mechanics has predicted seemingly counter-intuitive results. Initially, this caused much consternation among the physics community in the first half of the 20<sup>th</sup> century. Many “thought experiments” — which came to be known by their German title of *Gedankenexperiment* — were conceived in an attempt to resolve these apparent paradoxes through drawing on everyday intuition about the world around us. We now know that the strange effects were not in fact paradoxes at all, but that the results of quantum theory simply cannot be interpreted in terms of what we experience on a daily basis in the macroscopic world. However, at the time there was no way of testing this.

The advent of the laser<sup>1</sup> in 1960 opened up the field of experimental quantum optics. For the first time it became possible to produce a coherent, low-divergence

beam of light — a crucial development in experimental physics, despite the initial opposition of the sceptical majority who believed this was “a solution looking for a problem”<sup>2</sup>. During the final quarter of the 20<sup>th</sup> century, new techniques of generating nonclassical states of light, all of which relied on the laser, were first demonstrated and soon became widespread. Experiments utilising these ingenious methods allowed practical investigations of ideas once only imagined by the pioneers of quantum mechanics in the 1920s and 1930s. Most famous amongst these was perhaps the refutation of local hidden variable theories as expressed in the Einstein-Podolsky-Rosen paradox through the violation of the Bell inequalities<sup>3</sup> with entangled pairs of photons<sup>4-9</sup>.

The inherent usefulness of the laser stems from the fact that, due to the stimulated nature of the amplification process within the laser gain medium, all the light is emitted into the same limited set of electromagnetic field modes. Hence the number of photons per mode is much higher than could be achieved with any thermal light source, making lasers exceptionally bright sources of light, essential for most modern physics experiments. An analogy can be drawn here between the emission of photons into identical field modes and the ability to prepare individual quantum systems in indistinguishable states that is at the heart of in many of the experimental demonstrations of quantum mechanics that the laser has been used to achieve. For example, by creating the first Bose-Einstein condensate (BEC)<sup>10</sup> in 1995 it was shown that cooling an ensemble of atoms to their ground state ensures that they are all in indistinguishable states and allows the ensemble to coalesce into a mesoscopic

object displaying quantum behaviour.

Although indistinguishability plays a leading role in the majority of quantum phenomena, it is not trivial to produce single photons that are indistinguishable in all their degrees of freedom. Single photons are fundamental excitations of the electromagnetic field, itself the solution of Maxwell's equations, and as such are interesting for a number of reasons. Single photons and pairs of entangled photons allow tests of quantum mechanics<sup>11</sup>, for example the violations of Bell's inequalities mentioned above. The optical implementation of quantum computation, whether via the linear optics<sup>12</sup> or cluster state<sup>13</sup> model, requires sources capable of generating well-controlled photons. Linear optical quantum logic gates rely on the Bose-Einstein coalescence of single photons incident on a beamsplitter – a so-called Hong-Ou-Mandel interference<sup>14</sup>. However, this will only occur if the two photons are indistinguishable<sup>15</sup>. Single photons are also necessary for certain kinds of quantum cryptography, giving rise to provably secure key distribution.

## 1.2 What is a photon?

*All the fifty years of conscious brooding have brought me no closer to the answer to the question: What are light quanta? Of course today every rascal thinks he knows the answer, but he is deluding himself.*

A. Einstein

*For the purpose of this article, a photon is any eigenstate of the total number operator belonging to the eigenvalue 1.*

L. Mandel<sup>16</sup>

*... the photon is not an object that can be pinned down like a beautiful butterfly in a collection. The photon tells us, "I am who I am!" in no uncertain terms and invites us to get better acquainted with it.*

C. Roychoudhuri and R. Roy<sup>17</sup>

If there is anything to be learnt from these three quotes, it is that, although the basic concept of a discrete wavepacket of light appears at first glance to be simple, the photon is a tricky entity to really understand. After the introduction of the quantization of atomic energy levels to solve the problem of black-body radiation by Planck in 1900, it was Einstein's explanation of the photoelectric effect in 1905 that provided the impetus for the modern quantization of the electromagnetic field. Although this can be explained by a semiclassical theory of quantized exchange of energy between atoms and the light field<sup>18,19</sup>, at the time it was taken as evidence for the discrete nature of light. However, it was another twenty years before the name "photon" was suggested for these fundamental objects by Gilbert Lewis, a chemist, in 1926<sup>20</sup>, though the original concept was of the photon as a "hypothetical new atom, which is not light but plays an essential part in every process of radiation."<sup>21,22</sup>

Light is an electromagnetic field and the formalism of the photonic description arises most clearly from considering the solutions to Maxwell's equations in an optical cavity<sup>23</sup>. The cavity defines a series of longitudinal solutions, known as modes, for a given wavelength, each of which must have an integer number of wavelengths in its optical path. The time-dependent solutions of these modes have the form of

quantized harmonic oscillators and hence their energy levels,  $E_n$ , are discrete:

$$E_n = (n + 1/2)\hbar\omega. \quad (1.1)$$

We can define for this quantum harmonic oscillator operators,  $\hat{a}_i^\dagger$  and  $\hat{a}_i$ , that raise or lower respectively the number of field excitations in a given mode  $i$  by one. These operators are known as the creation and annihilation operators as they create or destroy a single photon in mode  $i$ :

$$\hat{a}_i^\dagger|0\rangle = |1\rangle, \quad (1.2)$$

$$\hat{a}_i|1\rangle = |0\rangle, \quad (1.3)$$

where  $|1\rangle$  is the state vector for a mode containing only one photon and  $|0\rangle$  represents a mode containing no photons, the so-called vacuum state of the system. Although no photons are present in this state and the expectation values of the field quadratures are zero, fluctuations of the vacuum field mean that the quadrature variances are non-zero. The zero-point energy of the quantum harmonic oscillator means that no field mode is ever “empty”: vacuum fluctuations with energy  $(1/2)\hbar\omega$  will always be always present.

This brings us to the most common, and probably unhelpful, definition of a photon:  $|1\rangle$ , the result of the photon creation operator acting on the vacuum state. For theoretical discussions of quantum optics and quantum information processing, this type of state is often assumed to be the logical starting point — after all, surely

it must be the simplest state to make. However, from the point of view of trying to generate this type of state in the laboratory, what does this description really mean? One obvious point is that the portrayal is incomplete: none of the various degrees of freedom that our photon will inevitably have are explicitly expressed in this description. These parameters include frequency, spatial distribution, momentum, and polarisation.

First, let us consider including only the frequency of the photon (written as angular frequency  $\omega$  for convenience). It is a simple enough matter to rewrite the creation and annihilation operators and state vectors to take this into account. The creation operator becomes  $\hat{a}_i^\dagger(\omega_i)$ , and when acting upon the vacuum state it creates a photon in mode  $i$  with angular frequency  $\omega_i$ :

$$\hat{a}_i^\dagger(\omega_i)|0\rangle = |\omega_i\rangle \tag{1.4}$$

So we now have a photon,  $|\omega_i\rangle$ , with a single well-defined frequency,  $\omega_i/2\pi$ . However, we now encounter another problem: photons do not have a single frequency. Our description thus far has assumed that the photon can only exist in a single frequency mode, but for a realistic treatment of the quantized field, a multimode interpretation of the photon must be used. This may at first sound strange, as the traditional view of the particle nature of light tends to imply that the individual wavepackets possess a well-defined (single) frequency. Upon reflection though it is clear that this cannot be the case: a single-frequency photon would have infinite duration and

could therefore not be a wavepacket at all.

To incorporate properly the frequency structure of our photon into its description, we must sum over all possible frequencies with a weight given by the frequency distribution of the particular photon,  $f(\omega_i)$ , as follows,

$$|\Psi_i(\omega)\rangle = \int d\omega_i f(\omega_i) \hat{a}_i^\dagger(\omega_i) |0\rangle. \quad (1.5)$$

Considering only the frequency degree of freedom, this is the most complete mathematical description of a single photon in a pure state. It is interesting to note that, having discarded the assumption that the photon has a single well-defined frequency, we now have the possibility of broadband photons, something which will appear again later in this thesis.

This is the formalism that will be used for describing photons in the following discussions, although the mathematics provide little physical intuition as to what a photon is. Despite its quantized nature, a photon has neither a uniquely specified energy nor momentum. It is also not localized to a particular position in space or time — indeed it can be spread over a broad region of both and many different paths. Yet each photon is indivisible and upon detection will result in a single excitation in a specific location. This leads to a more pragmatic (and popular) definition of the photon, “a photon is what makes my photon detector go *click*”<sup>24</sup>.

### 1.3 Pure states and mixed states

The representations of single-photon states that we have so far considered in Section 1.2 are all examples of what are known as pure quantum states. This is the type of state with which anyone who has completed a course in basic quantum mechanics will be familiar; they can be completely described by a state vector  $|\psi\rangle$ . Pure states are convenient for theoretical calculations as they are straightforward to manipulate and interpret, and are adequate to show the general properties of many simple quantum systems.

However, real-world quantum systems do not exhibit the perfect coherence required for purity, and therefore pure states no longer provide a sufficient framework for modelling them. In these cases, the system cannot be fully described through a state vector alone and instead the density operator formalism must be used. Such a system will be in a statistical mixture of an ensemble of pure states  $|\psi_i\rangle$  each weighted with a probability  $p_i$ . The system is said to be in a mixed state and it can be represented by a density operator  $\hat{\rho}$  that is defined to be <sup>25</sup>

$$\hat{\rho} \equiv \sum_i p_i |\psi_i\rangle\langle\psi_i|. \quad (1.6)$$

This density operator  $\hat{\rho}$  then provides a complete description of the system. Density operators can of course also be used to represent pure states; in this case,  $p_0 = 1$ ,  $p_{i \neq 0} = 0$  and  $\hat{\rho}_{\text{pure}} = |\psi_0\rangle\langle\psi_0|$ . This leads to a simple definition of the purity of any

system given its density operator:

$$\mathcal{P} = \text{Tr}(\hat{\rho}^2). \quad (1.7)$$

It is simple to see that  $\mathcal{P}$  is unity for  $\hat{\rho}_{\text{pure}}$  and tends to zero for maximally mixed states.

In the context of QIP, any impurity in the quantum states is usually detrimental. Mixed states are incoherent (i.e. classical) mixtures and even when prepared in a consistent manner they vary randomly from one iteration to the next. Therefore they cannot generate high-quality interference phenomena, such as would be required for linear optics quantum gates (see Section 1.8). Hence we wish to generate single photons in pure states.

## 1.4 An ideal single photon source: The photon gun

So what type of source is required for photonic quantum information applications? Two things are useful: single photons and pairs of entangled photons. Highly entangled pairs are available through a variety of photon pair generation techniques that are routinely implemented in many laboratories; these will be described in Section 1.5. However, it has until now been difficult to build such a reliable source of high-quality, indistinguishable single photons.

This leads us to consider the concept of the ideal single photon source and the characteristics it would possess. Firstly, the photons produced by independent

sources must be indistinguishable from one another. This means that one must have control over all their degrees of freedom — frequency distribution, emission time, spatial structure, momentum, and polarisation — to ensure that they are identical. Secondly, the photons must be in pure quantum states so that they can be used in optical quantum processing tasks. Thirdly, the photons should be available on-demand: when a photon is requested, one (and only one) is delivered with a probability of one. This type of idealized single photon source is often referred to as a “photon gun” — a box with a button which, when pressed, triggers the release of exactly one photon into the output channel.

However, there are many obstacles in the pursuit of such a source. The most obvious one is loss; any realistic single photon generating device will suffer losses and therefore will not be able to reliably output a photon every time one is requested. On the other hand, some sources suffer from the problem of having a nonzero probability of producing two photons simultaneously. A more subtle problem, and one often not explicitly considered, is that of ensuring indistinguishability between the photons. The conditions at the point of production must be controlled precisely to generate photons with exactly the same structure — otherwise more photons will have to be discarded through lossy filtering.

## 1.5 Methods of single photon generation

The first experiments specifically investigating single photon effects were performed by exciting a sparsely-populated atomic beam and collecting the subsequent emis-

sion. The two prime examples of this were implemented with different excitation processes: an on-resonance excitation yielding a single fluorescence photon<sup>26</sup> and the emission of polarisation-entangled photon pairs after a two-photon excitation<sup>6</sup>. These apparatuses were sufficient for demonstrations of the quantum nature of light, but the clumsy and complex experimental setups — not to mention the quality of the photons produced — were far from the ideal, user-friendly single photon source we seek. This section gives a brief background to the modern techniques that get closer to this ideal and how they relate to the work contained in this thesis. Further details on the methods of single photon generation can be found in the comprehensive review articles by Lounis and Orrit<sup>27</sup> and Oxborrow and Sinclair<sup>28</sup>.

### 1.5.1 Single emitters

The many different methods of generating single photons currently in use can be divided into two broad categories. The first is that of sources with a single emitter, such as a single atom or a quantum dot. To ensure that the individual photons emitted from these sources have the same characteristics — for example their frequency or spatial probability distribution — it is necessary to control the environment surrounding the emitter, commonly by means of a cavity. By coupling the emitter strongly to the cavity, emission can be encouraged into the electromagnetic field modes of the cavity rather than the side modes. The creation of photons in some of these sources is close to being deterministic — that is to say that having “pressed the button”, the probability of generating a photon is close to unity. However, in many

cases the collection efficiencies are poor, reducing the chance of having a useable photon at the output. All single-emitter sources require either complex vacuum or cryogenic equipment or advanced, intricate fabrication techniques, or both.

Single atoms are the obvious choice for use as an emitter of single photons. Assuming the atom is excited into the correct state, photons must be emitted individually<sup>26</sup>, however, this emission is not easy to collect as it occurs in all directions<sup>29</sup>. In cavity quantum electrodynamics (CQED), atoms are coupled to cavities to overcome this problem. Within the cavity modes the density of states of the atomic emission pattern is increased, hence the photons have a higher probability of being created in a cavity mode and the collection efficiency can therefore be improved. The emission linewidths of atoms in cavities are generally narrow (on the order of 10 MHz), giving good coupling to other atomic transitions for storage of photonic quantum states<sup>30</sup> but poor timing information about the single photons. The availability of detectors whose response time is fast relative to photon duration allows temporal filtering of the single photons. This can be used to artificially hide any mixedness and therefore the purity of these photons has not yet been demonstrated. In addition, the central frequency of the emission is sensitive to the exact local conditions around the atom and hence it is difficult to get good overlap between single photons from two separate, independent atoms. CQED systems are complex, involving many laser systems and an ultra-high vacuum (UHV) chamber. Early atom-cavity sources relied on atoms dropping from a magneto-optical trap (MOT) and passing through the cavity<sup>31</sup> or weak trapping in the cavity mode<sup>32</sup>, but recently it has been possible

to hold a single atom in a cavity for durations of several tens of seconds with an optical lattice<sup>33</sup>. A similar source of single photons is a single trapped ion<sup>34,35</sup>. The advantage of ions is that it is much easier to trap an ion in a cavity than it is a neutral atom as ions can be held in an radio-frequency dipole trap.

Advances in semiconductor fabrication technology over the last 20 years have enabled the construction of quantum dots and solid-state microcavities around them. Narrowband single photon emission<sup>36,37</sup> or pair emission<sup>38</sup> occurs from the recombination of electron-hole pairs formed during excitations of the quantum dot. The major problem with these sources is that two quantum dots are never the same and therefore their emission frequencies are different. Hence, interfering photons from two independent quantum dots is almost impossible<sup>39</sup>. Nevertheless, some impressive results have been achieved to date<sup>40</sup> based on the interaction of time-delayed photons originating from the same dot, but the purity of these photons is still imperfect. These sources are in themselves very compact but must be cooled to cryogenic temperatures (usually liquid helium) by bulky equipment. Fabrication of quantum dots in microstructured cavities is inherently complex.

Lattice defects in inorganic crystals, known as colour centres, can be used as single photon sources. The most popular example of this is nitrogen-vacancy (NV) centres in diamond. NV centres consist of a vacancy in the lattice adjacent to a nitrogen impurity, where an electron becomes trapped and acts as an emitter. The energy levels of NV centres act like a four-level system and single photon emission has been observed on the central transition<sup>41,42</sup>. NV centre sources can be operated

at room temperature but background rates are generally high and, for bulk diamond sources, total internal reflection in the sample makes extraction of the single photons problematic. This can, however, be mitigated by forming the NV centre in a diamond nanocrystal rather than a bulk sample<sup>43</sup>. An NV centre single photon source was recently used to experimentally implement Wheeler's delayed choice algorithm<sup>44</sup>, demonstrating that a single photon is truly in a superposition of both arms of an interferometer until a measurement is made.

### 1.5.2 Multiple emitters

The second category of single photon sources is those consisting of many emitters, for example an atomic gas or a bulk medium. These sources are inherently probabilistic — generally a train of pump laser pulses passes through the medium, but for each pulse the probability of obtaining anything at the output is necessarily much less than one. This would appear at first sight to make this type of source useless; what is the point of a source that produces a single photon in any one of several million time windows? Fortunately a solution exists to this apparent problem: rather than generating photons one by one like the single emitters, multiple-emitter sources actually create pairs of photons. Although it is initially unknown whether a given pump pulse will have generated a pair of photons or not, if it has, the pair of daughter photons can be split apart and one of them detected. The detection of one of these photons then announces that a pair-generation event has occurred for that pump pulse and, assuming that the other half of the pair has been successfully collected as

well, a single photon is available in the other arm of the apparatus. This detection process is known as *heralding*.

In the case of many emitters, the structure of the emission is determined by the relative phase of the emitters in the ensemble. An output field can only be generated in directions in which the emitters all remain in phase with the pump field. In these directions constructive interference occurs between the components of the output field generated at different points and the excitation field. In all other directions, the oscillations of the emitters do not remain in phase with the pump hence no output field will be found there. The coherent phasing of individual emitters to obtain constructive interference is known as *phasematching*. It can be achieved by several different methods, depending on the medium used, and will be discussed at length throughout this thesis.

A laser-cooled atomic ensemble<sup>45,46</sup> held in a magneto-optical trap can generate single photons<sup>47,48</sup> via an off-resonant Raman transition in a  $\Lambda$ -type system. First, a collective excitation is created in the ensemble by one laser and confirmed by detecting a single emitted photon. This excitation is then “read out” by a second laser pulse and a single photon is emitted in the opposite direction to the first. Given that one and only one photon was detected after the first pulse, a single photon will be emitted upon application of the read pulse. Additionally, pair generation has also been accomplished in atomic ensembles by a four-wave mixing process<sup>49,50</sup>. As in the single atom or ion case, cooled atomic ensemble sources require several lasers and a UHV system, and care must be taken to match the frequencies of two independent

sources by switching off all fields before emission, though this is less difficult as the emission linewidths are broader. Photon generation rates are generally low as collection can be problematic. A significant advantage of this type of system is that the photons are automatically of the correct linewidth and frequency to be written into a quantum memory based on a similar atomic ensemble<sup>51–53</sup> or enable entanglement distribution<sup>54,55</sup> across a quantum network via series of repeaters.

A recent advance in the field of single photon generation has been the development of photon pair generation in optical fibre<sup>56–60</sup>. This is a four-wave mixing process whereby the third-order nonlinearity of a homogeneous or microstructured fibre allows pump photons to couple to a pair of non-degenerate photons<sup>61</sup>. These photons are then separated from the pump by means of their spectrum. Fibre-based pair sources have the advantages that the fibre allows a very long interaction length to compensate for the very weak nonlinearity and the photons are generated in a single spatial mode. However, the pairs are generally highly correlated in frequency (see Section 1.7) so very tight filtering must be employed.

The final example of a multiple-emitter single photon source is parametric downconversion<sup>62</sup> (PDC). This is one of the most commonly used sources in quantum optics as it provides a relatively straightforward method of generating single photons<sup>63</sup>. This thesis will investigate some aspects of PDC not taken into consideration during the design of the majority of downconversion sources, and through this demonstrate how source engineering can provide superior heralded single photons. PDC is outlined in the next section.

## 1.6 Parametric downconversion

Parametric downconversion<sup>64,65</sup> is a three-wave mixing process wherein a pump photon can decay into a pair of daughter photons, known (for historical reasons) as the *signal* and *idler*. A medium whose polarisation has a nonlinear response to the incident optical frequency provides the coupling between the fundamental and sub-harmonic fields through its nonzero second-order susceptibility ( $\chi^{(2)}$ )<sup>66</sup>. As the process is parametric, in the limiting case no energy or momentum is transferred to the medium and must therefore be conserved between the three fields. The equations describing these conditions are known as the phasematching equations<sup>67</sup>,

$$\omega_p = \omega_s + \omega_i, \quad (1.8)$$

$$\vec{k}_p = \vec{k}_s + \vec{k}_i, \quad (1.9)$$

where  $\omega_\mu$  is photon angular momentum,  $\vec{k}_\mu$  is wavevector, and  $\mu = p, s, i$  denote pump, signal, and idler respectively.

PDC can take place in two regimes: spontaneous<sup>62</sup> and stimulated<sup>68</sup>. In spontaneous PDC, the daughter fields are seeded only by the vacuum fluctuations of the electromagnetic field. In this case, the parametric gain is low and therefore the probability of generating a daughter pair is small. Stimulated PDC is the high-gain regime: the first pair is generated spontaneously, but, due to the high amplification, this pair then acts as a seed for the sub-harmonic field, and many more pairs can be generated concurrently. Clearly, in order to have a high-quality single-photon

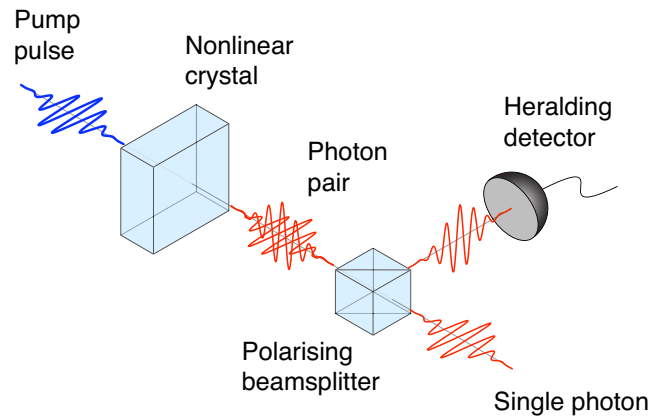


**Figure 1.1** A schematic of type-II PDC. A blue pump pulse passes through a second-order nonlinear crystal and each pump photon has a small probability of decaying into two red daughter photons with orthogonal polarisations. These are then split and one used to detect the presence of the other.

source, the probability of generating two pairs at the same time must be small, and hence all pair production must inevitably be spontaneous. This is achieved by ensuring that the likelihood of generating a pair from a given pump pulse is low. All the work contained herein is concerned with the spontaneous regime.

As a source of single photons, downconversion has the inherent advantages that the apparatus required is simple — only a pump laser and a  $\chi^{(2)}$  nonlinear crystal are needed to generate photon pairs, and the entire apparatus is at room temperature and pressure. The variety of lasers and crystals available give a considerable amount of flexibility in determining the parameters of the photons generated, allowing the use of efficient, room-temperature detectors in many cases. This makes PDC one of the most promising candidates for single photon sources in quantum information applications.

In order to exhibit a second-order nonlinearity a crystal must lack a centre of inversion symmetry<sup>69</sup> (these crystals are known as *non-centrosymmetric*<sup>70</sup>) and as a result all  $\chi^{(2)}$  crystals are optically anisotropic<sup>71</sup>. This leads to birefringence — the refractive index of the crystal is dependent on the polarisation of the light propagating within it. In the case of *uniaxial* crystals (all the crystals considered in this thesis are of this type although downconversion can be performed in biaxial crystals), there is a single axis of rotational symmetry, known as the *optic axis* or *c-axis* of the crystal. Light of arbitrary polarisation traveling through a uniaxial crystal can be decomposed into two orthogonal polarisations: the extraordinary ray (e-ray) is polarised in the plane defined by the optic axis and the incident wavevector (the principal plane), and the ordinary ray (o-ray) is polarised perpendicular to this plane, as illustrated in Figure 1.2. Two refractive indices,  $n_e$  and  $n_o$ , are then defined when these two polarisations propagate at right angles to the optic axis ( $\theta = 90^\circ$ ). As the o-ray electric field is always perpendicular to the optic axis, and due to the crystal symmetry,  $n_o$  does not depend on the angle of propagation through the crystal,  $\theta$ . Conversely, the general form of the e-ray refractive index,  $n_e(\theta)$ , varies with the angle of the wavevector relative to the optic axis.

It is this birefringence that allows the energy and momentum phasematching conditions (Equations 1.8 and 1.9) to be simultaneously satisfied within a single nonlinear crystal for a range of pump and daughter frequencies<sup>72,73</sup>. The angle at which perfect phasematching occurs for a given set of wavelengths,  $\theta = \theta_{pm}$ , is known as the phasematching angle. It also gives rise to two differently-phasematched types

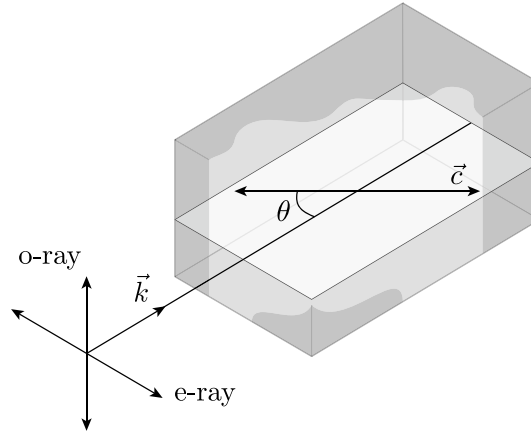


**Figure 1.2** Definitions of e-ray and o-ray polarisations in a non-linear crystal. The angle subtended by the incident wavevector ( $\vec{k}$ ) and the crystal optic axis ( $\vec{c}$ ) at which perfect phasematching occurs is known as the phasematching angle,  $\theta = \theta_{pm}$ .

of PDC. In type-I phasematched PDC, a pump photon decays into a pair of photons with the same polarisation as each other but orthogonal to the pump, whereas in type-II phasematched PDC, a pump photon couples to two daughter photons, one of which has the same polarisation as the pump but the other is orthogonal.

As well as being uniaxial, all the birefringent nonlinear media dealt with in this thesis are so-called *negative* crystals, meaning that they satisfy the relation<sup>74</sup>

$$n_o > n_e. \quad (1.10)$$

As wavevector and frequency are related through

$$k(\omega) = \frac{n(\omega)\omega}{c}, \quad (1.11)$$

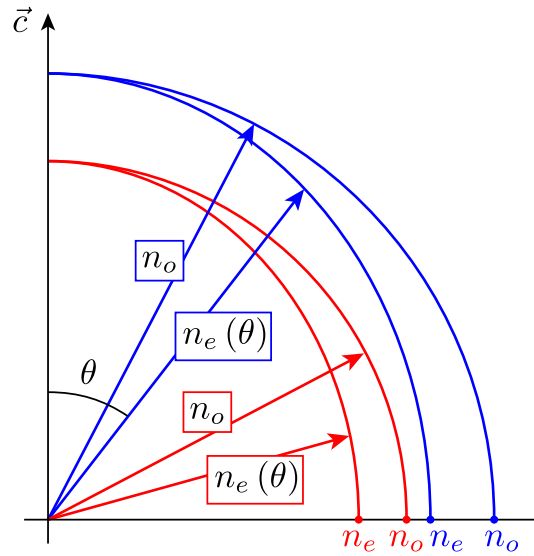


**Figure 1.3** An illustration of the variation of e- and o-ray refractive indices for two wavelengths in a normally-dispersive birefringent crystal. Note that for the sake of clarity the differences between the refractive indices have been scaled up dramatically.

for normally-dispersive media (in which refractive index increases with frequency), this sets the particular polarisations that the two types of downconversion must have. For type-I phasematching, the pump photon must be an e-ray, and the daughter photons o-rays, and for type-II the pump must also be e-ray with one downconverted photon being e-ray and the other o-ray.

The dependence of the e-ray refractive index on the propagation angle means that each type of phasematching has its own characteristic emission pattern<sup>75,76</sup>, shown in Figure 1.4, as phasematching can be satisfied in a range of directions. For type-I PDC, the photon pairs are generated in a series of concentric cones, rotationally symmetric about the pump propagation direction, and the angle of each cone is proportional to the frequency of the pairs. As both photons from the same pair are

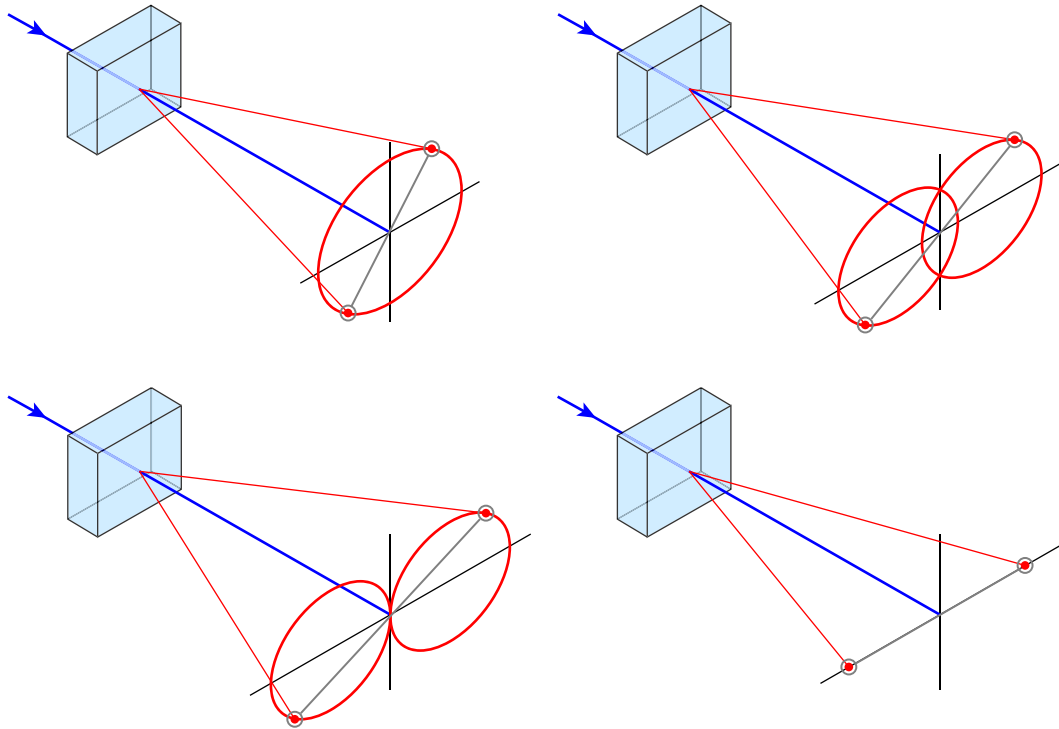


**Figure 1.4** PDC emission patterns for type-I (top left), type-II (top right), type-II collinear (bottom left), and type-II beamlike (bottom right) configurations. In each case, conjugate pairs are emitted on opposite sides of the pattern from one another to satisfy momentum conservation.

identical, their directions of emission are symmetric about the pump direction. In type-II PDC, there is no pairwise symmetry, as one half of each pair is an e-ray and the other an o-ray. The pairs are still emitted in a pattern of cones<sup>77</sup>, but without rotational symmetry about the pump. For each frequency, two cones are present with their centres separated in the principal plane, and in general they intersect along two directions.

There are two special cases of downconversion that will be dealt with in this thesis, the first of which is degenerate PDC. This is the case where the central

frequencies of the distributions of both daughter photons are the same. The second is collinear PDC — when the direction of the wavevectors of both downconverted photons is the same as that of the pump. For type-II phasematching this is the case where the e- and o-ray cones intersect along a single direction. Note that for certain phasematching conditions, the collinear case can be degenerate — indeed this is the form of downconversion mainly considered in this thesis.

## 1.7 Quantum correlations in PDC

All quantum states prepared in the laboratory are to some extent mixed and there are many different ways by which a pure (or perhaps we should say almost pure) state can be transformed into a mixed state. However, the process with which this thesis is primarily concerned is the introduction of impurity to a subsystem of a composite quantum system when a measurement is made on another part of the system. This occurs as a result of correlations between individual components of the system as a whole.

There exist two types of correlation within the output from a parametric down-converter. Firstly, the coupling between frequency and momentum in a birefringent crystal correlates the energy of each individual photon with its momentum (and therefore direction of emission). Secondly, as discussed in Section 1.6, phasematching of the downconversion process binds together the photons within each pair through conservation rules. Hence, more significantly in the context of this thesis, there exist additional pairwise correlations between photons.

The transverse momentum of each pair must sum to zero and therefore the transverse propagation directions of the daughter photons are anti-correlated<sup>75,78</sup> — if one downconverted photon is produced traveling to the left of the pump, the other will be to the right. This is illustrated in Figure 1.4. Even if we restrict the discussion to the collinear type-II case (where transverse momentum is necessarily zero) correlations will still in general be present between the frequency of one photon and that of the other from the same pair<sup>79</sup>. This is simply as a result of the coupling of the e-ray and o-ray frequencies due to phasematching. If such a correlated pair is split up and one photon detected as a herald by a detector that cannot resolve its frequency, this sums over the degrees of freedom of the detected photon and projects the remaining photon into a mixed state, rendering it useless for most QIP applications. This is explained further in Chapter 3.

The technique that is used in most present-day PDC sources to bypass this problem is that of spectral filtering<sup>80–83</sup>. If the emission structure of a parametric downconverter is not controlled, the photon pairs are emitted into many spatio-temporal field modes<sup>84,85</sup>. These pairs are highly correlated in frequency and the heralded single photons derived directly from them would be mixed. However, in order to produce an approximation of purity in the heralded single photons, the generated state is filtered towards a single mode using narrow spectral filters. This discards any pairs that do not satisfy the criteria for purity — any exhibiting pairwise correlations — and, as the filtering required for a given level of purity is generally very tight, results in a huge drop in production efficiency. This becomes a problem

if one wishes to perform experiments with multiple sources or with high photon number.

In contrast, this thesis presents a technique of spectral engineering of photon pairs that allows the generation of uncorrelated two-photon states. Pure, heralded single photons can then be produced directly without the need for spectral filtering and its associated loss.

## 1.8 Hong-Ou-Mandel interference

Photons interact only weakly with their environment. This makes them perfect for transmitting information across networks — either through optical fibre or in free space — where they act as so-called “flying qubits” (a qubit or quantum bit is a logical element in a quantum information processing (QIP) system). However, these weak interactions become a serious obstacle if one tries to use photons to perform computational operations in any QIP scheme.

Initially, it was believed that, in order to implement a photonic QIP device, it would be necessary to couple separate optical fields via nonlinear interactions<sup>86</sup> — something that is easy to achieve with intense laser fields but technically very difficult when the modes involved contain on the order of one photon each. However, in 2001 it was shown by Knill, Laflamme, and Milburn (KLM)<sup>12</sup> that optical QIP could in theory be accomplished without the use of these nonlinear interactions between single photons. In fact, only three basic types of components would be required: single photon sources, photon-number resolving detectors, and linear op-

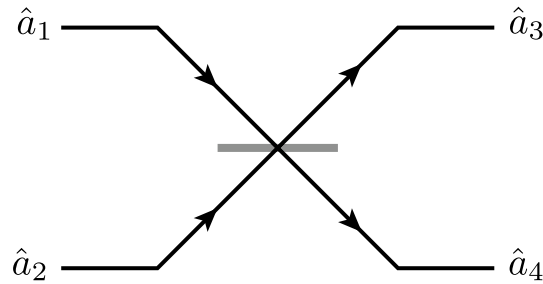


**Figure 1.5** An illustration of the input and output modes of a beamsplitter.

tical elements (beamsplitters and phase shifters). In their proposal, which became known as the KLM scheme for linear optics quantum computation (LOQC), nonlinear field interactions are replaced by beamsplitters that allow mixing of optical modes and hence interactions between single photons, and successful gate operation that is conditional upon certain detectors firing.

The beamsplitter is simply a partially reflecting mirror with two input and two output ports, as shown in Figure 1.5. In the case of a 50:50 beamsplitter, the two input modes are mixed at the interface and whatever is in each input mode has a probability of one half of ending up in each output mode. This illustrates the reason why beamsplitters are such useful components in quantum optics: the indivisible nature of quantized fields results in the output modes being in a quantum superposition that is a combination of whatever was incident on the beamsplitter.

Thus, as beamsplitters allow us to observe interference between weak fields, they can be used to demonstrate the bosonic behaviour of single photons. This is most simply demonstrated by considering a beamsplitter that has reflection and

transmission coefficients,  $\mathcal{R}$  and  $\mathcal{T}$  respectively, that are assumed to be real<sup>23</sup>. We can write down the transformation by such a beamsplitter of input modes 1 and 2 to output modes 3 and 4 as follows:

$$\begin{aligned}\hat{a}_3 &= \mathcal{R}\hat{a}_1 + \mathcal{T}\hat{a}_2 \\ \hat{a}_4 &= \mathcal{T}\hat{a}_1 - \mathcal{R}\hat{a}_2,\end{aligned}\tag{1.12}$$

where the minus sign in the second equation arises from the phase relationship required to make  $\mathcal{R}$  and  $\mathcal{T}$  real while maintaining energy conservation at the interface. Also by using the energy-conserving expression relating  $\mathcal{R}$  and  $\mathcal{T}$ ,  $\mathcal{R}^2 + \mathcal{T}^2 = 1$  we can find similar expressions relating the creation operators for the input modes to those of the output modes:

$$\begin{aligned}\hat{a}_1^\dagger &= \mathcal{R}\hat{a}_3^\dagger + \mathcal{T}\hat{a}_4^\dagger \\ \hat{a}_2^\dagger &= \mathcal{T}\hat{a}_3^\dagger - \mathcal{R}\hat{a}_4^\dagger,\end{aligned}\tag{1.13}$$

The output state is found by substituting the transformed modes at the output for the incident modes at the input, so, for the case of one single photon incident upon each input port of this beamsplitter we have:

$$\begin{aligned}|\psi\rangle &= \hat{a}_1^\dagger\hat{a}_2^\dagger|0\rangle \\ &= \left(\mathcal{R}\hat{a}_3^\dagger + \mathcal{T}\hat{a}_4^\dagger\right)\left(\mathcal{T}\hat{a}_3^\dagger - \mathcal{R}\hat{a}_4^\dagger\right)|0\rangle \\ &= \left(\mathcal{R}\mathcal{T}\hat{a}_3^\dagger\hat{a}_3^\dagger - \mathcal{R}^2\hat{a}_3^\dagger\hat{a}_4^\dagger + \mathcal{T}^2\hat{a}_4^\dagger\hat{a}_3^\dagger - \mathcal{T}\mathcal{R}\hat{a}_4^\dagger\hat{a}_4^\dagger\right)|0\rangle.\end{aligned}\tag{1.14}$$

Now, for a beamsplitter with transmission and reflection coefficients of equal magnitude (a 50:50 beamsplitter),  $\mathcal{R} = \mathcal{T} = (1/\sqrt{2})$  and  $\mathcal{T}^2 - \mathcal{R}^2 = 0$ . Since the operators  $\hat{a}_3^\dagger$  and  $\hat{a}_4^\dagger$  commute, Equation 1.14 reduces to:

$$|\psi\rangle = \frac{1}{\sqrt{2}} \left( \hat{a}_3^\dagger \hat{a}_3^\dagger - \hat{a}_4^\dagger \hat{a}_4^\dagger \right) |0\rangle. \quad (1.15)$$

Hence we see that the two crossed terms containing one photon in each output mode have cancelled each other out. This result shows that, so long as the two single photons are both pure and indistinguishable, they will always emerge in the same output mode of the beamsplitter as each other.

This interference effect is known as *photon bunching* or *Hong-Ou-Mandel interference* (HOMI)<sup>14</sup> and arises as a consequence of the phase shift that occurs upon reflection at the beamsplitter interface. The output modes are in a superposition state of all four terms in Equation 1.14, but for indistinguishable inputs, the second and third terms (representing both photons reflected or both transmitted respectively) are identical as shown in Figure 1.6. However, in the case where both fields are reflected, they pick up a  $\pi$  phase change relative to the transmitted case, resulting in the minus sign in front of the second term. Therefore, due to their indistinguishability, the second and third terms interfere destructively and cancel one another out, leaving only the first and fourth terms: both photons in one output mode or both in the other.

As well as being essential for LOQC, this effect is a useful tool for characterizing

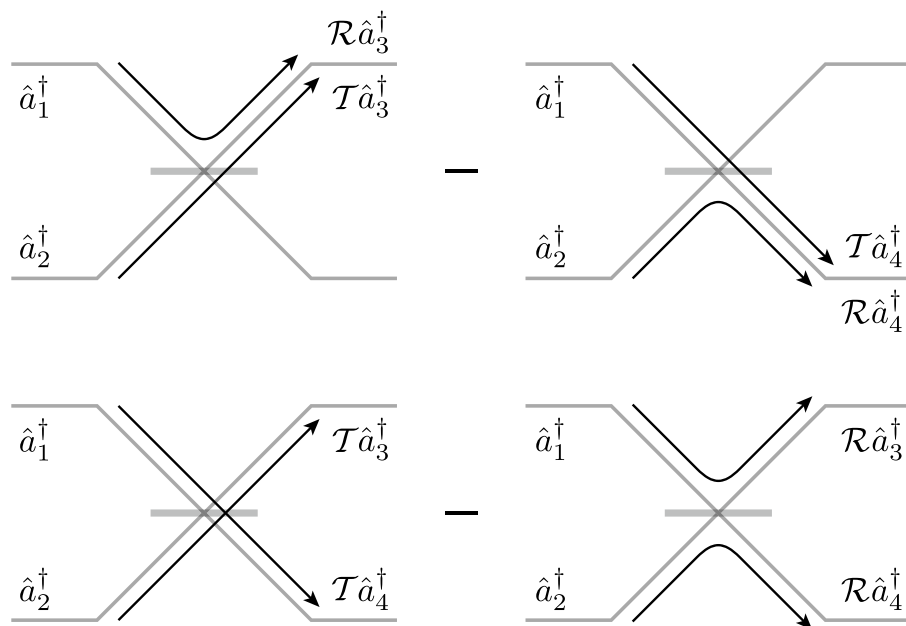


**Figure 1.6** A pictorial representation of single photon interference at a 50:50 beamsplitter, as demonstrated in Equations 1.14 and 1.15. The outcomes of the upper two panels are clearly distinguishable from one another, whereas the outcomes of the lower two panels are not. Indistinguishability and the ensuing destructive interference between these lower two panels results in the observation of photon bunching from the remaining upper panels.

single-photon states. If we were to perform a HOMI between two independent single photons and place two photon detectors on the two outputs of the beamsplitter, we would never observe simultaneous detection events at both detectors if our two photons were pure and indistinguishable.

This interference is an intrinsically quantum effect. If one of the photons incident on the beamsplitter is subjected to a variable time delay relative to the other, some distinguishability will be introduced between them as a result of the additional timing information available to an observer. As the time delay is scanned, the level of distinguishability changes; when the photons are not temporally overlapped at all upon arrival at the beamsplitter (the exact definition of “temporally overlapped” is discussed in Chapter 5), they are perfectly distinguishable and no interference can occur, whereas when they are perfectly overlapped, as was assumed in the calculation above, they are indistinguishable and perfect photon bunching should be seen. Therefore, if one were to record the rate of coincidence detection events at the two detectors as a function of the time delay (which is assumed to be small compared to the coincidence window), one would observe that it drops from a constant value where the photons are not overlapped to zero at zero time delay. This interference pattern is called a *HOMI dip*, as shown in Figure 1.7, and its visibility is defined as

$$V = \frac{P_C(\infty) - P_C(0)}{P_C(\infty)}, \quad (1.16)$$

where  $P_C(\tau)$  is the probability of obtaining a coincidence event as a function of the

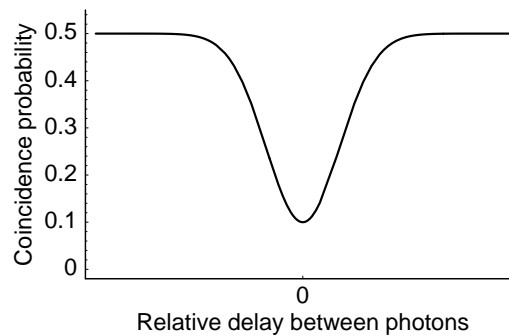


**Figure 1.7** A Hong-Ou-Mandel interference dip with  $V = 0.8$ .

time delay  $\tau$ . The maximum value that the visibility can attain were the light arriving at the beamsplitter classical has been shown to be  $0.5^{16}$ , but for the interference of pure, indistinguishable single photons, the visibility will be 1.

## 1.9 The state of the art in photonic QIP

Several implementations of optical QIP protocols have been demonstrated to date. Both the strategies for and the experimental verifications of quantum information processing that have been published so far are reviewed much more comprehensively than would be possible here by Ralph<sup>87</sup> and Kok *et al*<sup>88</sup>. All of these demonstrations have relied on interfering single photons with each other. However, all single photon sources suffer from random fluctuations in the properties of the photons from shot to shot, for example in their emission time (commonly known as *timing jitter*) or frequency. Therefore the emission structure of the ensemble of states is generally not single mode. This degrades the interference visibility as, when two photons arrive

at a beamsplitter, there is a chance that they will be distinguishable due to these fluctuations.

This limitation of current single photon sources is a constraint on the performance of quantum gates. Due to the statistical degradation of the state present at the input, the gate will not function correctly during some fraction of the trials. Previous implementations of QIP schemes have all required successful operations to be distinguished from failures by conditioning the outcome on a particular pattern of detection events. This applies both to ancillary measurements during gate operation in the KLM scheme and to heralding detections indicating correct state preparation in the cluster state model. However, in both cases the inability to input the desired state on every shot means that error-free operation must be post-selected not only on these ancillary measurements but also on the presence of logical qubits. The fluctuation of the input means that in many cases there will not be a photon in the information-carrying output modes and gate operation is non-deterministic even given that the ancillary detections have been correctly made.

Instead of preparing imperfect nonclassical states, this idea of post-selection can be taken to the extreme by inputting classical states to a system and conditioning the measurement on a pattern of detector firings. A recent experiment demonstrated that quantum-enhanced precision phase measurements are possible starting with only weak coherent (classical) states and using post-selective measurements to “invert the roles of state production and measurement”<sup>89</sup>. The price that one pays for this is that most of the input resources are wasted as they do not contribute to the

final result due to the poor overlap of the input state with the state projected onto by the measurement. This reduces the frequency with which the desired outcome is observed.

This issue of post-selection is not too much of a problem for experiments on small numbers of photons as one can obtain a reasonable overlap between the imperfect input and the ideal state. However, current gates are beginning to reach the stage where it is the source quality that is limiting the performance of quantum algorithms rather than the gates themselves<sup>90</sup>. If we want to move to higher photon numbers and longer strings of concatenated gates we need better single photon sources.

Downconversion sources have improved vastly since the first demonstration of parametric fluorescence in 1970<sup>62</sup>, however, there is still a long way to go in closing the gap between current sources and the ideal single photon generator. Table 1.1 gives the raw figures for a selection of several downconversion sources and other pair generation sources to allow a comparison to be made with what follows in this thesis.

## 1.10 Thesis outline

This thesis is presented in six chapters. The first chapter has given a background on the various methods of single photon generation and introduced some of the considerations one has to take into account when working with parametric downconversion as a heralded single photon source. The second chapter provides a more rigorous theoretical treatment of PDC and phasematching in birefringent media. Chapter 3 deals with characterizing correlations in the two-photon states resulting from PDC

Year	Paper	Method	Pump	Power	$\lambda_0$ (nm)	$\Delta\lambda_s$ (nm)	SMF	$R_C$ (s <sup>-1</sup> )	$\eta_D$	$\eta_H$
1970	Burnham <sup>62</sup>	Type-I PDC in ADP	cw	9 mW	633/668	4/1.5	No	2.5	1.2%	–
1987	Hong <sup>14</sup>	Type-I PDC in KDP	cw	~10 mW	702	8	No	1.3	–	–
1995	Kwiat <sup>91</sup>	Type-II PDC in BBO	cw	150 mW	702	5	No	1500	>10%	–
2001	Kurtsiefer <sup>92</sup>	Type-II PDC in BBO	cw	465 mW	702	None	Yes	$3.6 \times 10^5$	28.6%	–
2004	U'Ren <sup>93</sup>	Type-II PDC in PPKTP waveguide	fs	15 $\mu$ W	800	2/None	No	12750	51%	85%
2005	Pittman <sup>94</sup>	Type-I PDC in BBO	fs	79 mW	~780	10	Yes	~1000	31%	83%
2006	Chen <sup>95</sup> , Yuan <sup>46</sup>	Atomic ensemble	ns	–	795	None	Yes	15	–	<95%
2007	Lu <sup>82</sup>	Type-II PDC in BBO	fs	910 mW	788	3.2	Yes	$9.3 \times 10^4$	–	–
2007	Fedrizzi <sup>96</sup>	Type-II PDC in PPKTP	cw	1 mW	~810	None	Yes	$8.2 \times 10^4$	28.5%	84.4%
2007	Neergaard-Nielsen <sup>97</sup>	Type-I PDC in PPKTP in cavity	cw	1.7 mW	~860	~10 <sup>-4</sup>	No	12000	62%	70%
2007	Fulconis <sup>98</sup>	FWM in PCF	ps	1 mW	528/900	0.28/2	Yes	1700	–	~5%
2007	Halder <sup>99</sup>	PDC in PPLN waveguide	cw	2 mW	1560	0.01	Yes	100	–	–

**Table 1.1** Comparison of a small selection of photon pair sources. Pump = pump duration: cw (continuous wave), ns, ps, fs. Power = average pump power for one source.  $\lambda_0$  = central photon wavelength (two wavelengths indicates nondegenerate pairs).  $\Delta\lambda_s$  = spectral filter width (two values indicates different filters were applied to each daughter photon). SMF = single-mode fibre coupling of photons.  $R_C$  = rate of coincidence counts per second.  $\eta_D$  = detection efficiency.  $\eta_H$  = heralding efficiency. Detection efficiency is the ratio of pair count rates to that of singles and heralding efficiency is a measure of how often a single photon is available given a detection event has occurred (see Chapter 5). Dashes appear where the information was unavailable.

---

and possible methods of removing these correlations by careful source design. Some of the resulting experimental design issues are expounded in Chapter 4, including the effects of focusing and a spatially-varying pump beam, along with the results of a numerical model. Direct measurements of the spectral structure of photon pairs from the downconversion source are compared with the results of this model. Chapter 5 presents the main experimental methods and a detailed description of the downconversion source used. The results of the interference experiments on two heralded single photons from independent sources are presented. This gives a measure of the purity of the heralded single photons. The conclusions and an outlook on future work are contained in Chapter 6.



## Chapter 2

# Parametric Downconversion

In the first chapter, some of the concepts that will play leading roles in this thesis were introduced. The purpose of this chapter is to further explain PDC and phase-matching and set these within a mathematical framework to enable the subsequent discussion of source engineering later in this thesis. The standard derivation of the two-photon state from PDC is presented with details tailored for relevance to the work contained herein. Phasematching in birefringent nonlinear media is considered in depth, including an intuitive explanation of the underlying mechanics and techniques to visualise both type-I and type-II processes. The resulting spectral structure of general joint two-photon states for both cases are shown to elucidate the origins of spectral correlations between the daughter photons.

The field of nonlinear optics exploits the anharmonic response of a particular medium to an incident optical field. The medium acts as an ensemble of oscillators whose behaviour can be decomposed into frequencies that are the harmonics and sub-

harmonics of the driving field. In the case of nonlinear crystals, the anharmonicity in the frequency response is a consequence of the asymmetry of the crystal structure; each oscillator is subjected to a potential that is distorted by the presence of the crystal lattice. Therefore, when excited by the driving field, each oscillator has the possibility of emitting a field at any of the harmonics of the initial excitation.

The nonlinearity of the medium is described by the response of its polarisation<sup>70</sup>,  $P(\omega)$ , to an incident field with angular frequency  $\omega$ :

$$P(\omega) = \varepsilon_0\chi^{(1)}E(\omega) + \varepsilon_0\chi^{(2)}E^2(\omega) + \varepsilon_0\chi^{(3)}E^3(\omega) + \dots \quad (2.1)$$

A medium exhibiting significant second-order nonlinearity will provide coupling between an incident field and two others through its  $\chi^{(2)}$  coefficient. Equation 2.1 can then be truncated after the second term. The field in this second term can be expanded as

$$E^2(\omega) = E_0^2 \cos^2(\omega t) = \frac{E_0^2}{2} [1 - \cos(2\omega t)], \quad (2.2)$$

demonstrating the coupling between fields at  $\omega$  and  $2\omega$ . The dipole polarisation of the nonlinear medium in response to an incident field  $E_p(\vec{r}, t)$  is

$$P_p^{(2)}(\vec{r}, t) = \varepsilon_0 \sum_{m,n} \chi_{p,m,n}^{(2)} E_m(\vec{r}, t) E_n(\vec{r}, t). \quad (2.3)$$

where the indices  $p$ ,  $m$ , and  $n$  represent fields that can be in any of the three Cartesian coordinate directions. Therefore, the general form of  $\chi_{p,m,n}^{(2)}$  for a given set of three

fields is a  $3 \times 3 \times 3$  tensor, however, the permutation symmetry of the elements along with symmetry properties of uniaxial crystals can be invoked to reduce this number significantly. The displacement tensor,  $d_{p,m,n} = \frac{1}{2}\chi_{p,m,n}^{(2)}$ , can then be re-expressed in matrix form, and for any set of three fields an effective second-order nonlinear coupling coefficient,  $d_{\text{eff}}$ , which is dependent on propagation direction and crystal type, defined. We will not overly concern ourselves with the form of this coefficient as it only appears as a constant influencing the frequency conversion efficiency (a full description is given by Midwinter and Warner<sup>71</sup>). It is the coupling given by this component of the material polarisation between the incident pump field and the two output fields that allows the generation of photon pairs at around half the pump frequency.

If these two emitted fields were considered as classical waves emanating from an isolated emitter, they would propagate in all directions away from the source. However, in a nonlinear crystal, one must consider the contributions to the total field from the entire ensemble of emitters<sup>73</sup>. These emitters are driven coherently by the pump field and their harmonic emission must remain in phase with this field in order to sum constructively and form a macroscopic output. This is the essence of phasematching an ensemble of emitters.

The requirement for constructive interference between the fields to obtain useable output means that the conditions for phasematching define what the output state will be. Due to the inherent birefringence of the available nonlinear crystals, these conditions are tied to the frequencies of the fields in the interaction and their

propagation directions in the crystal. Hence in order to understand the structure of the photon pairs generated, it is vital to have a solid grasp of the mechanics of phasematching.

By deriving the quantum state generated in downconversion from first principles it not only becomes clear how the form of the two-photon state arises but also that the conditions for phasematching are found directly from the mathematics. In order to be able to prepare pure, heralded single photon states it is essential to understand the manner in which changing a parameter such as the pump wavelength or crystal type affects the relationship between the daughter photons. Only then is it possible to choose the conditions that will yield pure-state single photons.

## 2.1 Theory of parametric downconversion

This section presents a derivation of the quantum state generated by spontaneous PDC in the perturbative regime. Similar calculations have been presented by many authors, most relevantly for the current situation Hong and Mandel<sup>65</sup>, Rubin *et al*<sup>100</sup>, Grice and Walmsley<sup>79</sup>, and U'Ren<sup>101</sup>. The case considered in this derivation is that of either type-I or type-II PDC with a pulsed pump laser, hence the daughter photons are labeled using the historical names signal (*s*) and idler (*i*). The result can then be applied to either type of PDC simply by choosing the polarisation of the daughter photons within the crystal frame of reference. The pump field is denoted *p*. During this derivation, for the sake of clarity, we assume plane-wave propagation of the fields involved and therefore the functional dependence of the final state is on

frequency only.

In the interaction picture, given that we started at time zero with a state  $|\psi_0\rangle$ , the state at a time  $t$  — after the interaction is complete — is then

$$|\psi_t\rangle = \hat{T} \exp \left[ \frac{1}{i\hbar} \int_0^t dt' \hat{H}_I(t') \right] |\psi_0\rangle, \quad (2.4)$$

where  $\hat{H}_I(t')$  is the interaction Hamiltonian of the system and  $\hat{T}$  is the time-ordering operator. For the spontaneous regime, the downconverted modes are seeded only by vacuum fluctuations, and so the initial state is the vacuum,  $|\psi_0\rangle = |0\rangle$ . Furthermore, given that the interaction strength is small, this exponential can be expanded and anything beyond the second term discarded:

$$|\psi_t\rangle \approx \left[ 1 + \frac{1}{i\hbar} \int_0^t dt' \hat{H}_I(t') \right] |0\rangle. \quad (2.5)$$

This is equivalent to stating that the probability of generating one pair of photons within each interaction period is small and the probability of generating two is negligible. This interaction period is defined as the time during which the pump pulse is propagating through the nonlinear crystal, i.e. the pulse enters the crystal at  $t = 0$  and exits at time  $t$ .

The general form of the interaction Hamiltonian for a second order nonlinear process can be written as the integral over the interaction volume  $V$  of the second order contributions to the electromagnetic field energy density. For field  $E_p(\vec{r}, t)$  and

dipole polarisation  $P_p(\vec{r}, t)$  this is

$$H_I = \frac{1}{2} \int_V dV P_p(\vec{r}, t) E_p(\vec{r}, t). \quad (2.6)$$

where the fields arising from this polarisation are described in Equation 2.3.

Therefore we see that, following quantization of the field,  $\hat{H}_I$  for spontaneous PDC can be written

$$\hat{H}_I(t) = \varepsilon_0 d_{\text{eff}} \int_V dV \hat{E}_p(\vec{r}, t) \hat{E}_s(\vec{r}, t) \hat{E}_i(\vec{r}, t), \quad (2.7)$$

where  $\hat{E}_\mu(\vec{r}, t)$  is the quantized field operator for field  $\mu = p, s, i$  denoting pump, signal and idler respectively. By decomposing these field operators into their positive and negative frequency components,  $\hat{E}_\mu(\vec{r}, t) = \hat{E}_\mu^{(+)}(\vec{r}, t) + \hat{E}_\mu^{(-)}(\vec{r}, t)$ , the Hamiltonian can then be expressed as

$$\hat{H}_I(t) = \varepsilon_0 d_{\text{eff}} \int_V dV \hat{E}_p^{(+)}(\vec{r}, t) \hat{E}_s^{(-)}(\vec{r}, t) \hat{E}_i^{(-)}(\vec{r}, t) + \text{H.c.} \quad (2.8)$$

The components of the plane-wave field operators are<sup>23</sup>:

$$\begin{aligned} \hat{E}_\mu^{(+)}(\vec{r}, t) &= i \int_0^\infty d\omega_\mu \left[ \frac{\hbar\omega_\mu}{2\varepsilon_0 n(\omega_\mu) V_Q} \right]^{\frac{1}{2}} \hat{a}_\mu(\omega_\mu) \exp \left[ i \left( \vec{k}_\mu(\omega_\mu) \cdot \vec{r} - \omega_\mu t \right) \right] \\ \hat{E}_\mu^{(-)}(\vec{r}, t) &= -i \int_0^\infty d\omega_\mu \left[ \frac{\hbar\omega_\mu}{2\varepsilon_0 n(\omega_\mu) V_Q} \right]^{\frac{1}{2}} \hat{a}_\mu^\dagger(\omega_\mu) \exp \left[ -i \left( \vec{k}_\mu(\omega_\mu) \cdot \vec{r} - \omega_\mu t \right) \right], \end{aligned} \quad (2.9)$$

where  $V_Q$  is the quantization volume. Note that if we were to generalize this deriva-

tion to include the effects of Gaussian beam propagation these operators would also be summed over wavevector. As the pump has to be a strong laser field, it can be treated classically and the positive frequency component of its quantized field operator from Equation 2.9 replaced with

$$\hat{E}_p^{(+)}(\vec{r}, t) \Rightarrow E_p^{(+)}(\vec{r}, t) = A_p \int_0^\infty d\omega_p \alpha(\omega_p) \exp \left[ i \left( \vec{k}_p(\omega_p) \cdot \vec{r} - \omega_p t \right) \right], \quad (2.10)$$

where  $A_p$  is the pump amplitude and  $\alpha(\omega_p)$  is the spectral amplitude distribution of the pump, known as the pump envelope function.

We now substitute Equations 2.9 and 2.10 into Equation 2.8 to yield the full expression for the interaction Hamiltonian:

$$\begin{aligned} \hat{H}_I(t) = \varepsilon_0 d_{\text{eff}} A_p \int_0^\infty d\omega_p \int_0^\infty d\omega_s \int_0^\infty d\omega_i \int_V dV \alpha(\omega_p) A_s(\omega_s) A_i(\omega_i) \\ \hat{a}_s^\dagger(\omega_s) \hat{a}_i^\dagger(\omega_i) \exp \left[ i \left( \vec{k}_p(\omega_p) \cdot \vec{r} - \vec{k}_s(\omega_s) \cdot \vec{r} - \vec{k}_i(\omega_i) \cdot \vec{r} \right) \right] \\ \exp \left[ -i (\omega_p - \omega_s - \omega_i) t \right] + \text{H.c.} \end{aligned} \quad (2.11)$$

where we have used the simplifying substitution  $A_\mu(\omega_\mu) = \left[ \frac{\hbar \omega_\mu}{2 \varepsilon_0 n(\omega_\mu) V_Q} \right]^{\frac{1}{2}}$ . The quantum state at time  $t$  can then be found by operating this Hamiltonian on the input quantum state,  $|0\rangle$ , as in Equation 2.5. Note that when this operator is applied to the vacuum state the Hermitian conjugate term vanishes as the action of the annihilation operators on the vacuum gives zero:  $\hat{a}_s(\omega_s)|0\rangle = \hat{a}_i(\omega_i)|0\rangle = 0$ . The

resulting expression for the output state is then

$$\begin{aligned}
|\psi_t\rangle = |0\rangle + \frac{i\varepsilon_0 d_{\text{eff}} A_p}{\hbar} \int_0^\infty d\omega_p \int_0^\infty d\omega_s \int_0^\infty d\omega_i \alpha(\omega_p) A_s(\omega_s) A_i(\omega_i) \\
\int_V dV \exp \left[ i \left( \vec{k}_p(\omega_p) \cdot \vec{r} - \vec{k}_s(\omega_s) \cdot \vec{r} - \vec{k}_i(\omega_i) \cdot \vec{r} \right) \right] \\
\int_0^t dt' \exp \left[ -i (\omega_p - \omega_s - \omega_i) t' \right] \hat{a}_s^\dagger(\omega_s) \hat{a}_i^\dagger(\omega_i) |0\rangle.
\end{aligned} \tag{2.12}$$

In the situation presented here, downconversion is driven by an ultrashort pulsed laser and the temporal profile of the pulses can be found by taking the inverse Fourier transform of  $\alpha(\omega_p)$ :

$$\tilde{\alpha}(t') = \int_0^\infty d\omega_p \alpha(\omega_p) \exp \left[ -i\omega_p t' \right]. \tag{2.13}$$

This function, which sets the interaction time, will be short compared to  $t$ , the time when we are observing the generated quantum state after the interaction is deemed to have finished. The time-dependent pump envelope sets the time period over which the interaction takes place; the Hamiltonian is zero at times when  $\tilde{\alpha}(t') = 0$ . Therefore the limits of the time integration in Equation 2.12 can be set to infinity. The integral over  $t'$  then becomes

$$\int_{-\infty}^\infty dt' \exp \left[ -i (\omega_p - \omega_s - \omega_i) t' \right] = \delta(\omega_p - \omega_s - \omega_i) = \delta(\Delta\omega) \tag{2.14}$$

so for all nonzero terms we must have  $\omega_p = \omega_s + \omega_i$  and the integral over  $\omega_p$  becomes trivial. In addition, we make use of the fact that  $A_s(\omega_s)$  and  $A_i(\omega_i)$  are slowly varying functions of frequency and are therefore approximately constant over the range of

$\alpha(\omega_p)$ .  $A_s(\omega_s)$  and  $A_i(\omega_i)$  can then be taken outside the integral and Equation 2.12 simplifies to

$$|\psi_t\rangle = |0\rangle + \frac{i\varepsilon_0 d_{\text{eff}} A_p A_s(\omega_s) A_i(\omega_i)}{\hbar} \int_0^\infty d\omega_s \int_0^\infty d\omega_i \alpha(\omega_s + \omega_i) \int_V dV \exp \left[ i \left( \vec{k}_p(\omega_s + \omega_i) \cdot \vec{r} - \vec{k}_s(\omega_s) \cdot \vec{r} - \vec{k}_i(\omega_i) \cdot \vec{r} \right) \right] \hat{a}_s^\dagger(\omega_s) \hat{a}_i^\dagger(\omega_i) |0\rangle. \quad (2.15)$$

The integral over  $V$  can be decomposed into three integrals in Cartesian coordinates. We set the crystal to be orientated such that its input and output faces are in the  $xy$ -plane and it has length  $L$  in the  $z$ -direction. Imagining a collimated, plane wave pump whose transverse profile fits entirely within the crystal faces, the limits of integration in the  $x$ - and  $y$ - directions can be taken to be infinity:

$$\int_V dV e^{i\Delta\vec{k} \cdot \vec{r}} = \int_{-\infty}^\infty dx e^{i\Delta k_x x} \int_{-\infty}^\infty dy e^{i\Delta k_y y} \int_0^L dz e^{i\Delta k_z z} \quad (2.16)$$

where  $\Delta k_x = k_{p,x}(\omega_s + \omega_i) - k_{s,x}(\omega_s) - k_{i,x}(\omega_i)$ , and similarly for  $y$  and  $z$ . For this case in which the transverse distribution of the pump is effectively ignored, we see that the  $x$  and  $y$  integrals simply yield delta functions and the  $z$  term, when multiplied by  $(1/L)$ , gives a sinc function:

$$\frac{1}{2L} \int_V dV \exp \left[ i\Delta\vec{k} \cdot \vec{r} \right] = \delta(\Delta k_x) \delta(\Delta k_y) \exp \left[ \frac{i\Delta k_z L}{2} \right] \text{sinc} \left[ \frac{\Delta k_z L}{2} \right]. \quad (2.17)$$

If the transverse pump distribution were considered more realistically we would

obtain broader transverse phasematching functions more akin to the longitudinal condition. However, the approximation above is valid for the scope of this work. Additionally, a further simplification can be made by assuming that the pump and downconverted fields propagate collinearly with one another along the  $z$ -axis. Then the  $x$ - and  $y$ -components of the wavevectors are zero,  $\Delta\vec{k} = (0, 0, \Delta k_z)$ , and Equation 2.16 becomes

$$\begin{aligned} \int_V dV \exp [i\Delta\vec{k} \cdot \vec{r}] &= \int_0^L dz \exp [i\Delta k z] \\ &= 2L \exp \left[ \frac{i\Delta k L}{2} \right] \text{sinc} \left[ \frac{\Delta k L}{2} \right], \end{aligned} \quad (2.18)$$

where  $\Delta k = \Delta k_z$ . This case of collinear propagation is sufficient for the initial discussion of factorable state generation discussed in Chapter 3 of this thesis. Substituting Equation 2.18 into Equation 2.15 we obtain the final expression for the downconverted state in the case of collinear propagation, with the only functional dependence being on the frequencies of the daughter photons:

$$\begin{aligned} |\psi_t(\omega_s, \omega_i)\rangle &= |0\rangle + \frac{2i\varepsilon_0 d_{\text{eff}} A_p A_s(\omega_s) A_i(\omega_i) L}{\hbar} \int_0^\infty d\omega_s \int_0^\infty d\omega_i \alpha(\omega_s + \omega_i) \\ &\quad \exp \left[ \frac{i\Delta k L}{2} \right] \text{sinc} \left[ \frac{\Delta k L}{2} \right] \hat{a}_s^\dagger(\omega_s) \hat{a}_i^\dagger(\omega_i) |0\rangle. \end{aligned} \quad (2.19)$$

This can be tidied up by grouping all the factors before the integrals together as an efficiency term  $\eta$  so that

$$|\psi_t(\omega_s, \omega_i)\rangle = |0\rangle + \eta \int_0^\infty d\omega_s \int_0^\infty d\omega_i \alpha(\omega_s + \omega_i) \phi(\omega_s, \omega_i) \hat{a}_s^\dagger(\omega_s) \hat{a}_i^\dagger(\omega_i) |0\rangle, \quad (2.20)$$

where we have defined the collinear phasematching function to be

$$\phi(\omega_s, \omega_i) = \exp\left[\frac{i\Delta k L}{2}\right] \text{sinc}\left[\frac{\Delta k L}{2}\right]. \quad (2.21)$$

Hence we see that the frequency dependence of the two-photon state generated in PDC is given by the product of the pump envelope function,  $\alpha(\omega_s + \omega_i)$ , with the phasematching function,  $\phi(\omega_s, \omega_i)$ . We can group these two functions together into a new function,  $f(\omega_s, \omega_i)$ , the joint spectral amplitude, and use this to describe the joint spectral probability distribution of the photon pairs

$$F(\omega_s, \omega_i) = |f(\omega_s, \omega_i)|^2, \quad (2.22)$$

where  $F(\omega_s, \omega_i)$  is known as the joint spectral intensity. Given that a photon pair has been created, this is the probability of detecting a signal photon with frequency  $\omega_s$  and a corresponding idler photon with frequency  $\omega_i$ .

## 2.2 Phasematching in birefringent media

Not only does the previous section provide the two-photon amplitude from PDC, it also serves as a derivation of the phasematching conditions. Firstly, from integrating over time in Equation 2.14, we obtain the energy matching condition:

$$\omega_p = \omega_s + \omega_i. \quad (2.23)$$

Secondly, integrating Equation 2.16 over space yields two delta functions and a sinc function and hence we see that for the largest amplitude in the output state we require  $\Delta\vec{k} = 0$  and

$$\vec{k}_p = \vec{k}_s + \vec{k}_i. \quad (2.24)$$

In the collinear case where  $\Delta k_x$  and  $\Delta k_y$  are necessarily zero, Equation 2.24 becomes  $\Delta k = \Delta k_z = 0$  and

$$k_p(\omega_p, \theta_p) = k_s(\omega_s, \theta_s) + k_i(\omega_i, \theta_i). \quad (2.25)$$

These equations tell us the mathematical conditions that must be fulfilled for perfect phasematching, however, they give little insight into the underlying physical process.

### 2.2.1 The physics of phasematching

To elucidate this process further and gain some feeling for the way in which these equations permit phasematched emission from a nonlinear crystal, we can consider a couple of simple cases. We begin by representing diagrammatically a simplified model of degenerate type-I PDC in a negative uniaxial nonlinear crystal. This is the simplest version of phasematching to investigate because the momentum phasematching condition reduces to a relation between the refractive indices and therefore the phase velocities. Due to the symmetry between the photon pair,  $k_s(\omega_s, \theta_s) = k_i(\omega_i, \theta_i)$ , and in the collinear case Equation 2.25 reduces to

$$k_p(\omega_p, \theta_p) = 2k_s(\omega_s, \theta_s) \Rightarrow \frac{\omega_p}{k_p(\omega_p, \theta_p)} = \frac{\omega_0}{k_s(\omega_s, \theta_s)}. \quad (2.26)$$

where  $\omega_0$  is the central downconversion frequency, equal to half the pump frequency  $\omega_p$  due to energy conservation. The phase velocity is given by

$$v_{ph} = \frac{\omega}{k(\omega)} = \frac{c}{n(\omega, \theta)}, \quad (2.27)$$

after application of Equation 1.11. Hence we see from Equation 2.26 that the wavefronts must travel at the same speed in the collinear configuration to achieve phasematching. This can be generalised to the noncollinear case where it becomes a condition on the  $z$ -component of the phase velocity:

$$k_{p,z}(\omega_p, \theta_p) = 2k_{s,z}(\omega_s, \theta_s) \Rightarrow \frac{\omega_p}{k_{p,z}(\omega_p, \theta_p)} = \frac{\omega_0}{k_{s,z}(\omega_s, \theta_s)}. \quad (2.28)$$

Therefore the type-I case is relatively straightforward to visualise as we can simply consider how the wavefronts propagate through the medium and look for the emission directions in which the  $z$ -components of the phase velocity are equal.

These expressions allow an intuitive digrammatic representation of phasematching to be drawn. The pump, which is modelled as plane wave, is an e-ray and the daughter photons are o-rays as the crystal is negative. The pump field is represented by a set of parallel lines at its antinodes. So as to not clutter the diagram overly, we envisage a row of emitters positioned along the pump wavevector. Although in a real crystal the emitters would be packed so densely that their lattice spacing would be much less than the wavelength of the incident optical field, here we consider only a subset of emitters at the instantaneous antinodes of the pump field. These

emitters can be considered to be driven the hardest at that particular moment and dominate the emission pattern, but the conclusions can anyway be generalised to the closely-packed case. We treat each individual in this subset of emitters as a Huygens secondary source of radiation at half the frequency of the pump field. As the downconverted light propagates as an ordinary ray, the refractive index it experiences does not depend on its angle relative to the optic axis and so the individual emission patterns can be represented as a series of concentric circles at the antinodes of the sub-harmonic field.

Firstly we take the unrealistic case of a crystal that has no birefringence and no dispersion, depicted in Figure 2.1. The condition of no birefringence sets  $n_e(\omega, \theta_{pm}) = n_o(\omega)$  for all frequencies  $\omega$  at the particular pump propagation angle,  $\theta_{pm}$ . As this implausible crystal also exhibits no dispersion, there is a further condition that the refractive index is the same for pump and downconverted fields,  $n_e(\omega_p, \theta_{pm}) = n_o(\omega_{s,i})$ , and as a result all the wavefronts travel with the same phase velocity. Consider now the directions in which the  $z$ -components of the phase velocities of the pump and downconverted fields are the same. These are the points at which each individual line of the pump field intersects the wavefront from the emitter corresponding to the same cycle of the field. These crossing points are marked in Figure 2.1. These all occur where the emission circles are tangent to the pump field lines. Connecting these points together we have a line along the direction of the pump wavevector. This line corresponds to the direction in which the emitters are all in phase with the pump field. Hence it is clear in this case that phasematching and

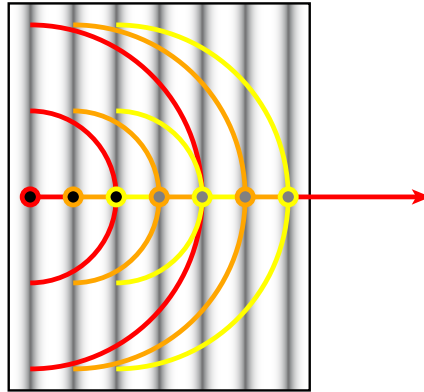


**Figure 2.1** Illustration of collinear phasematching in a crystal without dispersion or birefringence. The vertical lines represent the antinodes of the pump field. Each of the three black emitters has a pair of concentric rings around it marking the field propagating away from them at half the pump frequency. Colours simply link each field to a specific emitter. Constructive interference occurs where the emission wavefronts intersect with the corresponding pump antinodes, marked for each emitter by the grey-filled circles. Here this takes place in the collinear direction only.

therefore coherent emission will occur only in the direction of pump propagation.

Indeed, in the case of a dispersionless medium, perfect collinear phasematching will always occur.

Secondly, we add normal dispersion into the picture. Now because the frequency of the o-ray downconverted field is half that of the e-ray pump, dispersion changes the relative refractive indices of both fields so that  $n_e(\omega_p, \theta_{pm}) > n_o(\omega_{s,i})$  and the phase velocity of the downconverted field is increased relative to the pump. This situation is shown in Figure 2.2. Due to their increased phase velocity, the wavefronts of the PDC field travel faster than those of the pump and this is represented by the enlargement of the emission circles (in this case, their diameter has been scaled up by 1.1). Again, the points at which the  $z$ -component of the phase velocity is the

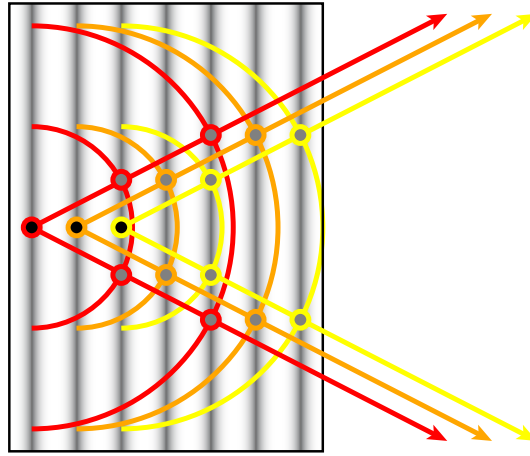


**Figure 2.2** Illustration of phasematching in a crystal with normal dispersion but without birefringence. Due to the higher phase velocity of the longer wavelength fields, phasematching now occurs at an angle to the incident field.

same for pump and downconversion are marked where corresponding lines intersect. Note now that the lines do not meet where the circles are tangent to the pump field lines — there is therefore no coherent addition in the collinear direction. Instead, the points of intersection lie along a line at an angle to the direction of propagation of the pump and noncollinear phasematching occurs.

Thirdly, if the condition set on the birefringence of the crystal is now relaxed so that  $n_e(\omega, \theta_{pm}) \neq n_o(\omega)$ , it can be seen that the introduction of birefringence alters the direction of emission. In this case the crystal is negative ( $n_o(\omega) > n_e(\omega, \theta_{pm})$ ) and hence, as the downconverted field is o-ray, the increase in  $n_o(\omega_{s,i})$  from the birefringence counteracts its reduction due to dispersion. Therefore, in this case, the birefringence acts to bring back the emission direction closer to collinear, as demonstrated in Figure 2.3.

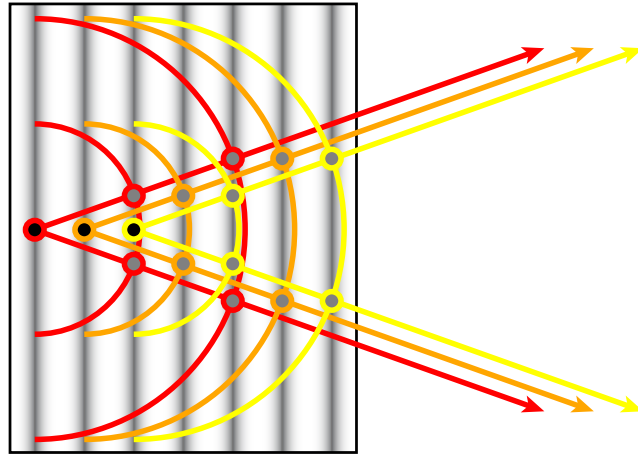


**Figure 2.3** Illustration of phasematching in a crystal with both normal dispersion and birefringence. The reduction in phase velocity of the generated fields by the birefringence brings the phasematching angle back closer to the collinear direction.

It is worth noting that if in this model we had added birefringence before dispersion we would not have observed any phasematching. As noted in the previous paragraph, the effect of birefringence in a negative crystal is to increase  $n_o$  relative to  $n_e$ , hence the phase velocity is reduced for the o-ray. Without the effects of dispersion, which reduces  $n_o$  relative to  $n_e$ , the phase velocity of the o-ray would always be too small for it to “catch up” with the e-ray, the lines on the figures would not intersect, and phasematching would not occur. This is why for type-I phasematching in a normally-dispersive birefringent medium the pump must always be e-polarised and the downconversion o-polarised.

Through the tradeoff between dispersion and birefringence it is possible to obtain degenerate collinear type-I phasematching in a realistic crystal. By choosing a pump wavelength and crystal orientation angle that offsets the relative increase

in  $n_e$  over  $n_o$  from dispersion with the reduction in  $n_e$  as a result of birefringence, phasematching can be achieved. In this case  $n_e(\omega_p, \theta_{pm}) = n_o(\omega_0)$  and the situation is again as depicted in Figure 2.1.

### 2.2.2 More complex phasematching conditions

These simplified examples give some feel for how phasematching takes place in a birefringent medium. However, due to the asymmetry between signal and idler photons, the picture is much more complex for type-II processes. The simple conditions on the phase velocities found in Equations 2.26 and 2.28 can no longer be applied and therefore diagrams similar to those previously constructed are insufficient to accurately describe the interaction.

Starting from the most straightforward case of type-II phasematching, that of collinear and degenerate PDC, we can derive a different condition on the phase velocities of the interacting fields. Taking Equation 2.25 and dividing by the central downconversion frequency,  $\omega_0 = \omega_p/2$  we find

$$\frac{2k_p(\omega_p, \theta_p)}{\omega_p} = \frac{k_s(\omega_s, \theta_s) + k_i(\omega_i, \theta_i)}{\omega_0}. \quad (2.29)$$

Therefore, we see that there is still a relationship that must be satisfied between the phase velocities, albeit through their inverses. Equation 2.29 states that the inverse phase velocities of the daughter photons must sum to twice that of the pump or, equivalently, the inverse phase velocity of the pump must be equal to the average inverse phase velocity of the downconverted fields. Clearly this is something that

is neither intuitive to consider nor easy to represent graphically in an insightful manner. However, instead of trying to analyze the type-II case in this way, an easier condition to visualise can be found. Substituting Equation 1.11 relating the wavevector to the refractive index and frequency into Equation 2.25 we obtain:

$$n_p(\omega_p, \theta_p)\omega_p = n_s(\omega_s, \theta_s)\omega_s + n_i(\omega_i, \theta_i)\omega_i \quad (2.30)$$

and for the degenerate case this becomes:

$$2n_p(\omega_p, \theta_p) = n_s(\omega_s, \theta_s) + n_i(\omega_i, \theta_i). \quad (2.31)$$

This condition on the refractive indices experienced by the three fields allows phase-matching to be described using the index ellipsoids first shown in Figure 1.3. Figures such as those presented subsequently were first drawn by the pioneers of phase-matched second harmonic generation<sup>71–73</sup>.

As already mentioned, the o-ray refractive index is not dependent on the direction of propagation, and is represented by a circle with radius  $n_o$ . Light traveling along the optic axis must be o-polarised due to the crystal symmetry. The largest difference between e- and o-rays occurs for propagation perpendicular to the optic axis and it is in this direction that  $n_e$  is defined. An e-ray subtending an angle other than  $90^\circ$  with the optic axis will experience a refractive index value that lies on an ellipsoid, the index ellipsoid, joining  $n_o$  on the axis to  $n_e$  at  $90^\circ$  to the axis. This ellipsoid

defining the e-ray refractive index is therefore:

$$\frac{x'^2}{n_o^2} + \frac{y'^2}{n_o^2} + \frac{z'^2}{n_e^2} = 1. \quad (2.32)$$

Here the optic axis lies along the  $z'$ -direction and so the linear optical response of a uniaxial crystal is rotationally symmetric about this axis and the  $y'$ -direction can be ignored. The radius of this ellipsoid, and therefore the angle-dependent e-ray refractive index, can be parameterized as function of  $\theta$ :

$$n_e(\theta) = \left[ \frac{\cos^2 \theta}{n_o^2} + \frac{\sin^2 \theta}{n_e^2} \right]^{-\frac{1}{2}}. \quad (2.33)$$

This is a convenient way in which to describe the e-ray refractive index.

The illustration of phasematching through the index ellipses is first demonstrated for collinear type-I phasematching in a negative uniaxial crystal to facilitate a comparison with the simple model presented in Section 2.2.1. In this case the condition for phasematching, Equation 2.31, reduces to

$$n_p(\omega_p, \theta_p) = n_s(\omega_0) = n_i(\omega_0). \quad (2.34)$$

and the situation is shown in Figure 2.4. Phasematching occurs where the pump index ellipse intersects the circle representing the signal and idler index. This takes place at a propagation angle  $\theta_{pm}$  relative to the optic axis and in this type of picture it is easy to see how this phasematching angle arises. The arrows in the figure

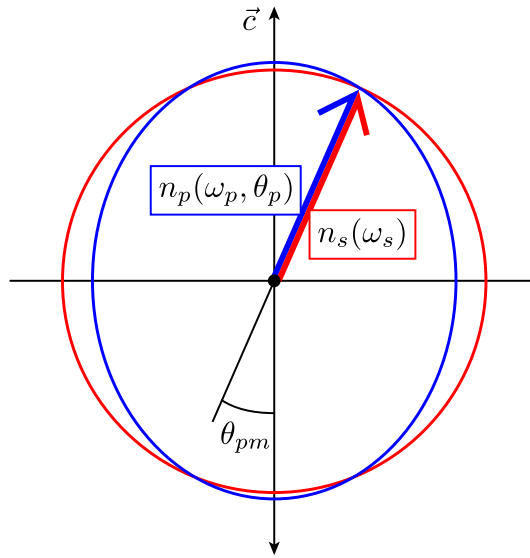


**Figure 2.4** Collinear type-I phasematching in a negative uniaxial crystal. The blue ellipse is the angle-dependent pump refractive index and the red circle is the o-ray refractive index at half the pump frequency. Phasematching occurs where the two intersect.

describe the wavevectors of the pump and downconverted light and, as in Equation 2.24, these must be equal.

Unlike the previous model, it is straightforward to extend this to type-II phasematching by using the full form of Equation 2.31. Again we first take the case of collinear degenerate phasematching in a negative crystal, as shown in Figure 2.5. The radius of the pump ellipse has now been multiplied by two, the o-ray circle is placed with its centre at the origin, and the centre of the e-ray ellipse rests on the circumference of this circle. By varying the sizes of both the circle and the ellipse (through changing the frequencies of the downconverted photons while maintaining degeneracy) as well as the position of the ellipse on the circumference of the circle, a set of parameters can be found whereby the downconversion ellipse touches tan-

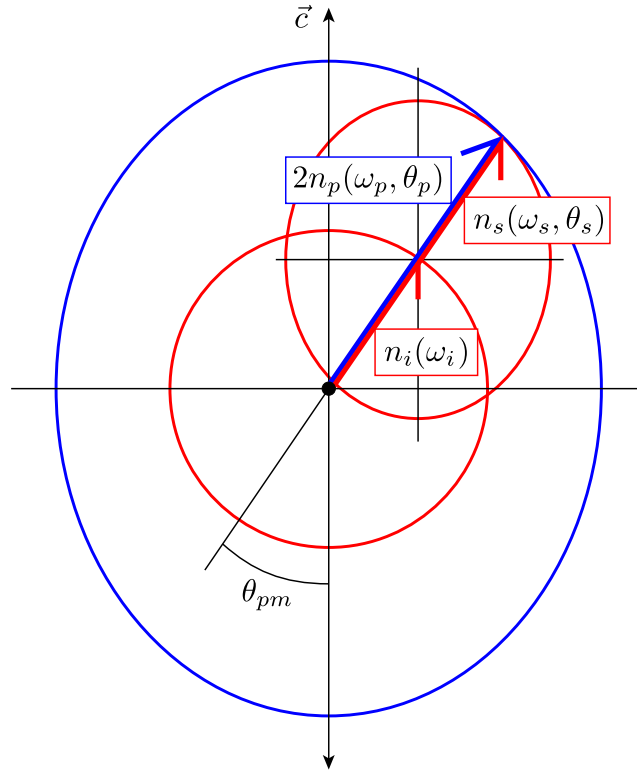


**Figure 2.5** Collinear type-II phasematching in a negative uniaxial crystal. The blue ellipse is twice the pump refractive index, the red ellipse and circle are respectively the refractive indices of the e- and o-ray downconverted fields.

gentially that of the pump at only one point. The e- and o-ray wavevectors then lie parallel to that of the pump. This set of parameters defines the phasematching angle of the pump at which degenerate collinear phasematching occurs.

Now imagine translating this PDC ellipse around the circumference of the o-ray circle without changing the size of either. For the same pump angle, a second position can be found where the two ellipses intersect at the terminus of the pump vector, as shown in Figure 2.5. Phasematching also occurs here, but the wavevectors of the downconversion are then no longer parallel to the pump direction, and hence

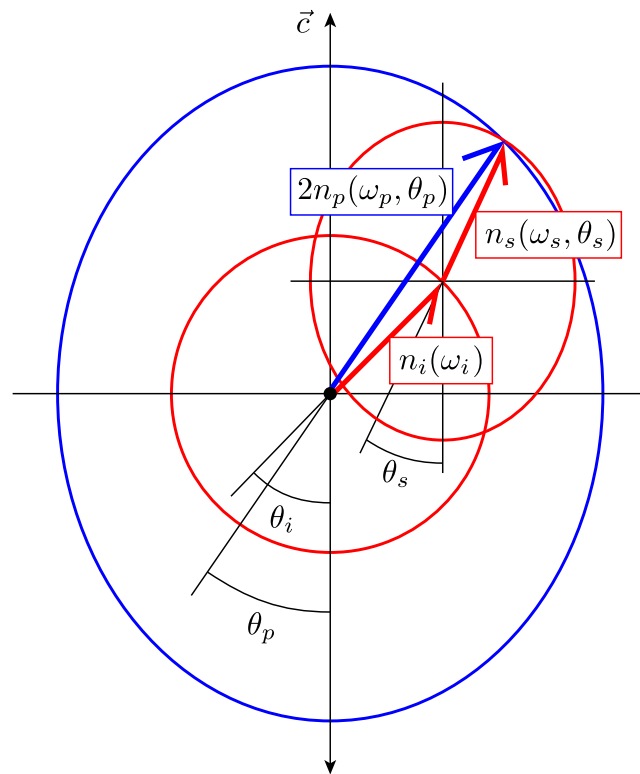


**Figure 2.6** Noncollinear type-II phasematching in a negative uniaxial crystal. As for Figure 2.5 but the position of the e-ray ellipse has been adjusted to illustrate noncollinear phasematching.

this situation describes noncollinear phasematching. Signal and idler photons are emitted at a pair of conjugate angles to the pump.

Hence we see that for this pump wavevector there are two ways of phasematching the production of photon pairs, one collinear and one noncollinear. However, we have only considered a two-dimensional analysis of the situation. If this were extended to three dimensions we would find that, as the index ellipsoids are rotationally symmetric about their optic axes, the emission patterns would be cones, one for the e-ray and one for the o-ray, where we have taken a section through the cones to

find only two angles of emission. Generalizing still further, the cones do not always intersect, and when they do it is not always tangentially as in the collinear case, as was shown in Figure 1.4.

So we have seen how phasematching arises in birefringent media and how the characteristics of the medium influence the emission directions. However, so far this has explained nothing about the frequency structure of the pairs, something that will be essential for the discussion of pure single photon generation.

### 2.3 The form of the two-photon state

In Section 2.1, the two-photon state from PDC was derived and expressed in Equation 2.20. This led to the two-photon joint spectral amplitude being defined as the product of the pump envelope function with the phasematching function:

$$f(\omega_s, \omega_i) = \alpha(\omega_s + \omega_i)\phi(\omega_s, \omega_i), \quad (2.35)$$

where the function  $f(\omega_s, \omega_i)$  contains all the spectral (and therefore temporal) information about the two-photon state. The joint spectral amplitude is in general complex as it contains the phases of both the phasematching function and the pump function (if it is not transform limited), so we define a real joint spectral intensity (or joint spectrum),  $F(\omega_s, \omega_i)$ , that is the modulus squared of the joint amplitude.

The pump envelope function is taken to be a Gaussian function of the pump frequency centered at twice the central downconversion frequency,  $\omega_0$ , and defined

as

$$\alpha(\omega_p) = \exp \left[ i\varphi(\omega_p) - \left( \frac{\omega_p - 2\omega_0}{\sigma} \right)^2 \right]. \quad (2.36)$$

For most of the discussion in this thesis it is assumed that the pump laser has approximately flat phase and therefore  $\varphi(\omega_p)$  is set to zero. Equation 2.36 is transformed into a two-dimensional function of signal and idler frequency by the substitution  $\omega_p = \omega_s + \omega_i$

$$\alpha(\omega_s + \omega_i) = \exp \left[ - \left( \frac{\omega_s + \omega_i - 2\omega_0}{\sigma} \right)^2 \right], \quad (2.37)$$

which is clearly symmetric in the two frequencies.  $\sigma$  is defined in terms of the full width at half maximum (FWHM) bandwidth of the spectral intensity as follows:

$$\sigma = \frac{\text{FWHM}_\omega}{\sqrt{2 \ln 2}} = \frac{2\pi c}{\lambda_{0p}^2} \frac{\text{FWHM}_\lambda}{\sqrt{2 \ln 2}} \quad (2.38)$$

where  $\text{FWHM}_\omega$  and  $\text{FWHM}_\lambda$  are the FWHM bandwidths of the pump intensity distribution measured in frequency and wavelength respectively. It is clear that the width of the pump envelope function is proportional to the bandwidth of the pump laser, and this can therefore affect the correlations between the daughter photons, as will be explained in the next chapter. A range of pump functions for different bandwidths is displayed in Figure 2.7.

The general form of the phasematching function is that of a sinc function, as given in Equation 2.21, that drops — with a rapidity dependent on the inverse of the crystal length — away from the line of zero phase mismatch between the

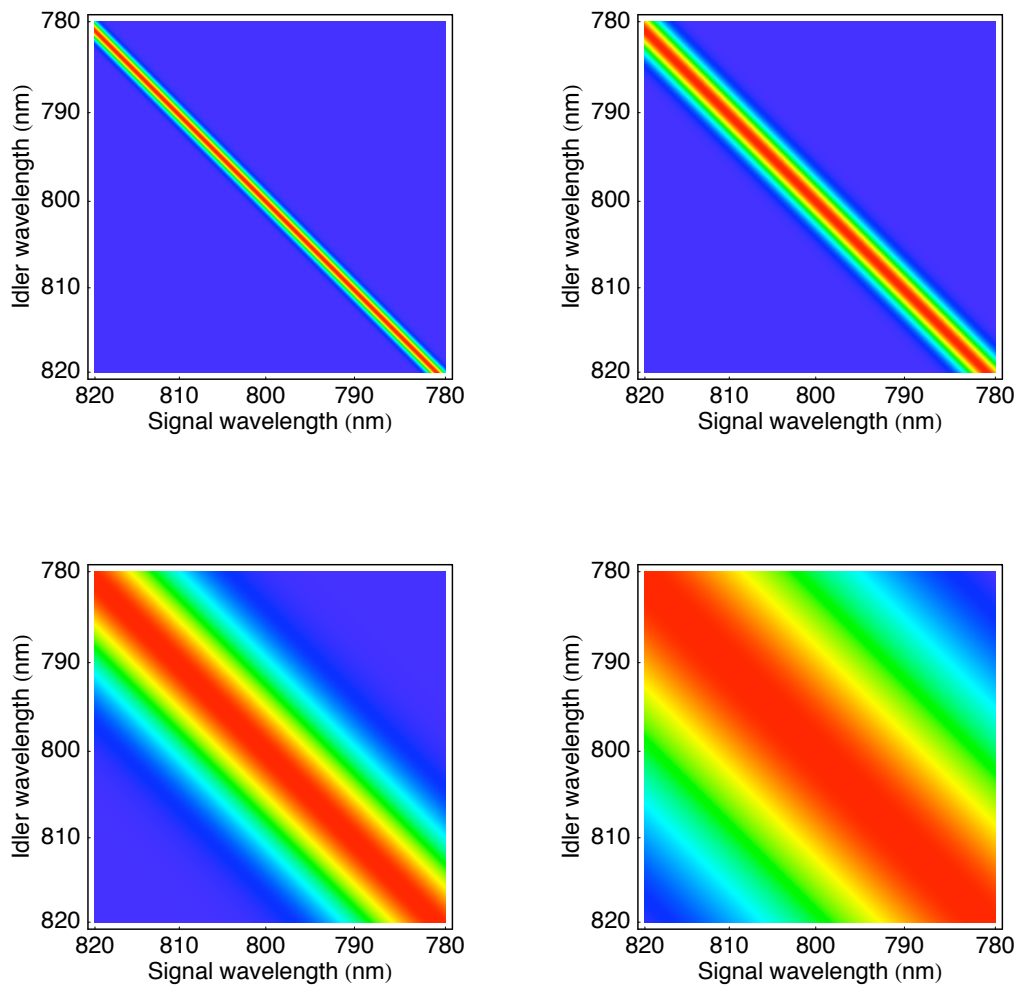


**Figure 2.7** Intensity distributions of pump functions with central wavelengths of 400 nm and bandwidths of 0.4, 1, 4, and 10 nm. Note that all plots of this type contained within are plotted as a function of signal and idler frequency and labelled in wavelength for convenience.

pump and daughter photons. The particular configuration of an individual phase-matching function is controlled by the optical properties of the nonlinear crystal used for the interaction. Every commonly available birefringent crystal has a set of empirical equations, known as the Sellmeier equations<sup>74</sup>, that describe the variation in the o- and e-ray refractive indices as a function of wavelength and, in some cases, temperature. From these equations the phase mismatch over a range of signal and idler frequencies can be found in the manner of Equation 2.30, and hence the phase-matching function plotted.

### 2.3.1 Type-I phase-matching

A type-I phase-matched process generates daughter photons with the same polarisation as each other. Therefore they both experience identical dispersion and hence the phase-matching function and two-photon state must be symmetric in the line  $\omega_s = \omega_i$ .

A typical calculated type-I phase-matching function is shown in Figure 2.8. In this case the nonlinear crystal was a 2 mm long piece of  $\beta$ -barium-borate (BBO) — one of the most widely used downconversion crystals — arranged in a collinear configuration to produce degenerate pairs at 800 nm. The phase-matching angle for this arrangement is  $\theta_{pm} = 29.2^\circ$ . The crystal is pumped by 1 nm FWHM pulses and hence the phase-matching function is similar to the pump function except that it is slightly curved. This curvature limits the overlap of the two functions and hence the bandwidth of the downconversion. Multiplying these two functions together gives

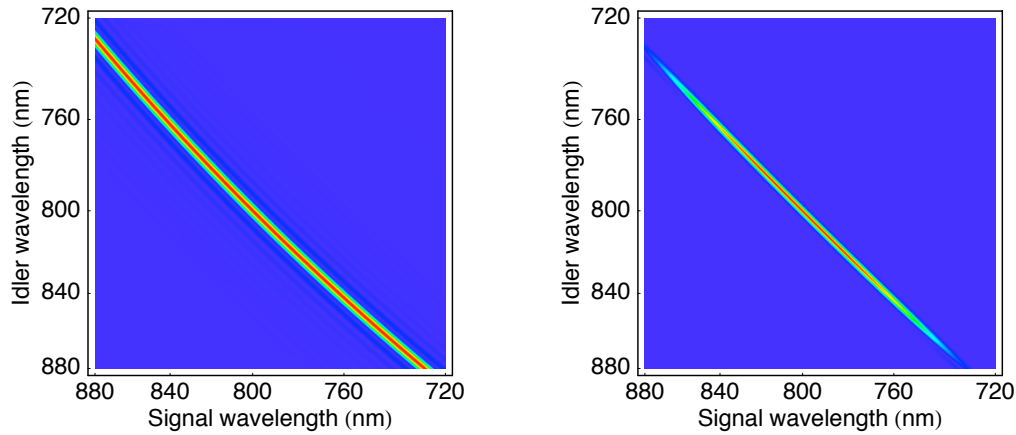


**Figure 2.8** Phasematching intensity and joint spectral probability distribution for a 2 mm long collinear type-I phasematched BBO crystal pumped at 400 nm by 1 nm bandwidth pulses (this corresponds to the second pump function plotted in Figure 2.7).

the two-photon joint probability distribution for this process. Note that, regardless of the bandwidth of the pump, the photon pairs will always be highly negatively correlated in frequency for a type-I process as a result of their symmetry.

### 2.3.2 Type-II phasematching

Conversely, in type-II processes, individual daughter photons will in general experience different dispersion from their siblings, and this breaks the symmetry of the phasematching function. The line of zero phase mismatch can therefore subtend a broad range of angles with the frequency axes, dependent on the properties of the Sellmeier equations for the particular nonlinear crystal. It is this additional flexibility of type-II phasematching that will be exploited in the next chapter to produce factorable states by setting the angle of the phasematching function at a given pair

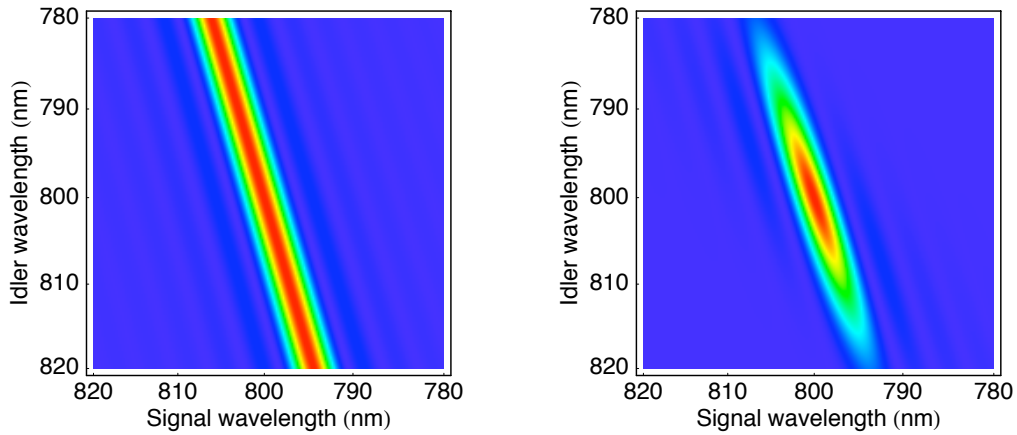


**Figure 2.9** Phasematching intensity and joint spectral probability distribution for a 2 mm long collinear type-II phasematched BBO crystal pumped at 400 nm by 4 nm bandwidth pulses (this corresponds to the third pump function in Figure 2.7).

of wavelengths.

Figure 2.9 demonstrates this point by illustrating the type-II collinear degenerate phasematching function for BBO. The phasematching angle has now changed to  $\theta_{pm} = 42.3^\circ$  to give the correct dispersion for pump and e-ray downconverted light to achieve phasematching, and as a result  $\phi(\omega_s, \omega_i)$  is rotated towards vertical. In addition, the type-II phasematching function is slightly broader than that for type-I. Clearly this changes the overlap with the pump function (here, 4 nm FWHM), and the final joint spectrum is plotted in the second panel of the figure. Although this has altered the spectral correlations between signal and idler photons, they are still highly correlated in frequency and hence a heralded photon from this source would inevitably be in a mixed state.



## Chapter 3

# Two-Photon State Engineering

The phenomenon of Hong-Ou-Mandel interference between two single photons was introduced in Chapter 1. This effect is vital to photonic implementations of quantum computation and fundamental new technologies, but it is challenging to prepare single photons with the required levels of purity and indistinguishability to yield the high-visibility interference exploited in these techniques. So is it possible to achieve good interference with some impurity in the single photons used? To answer this question, an attempt to interfere two photons in mixed states of frequency at a beam-splitter is considered in the opening section of this chapter. Subsequently, through studying the density operator for a heralded single photon, it is shown that this reduced state can be pure if and only if the joint spectral amplitude distribution of the initial pair is factorable. Two methods of quantifying this factorability are explained. Firstly, the use of the Schmidt decomposition in this context is revised, though it can only be applied to a specific class of simplified two-photon states. Secondly,

the singular value decomposition, not utilised in previous studies of factorable state generation, is introduced as a method of determining the factorability of *any* bipartite state. A detailed numerical analysis of the effects of spectral filtering, present on the output of almost all standard downconverters to limit spectral correlation, is developed to further motivate this work on *ab initio* factorable pair production. The origin of factorable states in the strictly collinear regime of type-II downconversion is presented, following in the footsteps of Grice *et al*<sup>102</sup> and U'Ren *et al*<sup>101</sup>.

Consider two single photons in mixed states sent simultaneously one into each of the input ports 1 and 2 of a 50:50 beamsplitter, as illustrated in Figure 1.5. For the purposes of this analysis, the photons are described by distributions over a discrete set of  $n$  frequency modes and initially each photon is in a classical mixture of all the possible frequency modes. However, this mode decomposition could be performed in any complete basis suitable for the system under investigation, for example spatial or temporal mode for photons, and hence the result is applicable to any variable in which the photon exhibits mixedness. The density operators for single photons in mixed frequency states in spatial modes 1 and 2 can be written

$$\begin{aligned}\hat{\rho}_1 &= \sum_{i=1}^n p_{1i} |\omega_{1i}\rangle \langle \omega_{1i}| = \sum_i p_{1i} \hat{a}_{1i}^\dagger |0\rangle \langle 0| \hat{a}_{1i} \\ \hat{\rho}_2 &= \sum_{j=1}^n p_{2j} |\omega_{2j}\rangle \langle \omega_{2j}| = \sum_j p_{2j} \hat{a}_{2j}^\dagger |0\rangle \langle 0| \hat{a}_{2j},\end{aligned}\tag{3.1}$$

where  $\hat{a}_{1i}^\dagger$  is the creation operator for a photon in spatial mode 1 and frequency

mode  $i$  and  $\sum_i p_{1i} = 1$ . These individual input states have purities given by

$$\mathcal{P}_1 = \text{Tr} \hat{\rho}_1^2 = \sum_{i=1}^n p_{1i}^2, \quad \mathcal{P}_2 = \text{Tr} \hat{\rho}_2^2 = \sum_{j=1}^n p_{2j}^2, \quad (3.2)$$

and the total input state is

$$\hat{\rho} = \sum_i \sum_j p_{1i} p_{2j} \hat{a}_{1i}^\dagger \hat{a}_{2j}^\dagger |0\rangle \langle 0| \hat{a}_{1i} \hat{a}_{2j}. \quad (3.3)$$

The beamsplitter relationships remain as in Equation 1.12 but with the addition of frequency subscripts:

$$\begin{aligned} \hat{a}_{1i}^\dagger &= \frac{1}{\sqrt{2}} (\hat{a}_{3i}^\dagger + \hat{a}_{4i}^\dagger) \\ \hat{a}_{2j}^\dagger &= \frac{1}{\sqrt{2}} (\hat{a}_{3j}^\dagger - \hat{a}_{4j}^\dagger), \end{aligned} \quad (3.4)$$

and the transformed input state becomes

$$\begin{aligned} \hat{\rho} &= \frac{1}{4} \sum_i \sum_j p_{1i} p_{2j} (\hat{a}_{3i}^\dagger \hat{a}_{3j}^\dagger - \hat{a}_{3i}^\dagger \hat{a}_{4j}^\dagger + \hat{a}_{3j}^\dagger \hat{a}_{4i}^\dagger - \hat{a}_{4i}^\dagger \hat{a}_{4j}^\dagger) |0\rangle \\ &\quad \langle 0| (\hat{a}_{3i} \hat{a}_{3j} - \hat{a}_{3i} \hat{a}_{4j} + \hat{a}_{3j} \hat{a}_{4i} - \hat{a}_{4i} \hat{a}_{4j}). \end{aligned} \quad (3.5)$$

The projection operator<sup>25</sup> for detecting a coincidence event at the two outputs is also required. Throughout this thesis, detectors are modelled as silicon avalanche photodiode single photon counting modules with a broadband frequency response that is assumed to be flat over the range of frequencies we are interested in. The

detectors are not frequency resolving and therefore cannot perform any spectral filtering unless an external filter is placed in front of them. Furthermore, due to the mechanics of the avalanche process within the silicon diode, the temporal resolution of the detectors is many times longer than the coherence time of the downconverted photons, so they cannot be used to temporally filter the photons either. The operator for a single detection event is therefore an incoherent sum over a range of frequencies:

$$\hat{\Pi}_D = \sum_d p_d |\omega_d\rangle \langle \omega_d|. \quad (3.6)$$

A coincidence event will result from simultaneously detecting a photon of either frequency mode in both of the spatial modes 3 and 4. The operator for these possibilities is then given by

$$\hat{\Pi}_{2C} = \sum_i \sum_j \hat{a}_{3i}^\dagger \hat{a}_{4j}^\dagger |0\rangle \langle 0| \hat{a}_{3i} \hat{a}_{4j}. \quad (3.7)$$

The expectation value of this operator is then given by the standard expression  $\text{Tr}(\hat{\rho} \hat{\Pi}_{2C})$ .

The action of  $\hat{\Pi}_{2C}$  on  $\hat{\rho}$  removes any terms in which both photons appear in the same output port and the outcome of the measurement becomes

$$\text{Tr}(\hat{\rho} \hat{\Pi}_{2C}) = \text{Tr} \left[ \frac{1}{4} \sum_i \sum_j p_{1i} p_{2j} \left( -\hat{a}_{3i}^\dagger \hat{a}_{4j}^\dagger + \hat{a}_{3j}^\dagger \hat{a}_{4i}^\dagger \right) |0\rangle \langle 0| \left( -\hat{a}_{3i} \hat{a}_{4j} + \hat{a}_{3j} \hat{a}_{4i} \right) \right]. \quad (3.8)$$

We then consider two separate cases. In the first, the two photons both happen to

be in the same frequency mode, so  $i = j$ ,  $\hat{a}_{3i}^\dagger \hat{a}_{4j}^\dagger = \hat{a}_{3j}^\dagger \hat{a}_{4i}^\dagger$ , and Equation 3.8 evaluates to zero. In this case, as both photons ended up with the same frequency, they were measured to have been indistinguishable upon incidence at the beamsplitter, perfect interference occurred and there was no coincidence at the detectors. On the other hand, if each photon was measured to be in a different frequency mode, then  $i \neq j$  and  $\text{Tr}(\hat{\rho} \hat{\Pi}_{2C}) = \frac{1}{2}$ . The photons no longer interfere at the beamsplitter due to their distinguishable frequencies and each simply has a one in two chance of ending up in each of the output ports. Therefore the overall probability of making a coincidence measurement with no time delay between the photons is given by

$$\begin{aligned} P_{2C}(0) &= \text{Tr}(\hat{\rho} \hat{\Pi}_{2C}) = \frac{1}{2} \sum_{i \neq j} \sum_j p_{1i} p_{2j} \\ &= \frac{1}{2} \sum_{i \neq j} p_{1i} \sum_j p_{2j} = \frac{1}{2} P(i \neq j), \end{aligned} \quad (3.9)$$

where  $P(i \neq j)$  is the probability that  $i$  is not equal to  $j$ . This in turn allows the visibility of the resulting interference effect to be found from Equation 1.16. As discussed in Section 1.8, when a long time delay,  $\tau$ , is introduced between the two photons they will never interfere regardless of the states they are in, and the coincidence probability will simply be  $P_{2C}(\tau) = 1/2$ . The visibility is then

$$V = 2 \left[ \frac{1}{2} - P_{2C}(0) \right] = 2 \left[ \frac{1}{2} - \frac{1}{2} (1 - P(i = j)) \right] = P(i = j), \quad (3.10)$$

and we see that, in order to obtain high visibility, the two states must have a high probability of being in the same mode.

In order to relate this result to the purities of the input states, the two input distributions are set to be identical, so  $p_{1i} = p_{2j}$  for all  $i = j$ , and  $\mathcal{P}_1 = \mathcal{P}_2$ . The probability of  $i = j$  is then found to be

$$P(i = j) = \sum_{i=j} p_{1i}p_{2j} = \sum_i p_{1i}^2 = \mathcal{P}_1 \quad (3.11)$$

$$\Rightarrow V = \mathcal{P}_1 = \mathcal{P}_2. \quad (3.12)$$

Therefore, for indistinguishable but mixed input states, the visibility is a measure of their purity. Pure input states are required for high visibility and conversely, high visibility demonstrates that the input states are pure. If the two states are distinguishable, it can be seen from Equation 3.11 that  $P(i = j)$  will be reduced and hence the visibility will also be degraded.

The general trends of these results can be elucidated if we further restrict the two input states to be a statistical mixture of  $n$  frequency modes each having equal probability. Therefore  $P(i = j) = \frac{n}{n^2} = \frac{1}{n}$ , which can be substituted into Equation 3.9 to give

$$P_{2C}(0) = \frac{1}{2} \left( 1 - \frac{1}{n} \right). \quad (3.13)$$

For perfect interference, we require that  $P_{2C}(0) = 0$ . It is clear from the result in Equation 3.13 that this can only be achieved if  $n = 1$ , in other words that the input states are both in a single frequency mode. This condition necessarily reduces the states in Equation 3.1 to pure states as the summations are over only one mode. Furthermore, for these equiprobable states, the visibility can be found from the

number of modes over which the input states are mixed:

$$V = 2 \left[ \frac{1}{2} - \frac{1}{2} \left( 1 - \frac{1}{n} \right) \right] = \frac{1}{n}. \quad (3.14)$$

Therefore the visibility of the HOMI dip will fall off with the inverse of the number of modes in a mixed input, and input states must be pure to give high visibility.

### 3.1 Factorability and purity

The general state from downconversion, up to the two-photon component, was derived in Section 2.1. Taking Equation 2.20, ignoring the vacuum component which will anyway be eliminated by heralding<sup>103</sup>, and dropping the efficiency coefficient, the two-photon state can be written

$$|\Psi(\omega_s, \omega_i)\rangle = \int_0^\infty d\omega_s \int_0^\infty d\omega_i f(\omega_s, \omega_i) \hat{a}_s^\dagger(\omega_s) \hat{a}_i^\dagger(\omega_i) |0\rangle, \quad (3.15)$$

where the joint spectral amplitude  $f(\omega_s, \omega_i)$  was defined as  $\alpha(\omega_s + \omega_i)\phi(\omega_s, \omega_i)$ . This is clearly a pure state, yet the joint spectral amplitude can contain correlations between the spatio-temporal degrees of freedom of the daughter photons, as was demonstrated in Section 2.3. This combination of purity and correlation causes the two-photon part of  $|\Psi(\omega_s, \omega_i)\rangle$  to be entangled in the frequency of the signal and idler photons.

In the entangled two-photon state  $|\Psi(\omega_s, \omega_i)\rangle$  written in Equation 3.15, when one photon is detected as a herald the remaining single photon will become mixed.

The only way in which the heralded photon can be projected into a pure state is if there is no entanglement in the initial state. As we will see in this section, this can only be realised by making  $f(\omega_s, \omega_i)$  factorable into a function of  $\omega_s$  multiplied by a function of  $\omega_i$  so that  $|\Psi(\omega_s, \omega_i)\rangle$  is a product state. Measuring one photon will then have no effect on the other.

The density operator for the two-photon state in Equation 3.15 is

$$\hat{\rho} = \int d\omega_s \int d\omega_i \int d\tilde{\omega}_s \int d\tilde{\omega}_i f(\omega_s, \omega_i) f^*(\tilde{\omega}_s, \tilde{\omega}_i) \hat{a}_s^\dagger(\omega_s) \hat{a}_i^\dagger(\omega_i) |0\rangle \langle 0| \hat{a}_s(\tilde{\omega}_s) \hat{a}_i(\tilde{\omega}_i). \quad (3.16)$$

In order to have a heralded single photon, one of the photons from a pair must be detected. As well as removing the vacuum term, this sums over the degrees of freedom of the measured photon and projects the remaining photon into a state that is described by the reduced density operator of  $\hat{\rho}$ . For detection of the idler photon, the reduced density operator for the signal is defined to be the partial trace over the idler's degrees of freedom<sup>25</sup>:

$$\hat{\rho}_s \equiv \text{Tr}_i(\hat{\rho}), \quad (3.17)$$

and similarly for the reduced density operator for the idler. Here only the frequency of each photon is considered explicitly and so this partial trace is found by integrating over a dummy state  $|\omega'\rangle$  that is an energy eigenstate of the idler

$$\hat{\rho}_s = \int d\omega' \langle 0| \hat{a}_i(\omega') \hat{\rho} \hat{a}_i^\dagger(\omega') |0\rangle. \quad (3.18)$$

After multiplying this out and performing the integrals over  $\omega_i$  and  $\tilde{\omega}_i$ , the reduced density operator for the signal photon is

$$\hat{\rho}_s = \int d\omega_s \int d\tilde{\omega}_s f_s(\omega_s, \tilde{\omega}_s) \hat{a}_s^\dagger(\omega_s) |0\rangle \langle 0| \hat{a}_s(\tilde{\omega}_s), \quad (3.19)$$

where the function describing the frequency distribution of the signal photon is given by

$$f_s(\omega_s, \tilde{\omega}_s) = \int d\omega' f(\omega_s, \omega') f^*(\tilde{\omega}_s, \omega'). \quad (3.20)$$

It is apparent that  $\hat{\rho}_s$  will only describe a pure state if the function  $f_s(\omega_s, \tilde{\omega}_s)$  is factorable so that Equation 3.19 can be rewritten with  $f_s(\omega_s, \tilde{\omega}_s) = g_s(\omega_s) g_s^*(\tilde{\omega}_s)$ . However, this will only be the case for all  $\omega'$  if the function  $f(\omega_s, \omega')$  is also factorable such that  $f(\omega_s, \omega') = g_s(\omega_s) h(\omega')$  and Equation 3.20 reduces to

$$f_s(\omega_s, \tilde{\omega}_s) = g_s(\omega_s) g_s^*(\tilde{\omega}_s) \int d\omega' h(\omega') h^*(\omega'). \quad (3.21)$$

This requirement of factorability in  $f(\omega_s, \omega')$  to prepare a pure reduced state is equivalent to the same constraint of factorability on the initial joint amplitude function. Therefore, for pure heralded single photons the initial two photon state must satisfy

$$f(\omega_s, \omega_i) = g_s(\omega_s) g_i(\omega_i). \quad (3.22)$$

This means that all frequency correlations, and by extension all correlations, in the initial state are eliminated.

### 3.1.1 A brief note on notation

In the previous section, it was demonstrated that factorability in the two-photon amplitude is required for the heralding of pure single photons directly from a source of photon pairs. This condition can clearly never be achieved with plane-wave pumped type-I PDC, but, as we will see, the additional flexibility of type-II phasematching allows a greater degree of control over the parameters of the source. Therefore all of the remainder of this thesis refers to type-II downconversion and hence the signal and idler are re-designated to be e-ray and o-ray to avoid any confusion. All the crystals considered herein are negative uniaxial, and therefore the pump will always be e polarised. To remind the reader of this, henceforth the pump, e-ray, and o-ray photons' wavevectors will be expressed as  $k_e(\omega_p)$ ,  $k_e(\omega_e)$ , and  $k_o(\omega_o)$  respectively. Note that  $\omega_o$ , the o-ray frequency, is distinct from  $\omega_0$ , the central downconversion frequency. Both theoretically and experimentally, the condition is enforced that all collected downconversion is (at least approximately) collinear and therefore correlations in transverse momentum are small. Furthermore it is assumed that the heralded photons will eventually have their transverse degrees of freedom constrained by a single-mode fibre and therefore the discussion of factorability is restricted to the frequency degree of freedom.

## 3.2 Calculating photon pair correlations

### 3.2.1 The Schmidt decomposition

Given that the initial two-photon state from PDC is required to be uncorrelated to prepare pure heralded single photons, it is essential to have an accurate method of quantifying exactly how factorable the joint state is and hence predicting for a given state what level of purity can be expected in the heralded photons. The most intuitive method for doing this is through the Schmidt decomposition of the two-photon state<sup>104,105</sup>.

The Schmidt decomposition is a unique method of expressing a bipartite system in terms of a complete set of basis states. For example, the Schmidt decomposition of the two-photon state in Equation 3.15 can be found by expressing  $|\Psi(\omega_e, \omega_o)\rangle$  as a linear superposition of product states:

$$|\Psi(\omega_e, \omega_o)\rangle = \sum_j \sqrt{\lambda_j} |\zeta_j(\omega_e)\rangle |\xi_j(\omega_o)\rangle, \quad (3.23)$$

where the coefficients  $\lambda_n$  are real, non-negative, and normalized such that

$$\sum_j \lambda_j = 1. \quad (3.24)$$

The orthonormal basis states  $|\zeta_j(\omega_e)\rangle$  and  $|\xi_j(\omega_o)\rangle$  are known as Schmidt modes; each set is dependent on only one subsystem of  $|\Psi(\omega_e, \omega_o)\rangle$ . The number of elements required in the sum to express  $|\Psi(\omega_e, \omega_o)\rangle$  in terms of the Schmidt modes then

indicates the degree of factorability of the two-photon state. This can be quantified by the Schmidt number,  $K$ <sup>106</sup>, defined as<sup>107</sup>

$$K \equiv \frac{1}{\sum_j (\lambda_j^2)} \equiv \frac{1}{\text{Tr}\{(\hat{\rho}_e)^2\}} \equiv \frac{1}{\text{Tr}\{(\hat{\rho}_o)^2\}}, \quad (3.25)$$

where  $\hat{\rho}_e$  and  $\hat{\rho}_o$  are the reduced density operators for the e- and o-ray photons.  $K$  is a measure of how many frequency Schmidt modes are active in the two-photon state and hence it is an entanglement measure. A factorable product state will be unentangled and can be described using only one pair of Schmidt modes; therefore it will have  $\lambda_1 = 1, \lambda_{j>1} = 0$  and  $K$  equal to unity. A state maximally entangled in frequency would require an infinite number of Schmidt modes to describe it, each with a vanishingly small  $\lambda_j$  coefficient, and therefore  $K$  would equal infinity.

From Equation 3.25 and the definition of purity given in Equation 1.7 we also see that  $(1/K)$  yields the purity of either reduced state. Therefore the Schmidt decomposition of the initial two-photon state can be employed to predict the purity of the heralded single photons. This provides another way of demonstrating that the joint amplitude must be factorable to produce pure states. A pure single daughter photon requires  $K = 1$  — a condition that can only be satisfied through  $|\Psi(\omega_e, \omega_o)\rangle$  being a product state and the photons being prepared in a single pair of modes. Therefore  $f(\omega_e, \omega_o)$  must be factorable.

### 3.2.2 The singular value decomposition

There are only certain limited classes of states for which it is possible to calculate the Schmidt decomposition analytically (see Section 3.4), yet it would be convenient if the value of  $K$  could be calculated for any arbitrary two-photon state<sup>108</sup>. Fortunately, there exists a matrix operation that is the analog of the Schmidt decomposition and can be computed numerically for any input state.

Let the state  $|\psi(\omega_e, \omega_o)\rangle$  be represented by the square matrix  $F$  where  $F_{mn}$  is the matrix element representing  $f(\omega_{e,m}, \omega_{o,n})$  and  $\omega_{e,m}$  and  $\omega_{o,n}$  are discrete frequencies of the e-ray and o-ray respectively. The singular value decomposition (SVD) of  $F$  is then defined as the decomposition of  $F$  into three matrices, two of which are unitary,  $U$  and  $V^\dagger$ , and one diagonal,  $D$ , such that

$$F = UDV^\dagger. \quad (3.26)$$

The unitary matrices then contain the modes into which the initial state has been decomposed.  $U$  is dependent only on  $\omega_e$  and its  $j^{\text{th}}$  column,  $U_{mj}$ , where  $j$  is held constant over e-ray frequency index  $m$ , represents the e-ray Schmidt mode  $|\zeta_j(\omega_e)\rangle$  while  $V^\dagger$  depends only on  $\omega_o$  and the  $j^{\text{th}}$  row  $V_{jn}^\dagger$  describes the o-ray Schmidt mode  $\langle \xi_j(\omega_o) |$ . The diagonal elements of  $D$  are called the singular values of  $F$ ; they are non-negative and entered in descending order of magnitude. It can be seen by multiplying out the three matrices on the right hand side of Equation 3.26 that each element of  $D$  describes how much of each of the modes listed in  $U$  and  $V^\dagger$  are mixed

at each pair of e-ray and o-ray frequencies to form  $F$ . Therefore the elements of  $F$ , specifying the amplitude at every pair of frequencies, each contain a sum over all  $j$  mode pairs.

The singular values can be swiftly calculated for relatively large matrices by numerical means (for example in Matlab) and the value of the Schmidt number found simply by normalizing  $D$  and summing the squares of the elements. This technique is particularly powerful as the Schmidt number can be determined quickly even for states for which an analytical solution to the Schmidt decomposition does not exist.

### 3.3 Correlated two-photon states and filtering

All downconversion sources demonstrated to date have exhibited strong pairwise correlations between the daughter photons<sup>109–111</sup>. Indeed, many experimentalists have sought to maximise these correlations to create highly entangled photon pairs<sup>91,112–114</sup> ideal for use in applications such as quantum key distribution<sup>115–118</sup> or quantum state teleportation<sup>119–122</sup>. However, all sources exhibiting correlations are useless for generating pure single photons.

The typical example of a downconverted two-photon state shown in Figure 2.9, in this case generated by pulsed pumping at 400 nm of a 2 mm BBO crystal cut for collinear type-II phasematching, exhibits clear correlations between the frequencies of the daughter photons. These correlations preclude the direct generation of pure heralded single photons, yet several experiments have been performed where

heralded single photons from two such sources (either BBO or another source that produces correlated states) are interfered with reasonable visibility<sup>80–83</sup>. This is brought about by the “brute force” method of heralded single photon generation, that of spectral filtering<sup>123</sup>.

The action of filtering is to throw away most of the photons that display pairwise correlations with no attempt made to remove these correlations at the point of production. Therefore it is very lossy as the majority of the pairs produced in any given time window have to be discarded from the ensemble in order for the remainder to be able to approximate an uncorrelated state. Photons in correlated pairs of modes are removed from the ensemble to leave something that approximates single mode behaviour<sup>124</sup>.

This situation can be modelled by assuming that the filters have Gaussian transmission functions, though the specific form of the filter function makes little difference to the results of the calculation. These spectral transmission functions are given by

$$g_S(\omega_\mu) = \sqrt[4]{\frac{2}{\pi\sigma_S^2}} \exp\left[-\left(\frac{\omega_\mu - \omega_0}{\sigma_S}\right)^2\right], \quad (3.27)$$

where  $\mu = e, o$  and  $\sigma_S$  is the filter width, defined in a similar manner to  $\sigma$  in Equation 2.38. The joint two-photon amplitude directly from the downconversion crystal is then multiplied by one or two of these filter transmission functions — corresponding to a filter in one or both output arms — to produce the final filtered joint amplitude. The purity of the heralded single photons from this source can then be found by taking the numerical SVD of the final state.

Figures 3.1 and 3.2 demonstrate the effect of applying a narrowband spectral filter to one or both photons of the correlated two-photon state from type-II BBO. The purity of the heralded photons is plotted as a function of the filter bandwidth along with two other figures of merit for the source. The first is the theoretical maximum heralding efficiency of each source, defined<sup>125</sup> for perfect detectors as the ratio of the coincidence count rate,  $R_C$ , to the count rate at the trigger detector,  $R_T$ :

$$\eta_H = \frac{R_C}{R_T}. \quad (3.28)$$

This corresponds to the heralded photon from one pair being available given that its twin has been detected. It can be calculated in the case of a filtered source as the ratio of the integral of the joint spectral intensity with the filter only on the trigger arm to that with filters in both arms. The second is the normalized overall coincidence count rate for the source, defined as the integral of the final filtered joint spectrum over the integral of the initial state. It is clear that for both filtering configurations, filtering increases the purity of the heralded photons; indeed this purity can be made arbitrarily close to unity by reducing the filter bandwidth. However, such filtering comes at a price, either in the overall count alone or both the overall count rate and the heralding efficiency.

With a filter in the trigger arm only, the heralding efficiency is not affected as the signal photon will in theory definitely be useable. However, the overall coincidence count rate is reduced due to the cut in the trigger rate. In the case of BBO, as the joint spectrum is broader in the o-ray than the e-ray, the reduction in overall count

rate will be minimised by filtering only the e-ray in preference to filtering only the o-ray, as the proportion of photons let through a filter in the e-ray arm alone will be greater than if the same filter were put in the o-ray arm only. This is the situation depicted in Figure 3.1; the e-ray only is filtered and these filtered photons are used as the heralds. Even though  $\eta_H$  is not reduced, if this type of source were used to generate high-purity heralded photons, the overall coincidence count rate would be very small because the filter bandwidth required to get to a high level of purity is so narrow that the count rate in the trigger arm would be tiny. For example, to prepare heralded single photons with a purity of 0.95 the filter bandwidth could not be greater than 1 nm and would pass only 11% of the generated photon pairs.

On the other hand, by filtering both arms, although the filter bandwidth needed to attain the same purity is much less narrow, the heralding efficiency would be necessarily reduced as many of the signal photons would have to be discarded and hence even in theory only a small proportion of them would be available. The broader o-ray bandwidth of the joint spectrum from BBO also gives a preferential scheme for this filtering configuration: the better heralding efficiency is obtained by using the o-ray as a herald rather than the e-ray. By cutting out proportionally more photons in the trigger arm the fraction that are thrown away in the heralding arm can be made as small as possible and hence the heralding efficiency obtained is as high as it can be. Even so, for a required purity of 0.95 in the heralded e-ray photons, the maximum possible heralding efficiency is reduced to 0.75 at a filter bandwidth of 4 nm, passing 12% of the generated pairs. This is shown in Figure 3.2.

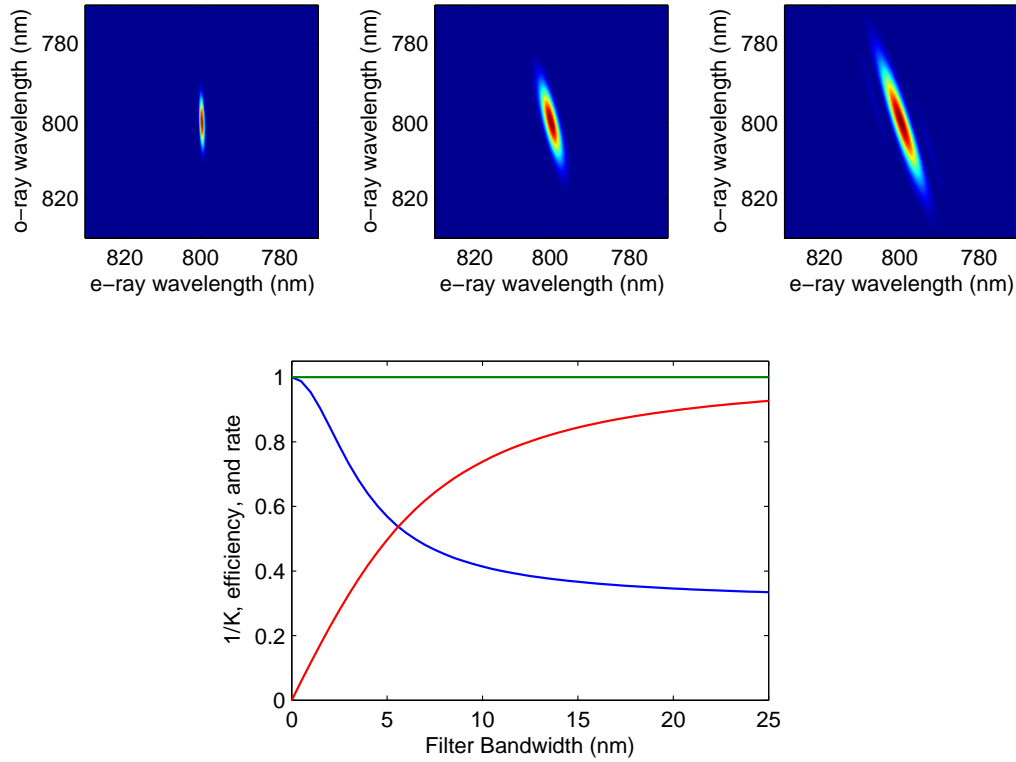


**Figure 3.1** Demonstration of the effects of filtering only the e-ray from a 2 mm long collinear type-II BBO PDC source pumped at 400 nm with a pump bandwidth of 4 nm. The top three plots illustrate the joint spectra for filter bandwidths of 1 nm (left), 5 nm (centre), and 25 nm (right). The bottom plot shows the effect of filtering on the inverse Schmidt number (blue, equal to the heralded purity), the heralding efficiency (green), and the normalised coincidence count rate (red).

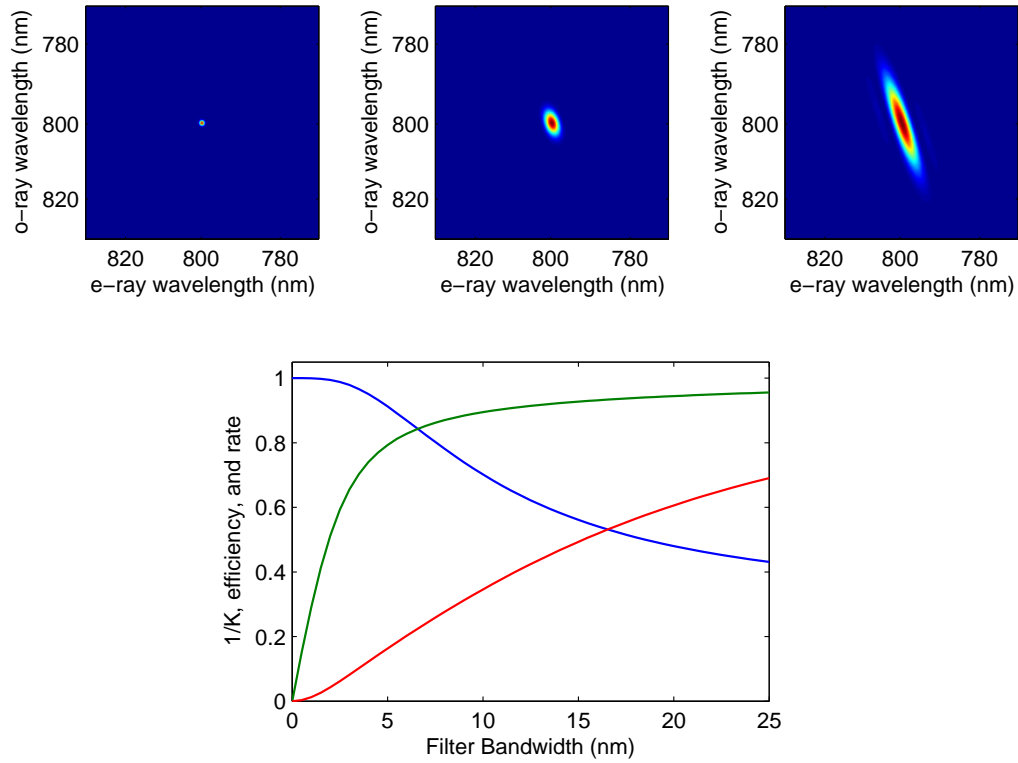


**Figure 3.2** Demonstration of the effects of filtering both arms of a 2 mm long collinear type-II BBO PDC source pumped at 400 nm with a pump bandwidth of 4 nm. The top three plots illustrate the joint spectra for filter bandwidths of 1 nm (left), 5 nm (centre), and 25 nm (right). The bottom plot shows the effect of filtering on the inverse Schmidt number (blue), the heralding efficiency (green), and the normalised coincidence count rate (red).

When considering only one PDC source generating one pair of photons at a time, filtering is not a huge problem in terms of the count rates expected. For example, if the necessary filtering for the level of purity required from a spectrally-correlated source means that one must use a filter that has a 50% overall probability of transmitting each photon (summed across the entire bandwidth of both the filter and the photons), then the likelihood of a pair being transmitted is still a quarter. However, filtering does become more of an obstacle if one wants to perform an experiment requiring the delivery of two pairs, either from one source or in independent sources. In this case, the probability of having two pairs available after filtering given that two were generated (itself a relatively unlikely event) is only 6%.

Nevertheless, some impressive experiments requiring the generation of at least two pairs in sources that must use filtering have recently been demonstrated. Among these proof-of-principle experiments are the implementation of optical quantum gates<sup>126</sup>, linear optics quantum computation<sup>127</sup>, and cluster state quantum computation<sup>128</sup>. Furthermore, parametric downconversion sources have been used to generate entanglement between more than two photons<sup>82,129</sup>, demonstrate entanglement swapping between two pairs<sup>130</sup>, and build “Schrödinger cat” states<sup>131,132</sup> — superpositions of quasi-classical states.

Experiments with two pairs are already pushing the limits of what can be achieved with a correlated PDC source, but filtering becomes a far more serious problem when moving to higher photon numbers. The probability of having  $n$  pairs available after filtering given that  $n$  pairs were generated goes as the  $(2n)^{\text{th}}$  power

of the filter transmission. For the same filtering regime yielding photons of the same purity as before, the probability of having four pairs transmitted is less than half a percent. Hence filtering is not scalable to higher photon numbers and a more effective approach to pure-state photon preparation must be found.

### 3.4 Generation of factorable states

A more elegant approach to preparing pure heralded single photons would be to generate photon pairs directly in factorable states. If this could be achieved there would be no need for lossy spectral filters and no longer any fundamental tradeoff of the purity of the single photon states against the heralding efficiency and count rates. Several methods have to date been proposed for the management of correlations created between pairs of downconverted photons at the point of production. These are mostly based on manipulating the spectra of the downconverted pairs through the phasematching conditions either by changing the structure of the pump beam or engineering the dispersion characteristics of the source itself, or a combination of both. Techniques primarily reliant on pump control include the angular dispersion of the pump beam from a grating before sending it through the source<sup>133–135</sup>; this alters the phasematching conditions at different angles and is known as achromatic phasematching. A similar situation will be revisited in Chapter 4. The spectral structure can also be affected by altering the spatial profile of the pump beam and the geometry of the phasematched output<sup>136,137</sup>. A side-pumped waveguided downconversion source generating counter-propagating photons was proposed to per-

mit photon-pair generation with arbitrary spectra<sup>138,139</sup> but this inevitably results in a very short interaction length between the pump and the nonlinear medium. Additionally, control of the spatial emission pattern has been studied through the spatial profile of the pump<sup>140</sup> and microstructuring the nonlinear medium to alter the phasematching conditions<sup>141</sup>.

However, none of these techniques has yet shown the ability to generate the factorable states required for pure heralded single photon preparation. Nevertheless, there exists one approach to spectral engineering specifically proposed with the idea of tailoring the joint spectrum from a downconverter to minimise the correlations between the daughter photons in mind. This was first expounded by Grice *et al*<sup>102</sup> and is outlined in this section.

To see how factorable state generation might be accomplished, let us return to the two-photon state in Equation 3.15. The product of the pump function with the phasematching function can be simplified by approximating the sinc function in Equation 2.21 with a Gaussian as follows:

$$\phi(\omega_e, \omega_o) = e^{\frac{i\Delta k L}{2}} \operatorname{sinc}\left(\frac{\Delta k L}{2}\right) \approx e^{\frac{i\Delta k L}{2}} \exp\left[-\gamma\left(\frac{\Delta k L}{2}\right)^2\right], \quad (3.29)$$

where the constant  $\gamma = 0.193$  is set to match the FWHM bandwidth of the Gaussian to that of the sinc function. A further simplification is to make an approximation of the wavevector mismatch,  $\Delta k \approx \Delta k_0$ , by taking the Taylor expansion of the three wavevectors for pump, signal, and idler about the degenerate central downconver-

sion frequency  $\omega_0$ . Only terms up to the second order are retained, and breaking this down into the zeroth, first, and second order contributions to the wavevector mismatch we have

$$\Delta k_0 = \Delta k_0^{(0)} + \Delta k_0^{(1)} + \Delta k_0^{(2)}. \quad (3.30)$$

Due to phasematching at the central frequency, the zeroth order contribution disappears:

$$\Delta k_0^{(0)} = k_e(2\omega_0) - k_e(\omega_0) - k_o(\omega_0) = 0, \quad (3.31)$$

and the first order contribution is expressed as

$$\Delta k_0^{(1)} = k'_e(2\omega_0)(\omega_p - 2\omega_0) - k'_e(\omega_0)(\omega_e - \omega_0) - k'_o(\omega_0)(\omega_o - \omega_0), \quad (3.32)$$

where prime denotes differentiation with respect to angular frequency. The frequency detunings are now replaced with two new variables,  $\nu_e = \omega_e - \omega_0$  and  $\nu_o = \omega_o - \omega_0$ , and using the energy conservation condition (Equation 2.23) we have

$$\begin{aligned} \Delta k_0^{(1)} &= [k'_e(2\omega_0) - k'_e(\omega_0)] \nu_e + [k'_e(2\omega_0) - k'_o(\omega_0)] \nu_o \\ &= a_e \nu_e + a_o \nu_o, \end{aligned} \quad (3.33)$$

where the new coefficients are the mismatches between the inverse group velocities

of the pump and daughter fields, given by

$$a_e = k'_e(2\omega_0) - k'_e(\omega_0), \quad a_o = k'_e(2\omega_0) - k'_o(\omega_0). \quad (3.34)$$

Similarly for the second order contribution to the wavevector mismatch we have

$$\begin{aligned} \Delta k_0^{(2)} &= \frac{1}{2}k''_e(2\omega_0)(\omega_p - 2\omega_0)^2 - \frac{1}{2}k''_e(\omega_0)(\omega_e - \omega_0)^2 - \frac{1}{2}k''_o(\omega_0)(\omega_o - \omega_0)^2 \\ &= \frac{1}{2} [k''_e(2\omega_0) - k''_e(\omega_0)] \nu_e^2 + \frac{1}{2} [k''_e(2\omega_0) - k''_o(\omega_0)] \nu_o^2 + k''_e(2\omega_0)\nu_e\nu_o \\ &= \frac{1}{2}b_e\nu_e^2 + \frac{1}{2}b_o\nu_o^2 + b_{eo}\nu_e\nu_o, \end{aligned} \quad (3.35)$$

where

$$b_e = k''_e(2\omega_0) - k''_e(\omega_0), \quad b_o = k''_e(2\omega_0) - k''_o(\omega_0), \quad b_{eo} = k''_e(2\omega_0). \quad (3.36)$$

A good approximation to the phasematching function close to  $\omega_0$  can then be formed by the substitution of these expansions into Equation 3.30 and thence Equation 3.29.

The resulting approximation of  $\phi(\omega_e, \omega_o)$  can be further simplified by analyzing where correlations in the two-photon state will arise. As we care only about constructing a factorable state, terms that will not under any circumstances lead to correlations can be abandoned. However, we must contemplate not only correlations in the spectral domain (contained in the real part of the joint amplitude), but also temporal correlations that can be “hidden” in the phase of the joint amplitude. A linear phase term in Equation 3.29 will not lead to temporal correlations as it would

only cause a shift of the Fourier transform of  $f(\omega_e, \omega_o)$ , whereas a quadratic phase term would cause a tilt in the joint temporal distribution. Therefore we need only consider the second order terms in the imaginary exponent. Conversely, as the real exponent gets squared, only the first order terms are required as the square of these will dominate over the vanishingly small effects of the second order terms squared. Therefore the approximation to the phasematching function can be reduced to

$$\phi(\nu_e, \nu_o) = \exp \left[ i \frac{L}{4} (b_e \nu_e^2 + b_o \nu_o^2 + 2b_{eo} \nu_e \nu_o) - \gamma \frac{L^2}{4} (a_e \nu_e + a_o \nu_o)^2 \right]. \quad (3.37)$$

The pump function (Equation 2.36) can also be written in terms of the new detunings  $\nu_e$  and  $\nu_o$ . If we assume a quadratic phase on the pump, given by  $\varphi_2/2$  then we have

$$\alpha(\nu_e + \nu_o) = \exp \left[ -i \frac{\varphi_2}{2} (\nu_e + \nu_o)^2 - \left( \frac{\nu_e + \nu_o}{\sigma} \right)^2 \right]. \quad (3.38)$$

The approximate joint spectral amplitude is then

$$\begin{aligned} f(\nu_e, \nu_o) &\approx \exp \left[ \left\{ i \left( \frac{L}{4} b_e - \frac{\varphi_2}{2} \right) - \left( \gamma \frac{L^2}{4} a_e^2 + \frac{1}{\sigma^2} \right) \right\} \nu_e^2 \right] \\ &\exp \left[ \left\{ i \left( \frac{L}{4} b_o - \frac{\varphi_2}{2} \right) - \left( \gamma \frac{L^2}{4} a_o^2 + \frac{1}{\sigma^2} \right) \right\} \nu_o^2 \right] \\ &\exp \left[ \left\{ i \left( \frac{L}{2} b_{eo} - \varphi_2 \right) - \left( \gamma \frac{L^2}{2} a_e a_o + \frac{2}{\sigma^2} \right) \right\} \nu_e \nu_o \right] \\ &= \exp \left[ -i (n_e \nu_e^2 + n_o \nu_o^2 + n_{eo} \nu_e \nu_o) - (m_e \nu_e^2 + m_o \nu_o^2 + m_{eo} \nu_e \nu_o) \right] \end{aligned} \quad (3.39)$$

where the e-ray coefficients are given by

$$m_e = \gamma \frac{L^2}{4} a_e^2 + \frac{1}{\sigma^2}, \quad n_e = \frac{L}{4} b_e - \frac{\varphi_2}{2}, \quad (3.40)$$

and similarly for the o-ray and crossed term coefficients. All the spectral correlations are contained within the real part of this function, and temporal correlations arise from this real part and its associated phase.

Considering firstly the spectral correlations alone, the joint spectral intensity,  $|f(\nu_e, \nu_o)|^2$ , is a two dimensional Gaussian distribution whose aspect ratio is set by the magnitudes of  $m_e$  and  $m_o$  and whose tilt is dependent on  $m_{eo}$ . It is this tilt that causes spectral correlation. A new parameter,  $\varrho$ , can be defined in terms of these  $m$  coefficients as follows

$$-2 < \varrho = \frac{m_{eo}}{\sqrt{m_e m_o}} < 2. \quad (3.41)$$

When  $\varrho = 0$  then the joint spectral intensity will have no tilt and therefore no correlations in frequency.

This can be generalized to the construction of a two-photon state with neither spectral nor temporal correlations. If we set  $m_{eo} = n_{eo} = 0$  and hence discard the last exponential in Equation 3.39 then both the phase and magnitude of  $f(\nu_e, \nu_o)$  are factorable into a function only of  $\nu_e$  multiplied by a function of  $\nu_o$  alone. A two-photon state with this factorable joint amplitude would have no correlations between the e-ray and o-ray frequencies or emission times. All the correlations arise from the exponent containing crossed terms in  $\nu_e$  and  $\nu_o$  and it is this exponent that

must be made zero to enable factorable state generation.

In most realistic situations, the magnitude of  $n_{eo}$  is sufficiently small that temporal correlations resulting from the phase of  $f(\nu_e, \nu_o)$  have little appreciable impact on the overall level of correlation of the two-photon state compared to the effect of correlations in the amplitude of  $f(\nu_e, \nu_o)$ . Certainly it is primarily spectral correlations with which the experimentalist must be concerned to achieve something approaching a factorable state. If additional factorability is desired after the spectral domain has been taken care of, the phase of the pump pulse,  $\varphi_2/2$ , can be adjusted using a prism line to impart negative dispersion and set  $n_{eo}$  to be exactly zero. This corresponds to the pump pulse being exactly transform-limited when it reaches the mid-point of the crystal<sup>101</sup>. However, this level of control is not required for the experiments presented herein and the remainder of this section will deal with eliminating solely spectral correlations. The question of phase on the joint spectrum will be revisited later.

So how is it possible to achieve  $m_{eo} = 0$ ? Using Equations 3.33 and 3.39, the full expression for the coefficient required to be zero is

$$m_{eo} = \gamma \frac{L^2}{2} [k'_e(2\omega_0) - k'_e(\omega_0)] [k'_e(2\omega_0) - k'_o(\omega_0)] + \frac{2}{\sigma} = 0. \quad (3.42)$$

The mechanics of phasematching in a standard birefringent crystal allow two methods of fulfilling this condition. The dispersion relations make it possible to adjust the relative values of  $k'_e(2\omega_0)$ ,  $k'_e(\omega_0)$ , and  $k'_o(\omega_0)$  by selecting the phasematched down-

conversion wavelengths via the crystal orientation and pump wavelength. It is on this principle that both methods of factorable state generation in bulk media are based. The first method concerns the situation where the derivative of the pump wavevector lies between those of the two daughter photons:  $k'_e(\omega_0) < k'_e(2\omega_0) < k'_o(\omega_0)$ . By taking the inverse of this inequality it can be seen that it corresponds to a condition on the group velocities of the three fields. The group velocity is defined to be

$$v_g = \frac{\partial\omega}{\partial k(\omega)} = \frac{1}{k'(\omega)} \quad (3.43)$$

and therefore the group velocity of the pump must be between those of the two daughter photons. This demonstrates why, in the collinear case, it is important to have the flexibility offered by type-II phasematching, as this condition clearly could never be met in a type-I system. If the condition is fulfilled, the first term in Equation 3.42 will now be negative and the following equality between the crystal length and pump bandwidth must be satisfied:

$$L = \frac{2}{\sigma\sqrt{\gamma a_e a_o}}. \quad (3.44)$$

So long as this condition is fulfilled, the resulting joint spectral intensity will be factorable.

This can be thought of graphically in terms of the plots of the two-photon joint spectrum first presented in Section 2.3. Methods that result in factorable states rely on manipulating the phasematching function in a particular manner that negates

the negative correlations introduced by the pump envelope function. The situation considered immediately above equates to juxtaposing the negative slope of the pump function with a positively-correlated phasematching function. By matching the bandwidth of the pump to that of the crystal using the relationship in Equation 3.44, one can end up with a state that is factorable in frequency. The phasematching function will be orientated at  $45^\circ$  if the pump group velocity is exactly half way between those of the two daughter photons — this is known as the symmetric group velocity matching condition.

This is demonstrated in Figure 3.3. For BBO, the group velocity of an e-ray at 800 nm is approximately the average of the group velocities of an e-ray and an o-ray at  $1.6 \mu\text{m}$ . This results in a positively-correlated phasematching function, and this is shown in the figure for a 2 mm long BBO crystal cut for type-II phasematching at  $1.6 \mu\text{m}$  ( $\theta_{pm} = 28.9^\circ$ ). By pumping this crystal with ultrafast pulses at 800 nm and setting the bandwidth of the pulses to be 14 nm, the condition for factorability is satisfied. The state resulting from the multiplication of these two functions is roughly circular, as illustrated in the figure. For a perfectly circular joint spectral intensity, the group velocity of the pump must be the average of the group velocities of the downconverted photons. This situation also illustrates the importance of using a broadband pulsed pump laser as the bandwidth of the pump must match that of the crystal to ensure factorability. In this case, there are no spectral correlations and the joint spectral intensity is factorable. Another helpful feature of the exponential approximation to the phasematching function and truncated expansion of the phase

mismatch is that it allows one to take the analytic Fourier transform of the spectral amplitude and hence find the joint temporal intensity. This is also plotted in Figure 3.3 and demonstrates that, for a pump with flat spectral phase, there are also no temporal correlations in the approximate state.

The second method of making  $m_{eo} = 0$  is also reliant on having a broadband pump, in fact one that is broadband enough relative to the bandwidth of the phase-matching function that

$$\gamma L^2 \gg \frac{4}{\sigma} \quad (3.45)$$

and the term in Equation 3.42 containing the inverse of the pump bandwidth can be ignored. Therefore, for a broadband pump and long crystal (with its associated small phasematching bandwidth),  $m_{eo}$  can be approximated by

$$m_{eo} \approx \gamma \frac{L^2}{2} [k'_e(2\omega_0) - k'_e(\omega_0)] [k'_e(2\omega_0) - k'_o(\omega_0)]. \quad (3.46)$$

It is clear that this can be set to zero by making the group velocity of either the e- or the o-ray downconverted field equal to that of the pump. In the case of downconversion in a uniaxial crystal, this must be done by matching the group velocities of the pump and the o-ray daughter photon. Therefore, o-ray photons will propagate through the crystal alongside the pump while e-ray photons will “walk off” temporally from the pump due to their different group velocity. Hence this is known as asymmetric group velocity matching.

The particular phasematching function for this situation will be broadband in the

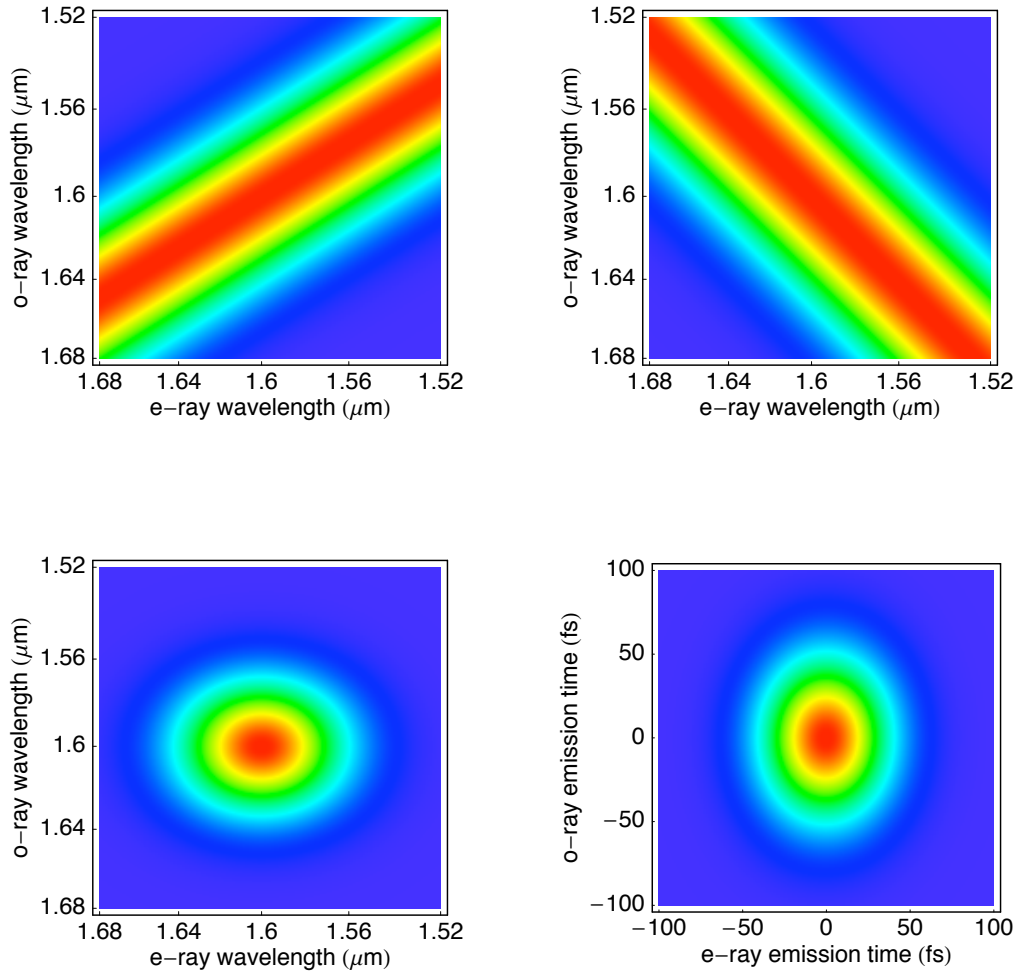


**Figure 3.3** Factorable state generation in BBO. Exponential approximation to phasematching intensity centered at  $1.6 \mu\text{m}$  (top left) and pump intensity distribution for 14 nm bandwidth (top right). Resulting joint spectral intensity (bottom left) and joint temporal probability distribution (bottom right) both of which are completely factorable.

frequency of the group velocity matched o-ray and much narrower in the frequency of the e-ray photon. The phasematching function does not exhibit any tilt; it is “vertical” when plotted as a function of e- and o-ray frequency, and it is this that can make the two-photon state uncorrelated. The pump envelope function must be sufficiently broadband to allow this phasematching function to dominate the form of the joint state.

This gives the general framework describing the basic conditions that need to be satisfied to generate factorable states. For the approximate forms of the two-photon states considered in this section, it is possible to find their analytic Schmidt decompositions and hence quantify any correlations. Although this would appear at first to be a very useful technique, in fact it is less insightful than one might imagine. These approximate, plane-wave two-photon states with flat phase do not describe accurately enough the situation encountered in experiments, where the joint spectra have curvature from third and higher order components of the wavevector mismatch. Additionally any structure in or focusing of the pump beam can have a dramatic impact on the overall factorability. Therefore the numerical singular value decomposition of the exact two-photon state is often more appropriate.

Nonetheless, a brief investigation of the analytic Schmidt decomposition for such states is justified to give some insight into how the technique works. Finding the Schmidt decomposition requires the solution of a pair of integral eigenvalue equa-

tions<sup>104</sup>

$$\begin{aligned}\int d\omega' \int d\omega_o f(\omega_e, \omega_o) f^*(\omega', \omega_o) \zeta_n(\omega') &= \lambda_n \zeta_n(\omega_e) \\ \int d\omega' \int d\omega_e f(\omega_e, \omega_o) f^*(\omega_e, \omega') \xi_n(\omega') &= \lambda_n \xi_n(\omega_o).\end{aligned}\quad (3.47)$$

The solutions to these equations for the type of state in Equation 3.39 with the complex exponential set to zero are given by Hermite polynomials<sup>102</sup> that can be written in the form<sup>142</sup>

$$\begin{aligned}\sqrt{1-\mu^2} \sum_{n=0}^{\infty} \mu^n \zeta_n(\alpha_1 x_1) \xi_n(\alpha_2 x_2) \\ = \exp \left[ -\frac{1+\mu^2}{2(1-\mu^2)} (\alpha_1^2 x_1^2 + \alpha_2^2 x_2^2) + \frac{2\mu}{1-\mu^2} \alpha_1 \alpha_2 x_1 x_2 \right].\end{aligned}\quad (3.48)$$

By equating coefficients between this expression and Equation 3.39 a quadratic equation relating  $\mu$  and the  $m$  coefficients can be found. Substituting the definition of  $\varrho$  in Equation 3.41 into the solution for  $\mu$  gives

$$\mu = \frac{-2 + \sqrt{4 - \varrho^2}}{\varrho},\quad (3.49)$$

which tends to 1 as  $\varrho$  tends to zero. The magnitudes of the Schmidt modes,  $\lambda_n$ , can then be described by comparing Equation 3.48 to the definition of the Schmidt decomposition given in Equation 3.23:

$$\lambda_n = (1 - \mu^2) \mu^{2n}.\quad (3.50)$$

Therefore, by calculating the  $m$  coefficients from the Sellmeier equations of a given nonlinear crystal and the pump bandwidth, it is possible for this type of state to find the magnitudes of the Schmidt modes directly and hence quantify the degree of correlation from the number of active modes. In this case the Schmidt number is

$$K = \frac{1 + \mu^2}{1 - \mu^2}, \quad (3.51)$$

obtained by summing the Schmidt mode magnitudes from zero to infinity.

We can now compare the factorability of a two-photon state approximating that plotted in Figure 2.9 for type-II phasematched BBO pumped at 400 nm with that of the uncorrelated state from BBO pumped at 800 nm. The magnitudes of the Schmidt modes for both states are shown in Figure 3.4. For the correlated state, the probability of finding the photon pair in the lowest order mode is just over 50%, and  $K = 2.89$ , showing that the emission is multimode in character. Heralded single photons from this state would be mixed, and the only way to get good interference visibility would be to sacrifice count rates and use spectral filters. However, in the case of the uncorrelated state, due to the conditions set on the parameters defining the spectral structure,  $\rho$  is equal to zero and therefore  $K = 1$ . The emission is into a single spectral mode and heralded pure single photons could be generated directly without any filtering.

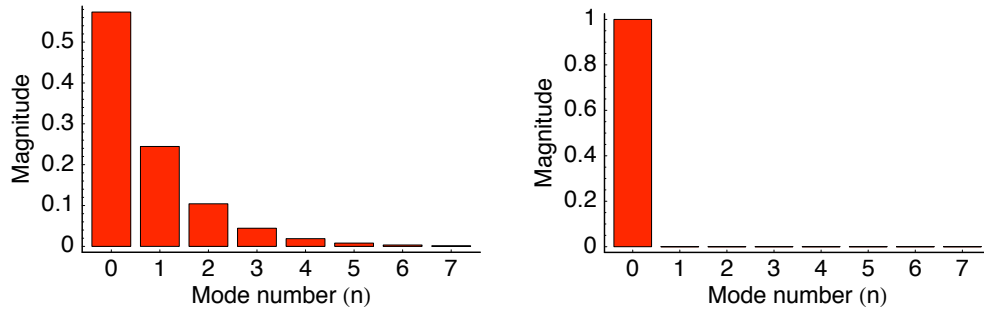


**Figure 3.4** Magnitudes of the first eight Schmidt coefficients for the approximate state generated by collinear type II BBO pumped at 400 nm (left, state is an approximation to that in Figure 2.9) and 800 nm (right, state as in Figure 3.3).

### 3.4.1 KDP and factorable two-photon states

The factorable state formed by symmetric group velocity matching in BBO studied in the previous sections has the advantage that it can be pumped with a standard femtosecond titanium:sapphire laser at 800 nm. However, the main disadvantage is that the pairs generated cannot be detected using silicon-based single photon detectors as these are not sensitive to light at  $1.6 \mu\text{m}$ . Instead the only widely available solid-state detectors suitable at this wavelength are much less efficient indium-gallium-arsenide-based devices. This emphasizes the point that, for each particular nonlinear crystal, the conditions for factorability can only be fulfilled over a certain range of wavelengths<sup>102</sup> and, for most crystals, this puts the downconverted photons beyond the useful range of silicon photodetectors (up to about  $1 \mu\text{m}$ ).

Therefore it is essential to select the correct nonlinear crystal to allow factorable state generation in the required wavelength range. Ideally, this would be to produce

downconverted photons at less than 900 nm or so, where the efficiency curve for silicon detectors is still relatively high, and also allow pumping with a widely available type of broadband pulsed laser, an obvious choice for this downconversion range being the second harmonic of titanium:sapphire at around 400 nm. This goal can be achieved through the asymmetric group velocity matching regime in potassium dihydrogen phosphate (KDP).

At a phasematching angle of  $67.8^\circ$  in KDP, an e-ray pulse at 415 nm will travel with the same group velocity as an o-ray pulse at 830 nm, hence fulfilling the condition for asymmetric group velocity matching in Section 3.4. This results in a vertical phasematching function that is broadband in o-ray frequency but narrow-band in the e-ray. The collinear, plane-wave phasematching function is plotted in its approximate form for a 5mm long crystal in Figure 3.5, along with the pump envelope function for a broadband frequency-doubled titanium:sapphire laser centered at 415 nm, and the resulting two-photon joint intensity distribution. This is clearly highly factorable; the Schmidt number for this approximate distribution is  $K = 1.01$ . Therefore, over 99% of the emission is into the first Schmidt mode.

There is an intuitive physical explanation for how this single-mode emission takes place. As any o-ray downconversion would travel alongside the e-ray pump at their mutual group velocity of  $1.97 \times 10^8$  m/s, its possible emission time is therefore constrained to be contiguous with the highly temporally localized pump pulse. Hence o-ray daughter photons must be emitted into a mode that is similar to the broadband single temporal mode of the pump, and, as the modal structure of the o-ray photon

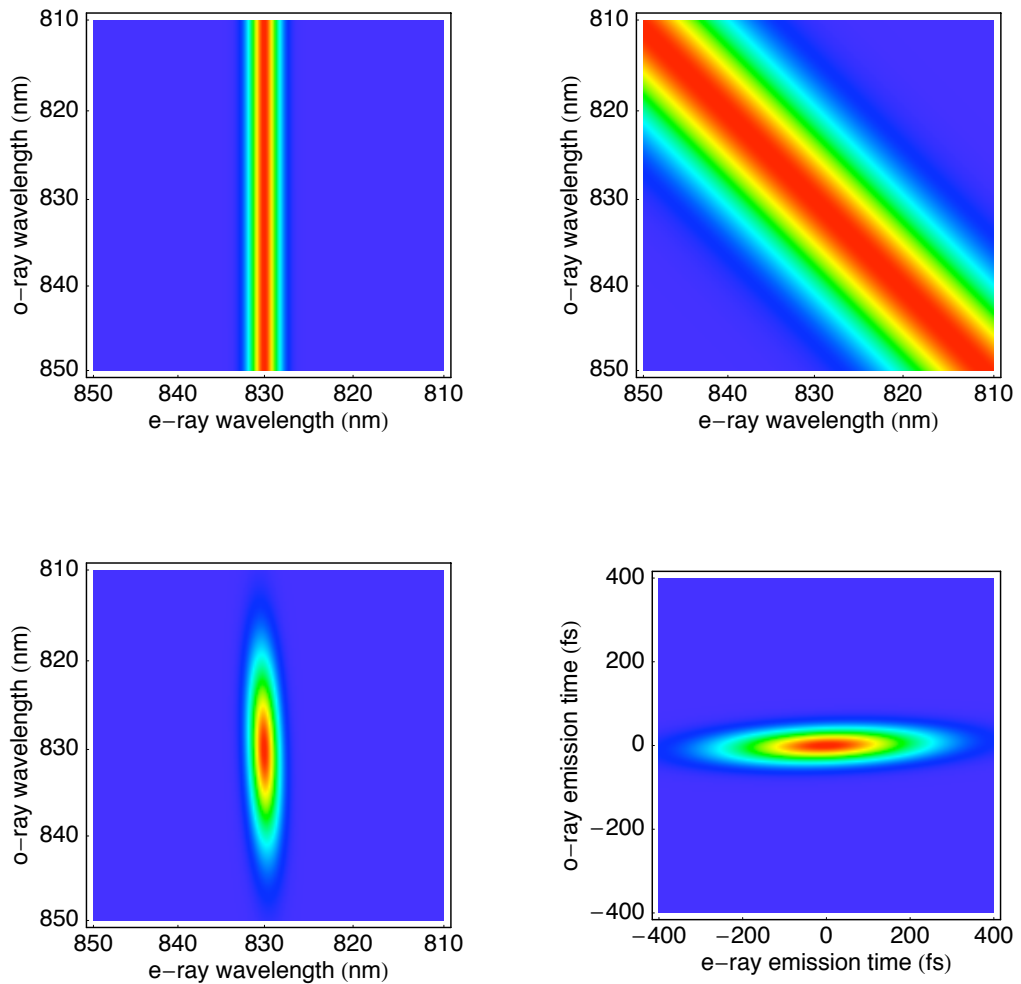


**Figure 3.5** Factorable state generation in KDP. Approximate phasematching intensity for 5 mm collinear type-II KDP centered at 830 nm (top left) and 4 nm bandwidth pump function at 415 nm (top right). Lower panels show the resulting factorable spectral (left) and temporal (right) intensity distributions.

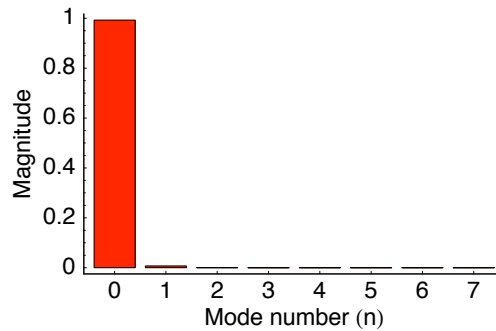


**Figure 3.6** Magnitudes of the first eight Schmidt coefficients for the approximate state generated by collinear type II KDP pumped at 415 nm (state as in figure 3.5).

is restricted to a single mode, so is that of the e-ray daughter photon. However, the e-ray downconverted photons travel at a group velocity of  $2.02 \times 10^8$  m/s. An e-ray photon created at the entrance face of the long crystal would have walked off ahead of the pump, whereas one created at the exit face would not, so the temporal mode structure of the e-ray photon is much less localized. Therefore emission is into a single broadband mode for the o-ray photon and a narrower bandwidth single mode for the e-ray photon. The single temporal mode structure of the photon pairs results in exceptionally low jitter in the arrival time of the single photons.

### 3.4.2 Additional methods of group velocity matching

The technique of selecting the pump wavelength and bulk birefringent nonlinear medium to give the correct dispersion properties to match either symmetrically or asymmetrically the group velocities of the three fields is the simplest way to achieve factorable state generation. For the purposes of the work presented here, there exists

an ideal, widely-available nonlinear crystal, KDP, and pump laser system, frequency-doubled titanium:sapphire, to implement this procedure in the laboratory. However, there are a limited number of combinations of crystals and wavelengths wherein this protocol is possible, and these may not provide the required output in all situations. This leads to the consideration of whether there exist any other regimes in which group velocity matching can be satisfied.

One possibility is to use something other than a bulk crystal for the nonlinear medium<sup>143</sup>. A series of identical nonlinear crystals that are not group velocity matched can be separated by linear but birefringent crystal spacers designed to compensate for the temporal walkoff in the nonlinear regions to form a so-called “crystal superlattice”<sup>144</sup>. By reversing the sign of the walkoff in the linear media, the relative positions fields that have walked off in the nonlinear sections are reversed during their traversal of the linear sections. In this way, in theory effective group velocity matching can be performed and factorable states prepared. However, one requires stringent tolerances on the thicknesses of the linear and nonlinear sections, something that is not possible with current manufacturing techniques.

Another potential method of obtaining factorable states is to utilise the transverse momentum of the pump and downconverted beams to provide an additional constraint on the phasematching landscape<sup>145</sup>. Repeating the derivation in Section 2.1 for type-I PDC with a pulsed pump that rather than being plane-wave is focused to a Gaussian spot, the resulting two-photon state has an additional multiplicative term that is a phasematching condition on the transverse wavevec-

tors<sup>101</sup>. For type-I PDC, this transverse phasematching function is dependent on the *difference* between the daughter frequency detunings, unlike the longitudinal phasematching function which is dependent on their *sum*. Therefore the transverse function is positively correlated in the daughter frequencies, and (analogous to the case of the positively-correlated longitudinal phasematching function in the case of BBO pumped at 800  $\mu\text{m}$ ) when multiplied by the negatively correlated longitudinal phasematching function (analogous to the pump in the case of BBO) can produce an uncorrelated state. This requires that a condition on the pump spot size relative to the crystal length is satisfied and that the angle between the downconverted beams that are collected is well-defined, for example by fibres. Additionally, it is essential that the pump function has enough bandwidth to not affect the joint amplitude. However, as this technique does not rely on group velocity matching through the material properties of the crystal it can be applied at any wavelength and is less dependent on finding exactly the right nonlinear crystal.

## Chapter 4

# Experimental Demonstration of Factorable State Generation

The model of downconversion as a plane-wave, collinear process combined with the approximation of the phasematching function as a Gaussian is sufficient to find the broad conditions required for factorable state generation. This model was used in Chapter 3 to derive the technique of group velocity matching and it was demonstrated that, within this framework, factorable state generation should be possible in two different regimes: symmetric and asymmetric.

In this chapter, the conditions surrounding asymmetric group velocity matching in KDP will be investigated in more detail. In preparation for this, the Gaussian approximation for the phasematching function must be abandoned and the full expression for the wavevector mismatch used in preference to the truncated Taylor expansion. These two changes respectively allow not only the side lobes on the

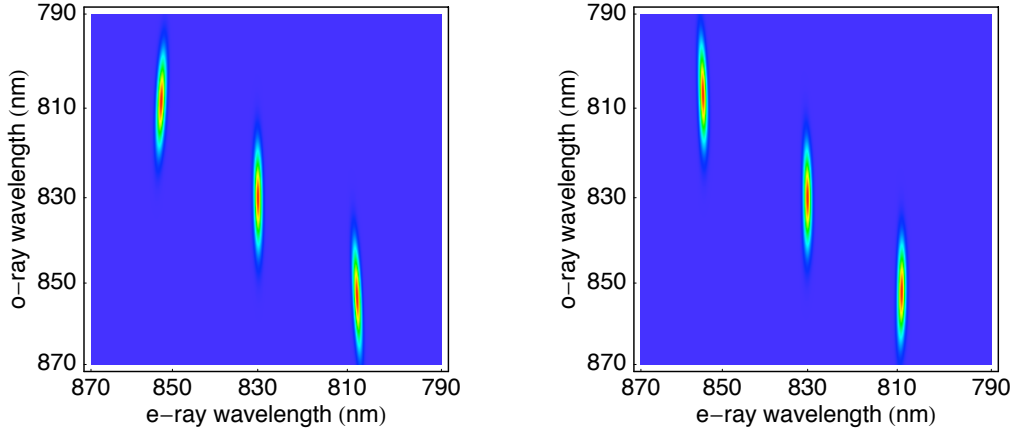


**Figure 4.1** Comparison of joint spectra generated using the exponential phasematching approximation with truncated wavevector mismatch (left) with those calculated from the full mismatch (right). Three individual joint spectra were calculated for three different phasematching angles separated by  $1.5^\circ$  and plotted on the same axes for ease of comparison. Each individual joint spectrum is for the collinear case. Note the exaggerated tilt on the nondegenerate joint spectra in the case of truncated mismatch.

phasematching sinc function but also its curvature due to higher order phase mismatch terms to be seen — changes that can make an appreciable difference to the factorability of the overall two-photon state. In fact, as the Taylor expansion was taken about the degenerate downconversion frequency  $\omega_0$ , the validity of the truncation is limited to a very small frequency range around the degenerate point. If using the truncation away from this point the removal of the proper curvature from the phasematching function can give predictions of a joint spectrum tilted in the opposite direction from the correct spectrum calculated with the full expression for  $\Delta k$ . This is demonstrated in Figure 4.1.

The exact phasematching function and two-photon state for collinear type-II

KDP pumped at 415 nm is shown in Figure 4.2. The slight curvature of the phase-matching function can now be seen, however, in a realistic experimental situation, this strict collinear calculation is still not enough to correctly model the two-photon states generated.

As described in Chapter 1, the degenerate emission from a type-II downconverter is into a pair of cones which, for collinear phasematching, intersect along the direction of the pump wavevector. In interference experiments, this complicated emission pattern requires that the spatial modes over which the e-ray and o-ray downconversion are collected are defined either using apertures or by coupling the light into single-mode optical fibres. Practically, it is more convenient to have the downconverted light coupled into single-mode fibre as this makes the experiment less susceptible to misalignment and delivers photons that can be easily distributed to subsequent pieces of apparatus. The action of the optics that couple light into the fibre is to map a single transverse Gaussian optical mode from the crystal onto the mode supported by the fibre. Hence the fibre acts as a spatial filter and to get good coupling efficiency into the fibre, preferential emission from the downconverter into the correct spatial mode must be encouraged. This is done by focusing the pump into the nonlinear crystal, rendering the collinear model inappropriate for simulating the states that will be generated. Furthermore, inhomogeneities in the pump beam can also introduce correlations that cannot be modelled with the techniques presented thus far.

In order to explain clearly the effect that each of these factors has on the joint

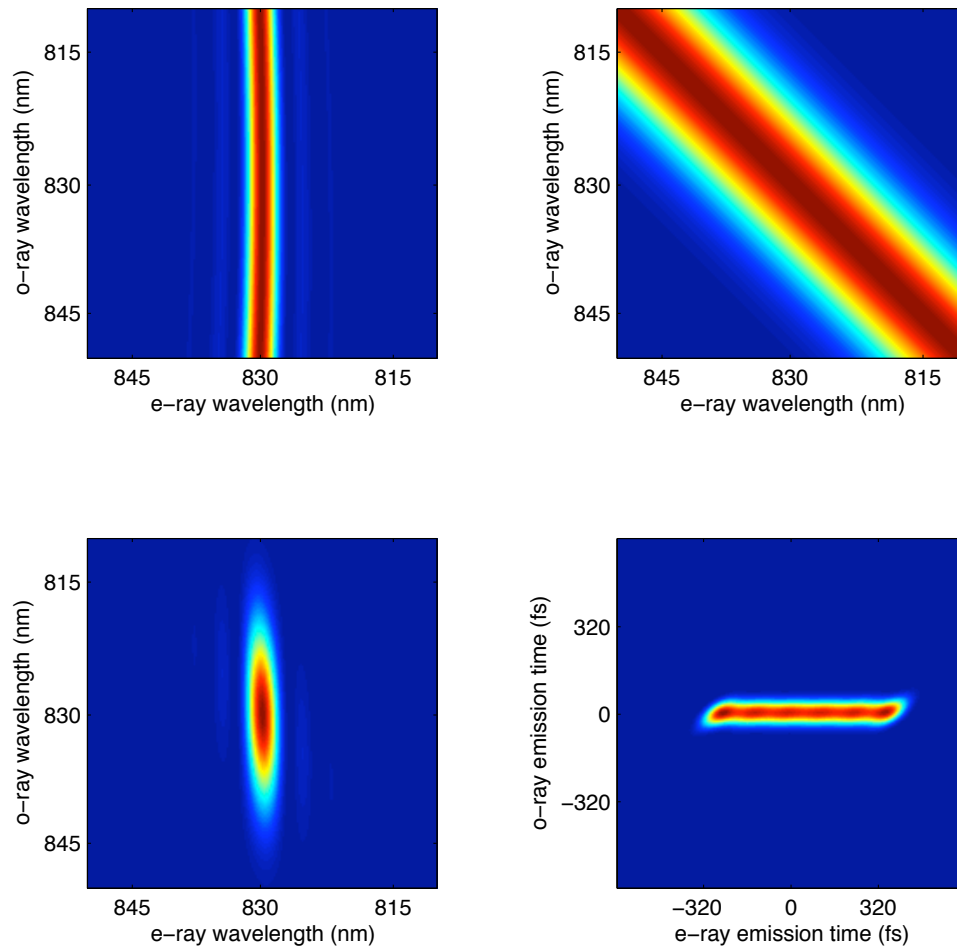


**Figure 4.2** Exact state for collinear type-II KDP. Intensity of the sinc phasematching function with full wavevector mismatch for a 5 mm crystal (top left), 4 nm pump function (top right), joint spectral intensity (bottom left), and joint temporal intensity (bottom right).

spectrum, the three key factors that must be understood and controlled to obtain a factorable state from asymmetrically group velocity matched KDP will be introduced one by one in this chapter. These three effects are firstly the pump focusing, then the fibre collection angle, and lastly the frequency inhomogeneities of the pump — here in the form of spatial chirp. Individual illustrations of their effect on the joint spectrum will be shown explicitly, followed by an explanation of how one may be traded off against another. A numerical model is developed that allows the experimentalist to model accurately the effects of changes in the focusing geometry or the pump and crystal characteristics upon the factorability of the final state. Then a method for characterizing experimentally the joint spectral intensity is demonstrated along with results of measurements made on the joint spectrum from KDP. These experimental results are shown to be in good agreement with the predictions of the numerical model.

The detailed numerical study of factorable state generation in a plausible experimental situation presented in this chapter was an essential precursor to achieving a successful laboratory demonstration of pure single photon preparation. It represents a significant advance on previous work on factorable states from downconversion sources as it allows a full understanding of how focusing and pump effects can introduce correlations to a state that would otherwise be factorable. Furthermore, it can be applied to other nonlinear crystals to study the states generated therein.

Finally in this chapter, a measurement of the degree of second order coherence of the source is described. This confirms the nonclassical nature of the emission from

the downconverter and that the heralded states can, to a very good approximation, truly be considered to be single photons.

## 4.1 Experimental factors affecting factorability

### 4.1.1 Pump focusing

The focusing of pump pulses into a nonlinear crystal is perhaps the most obvious way in which the majority of experimental situations differ from the plane-wave model of downconversion derived in Section 2.1. Even though, as in the situation at hand, the focusing need not be tight, it can still have a significant effect on the joint spectrum. There are several schools of thought on exactly how one should focus into a downconversion crystal depending on the configuration and the criteria that require optimization. None of these result in a strict set of rules that can be applied to any given experiment but the general consensus is twofold. Firstly, tighter focusing broadens the spatial distribution of the pairs<sup>146</sup> and reduces the level of spatial entanglement between the daughter photons. Secondly, to increase the coupling efficiencies of the pairs into single mode fibre, one must focus to a smaller spot in the crystal<sup>92,147</sup>.

However, consideration should also be given to the effects of spatial walkoff in the nonlinear crystal. As the pump is e-polarised, the birefringence of the crystal means that the Poynting vector of the pump will not be collinear with its wavevector and as the beam traverses the crystal it will skew off in the plane of the optic axis.

This has the seemingly counter-intuitive effect of smearing out the spatial emission pattern of the o-ray rather than the e-ray daughter photons. The e-ray photons travel in the same direction as the pump whereas o-ray photons do not walk off and hence travel in the direction of their wavevector. So, as the e-ray pump walks off to the side, o-ray daughter photons can be emitted in the forward direction from all points along the line of the pump beam, spreading out their emission spatially as illustrated in Figure 4.3. To be able to image into a fibre the volume in the crystal whence emission occurs, it is desirable that the pump walkoff should not be larger than the pump spot size.

An optimal solution for balancing these two opposing forces is not simple to find. Here we adopt an approach often employed to maximise the efficiency of nonlinear optical processes by setting the Fresnel number of the pumping system to be as close to unity as possible given the constraint of spatial walkoff. Approaching a Fresnel number of one by matching the Rayleigh range of the pump focus to the length of the crystal encourages preferential emission into a single spatial mode, allowing efficient fibre coupling of the downconverted pairs<sup>148</sup>. The pump Fresnel number is defined as

$$\mathcal{F}_{\text{pump}} = \frac{z_R}{L} = \frac{\pi w_0^2}{\lambda_p L} \quad (4.1)$$

where  $w_0$  is the radius of the pump beam waist. Therefore  $z_R$ , the Rayleigh range of the pump focus, must be of the order of the crystal length. The crystal must be at least several millimeters long to ensure that Equation 3.46 is valid, and so we see that for a crystal of  $L = 5$  mm the  $\mathcal{F}_{\text{pump}} = 1$  condition gives a relatively

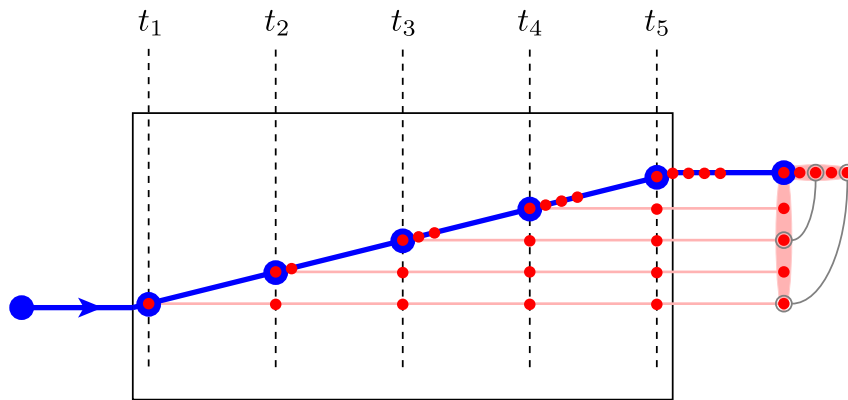


**Figure 4.3** Illustration of spatial and temporal walkoff during collinear downconversion in KDP. The blue pump pulse enters the crystal from the left and walks off spatially from the direction of its wavevector. For each of the five time bins ( $t_1 - t_5$ ) considered there exists a probability amplitude for a possible downconversion event (represented by blue blobs), all of which have the potential to create a pair of daughter photons (red blobs). An e-ray photon created would travel in the same direction as the pump but at a higher group velocity, whereas an o-ray would travel in the direction of the pump wavevector but at the same group velocity as the pump. At the exit face of the crystal, these amplitudes sum coherently so that the resulting e-ray distribution is long in time and narrow in space, opposite to the o-ray distribution which is short in time but spread out in space.

large beam waist radius of  $w_0 = 25 \mu\text{m}$ . For a pump beam of around a millimeter in diameter, a fairly long focal length lens ( $f \approx 200 \text{mm}$ ) will provide the required focusing conditions.

An additional constraint in the system under investigation here is to maintain the level of factorability in the joint spectrum given the focusing conditions required for efficient coupling. The principal effect of a light focus upon the joint spectrum is that, within the pump beam that was previously considered to be collimated, there now exists an angular distribution of wavevectors. This angular spread can be estimated simply through the geometry of the pumping system: the FWHM distribution of propagation angles in the crystal will, in the paraxial limit, be equal to the ratio of the FWHM beam diameter of the collimated pump beam incident on the focusing lens to the distance from the lens to the crystal (i.e. the focal length of the lens):

$$\Delta\theta \approx \frac{2w_{\text{lens}}}{f}. \quad (4.2)$$

This is shown in Figure 4.4. Every angle within this pump distribution will experience different phasematching conditions due to its unique propagation direction relative to the optic axis of the crystal. Hence over the corresponding range of angles exiting the crystal there will be a spread of downconversion wavelengths, each associated with the particular pump angle that gave rise to the pair, and each with a different central wavelength. As this distribution will eventually be coupled into single-mode fibre and hence summed to give the total two-photon amplitude, the relationship of these new wavelengths to one another becomes very important. Any

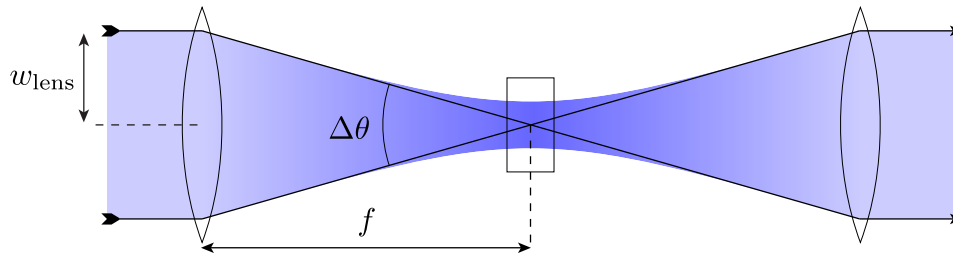


**Figure 4.4** The angular range of wavevectors contained in the focus of a Gaussian beam that was initially collimated can be approximated by the ratio of the beam size at the lens to its focal length.

trends here could lead to unwanted spectral correlations in the joint state.

This coupling of downconversion wavelength to angle is shown in Figure 4.5. This is a plot of the collinear, degenerate phasematched wavelength in KDP as a function of the phasematching angle, expressed as the difference between this angle and  $67.8^\circ$ , the collinear phasematching angle at 830 nm. It can be seen that this central downconversion wavelength changes rapidly as a function of angle, and that, when considered over a broad wavelength range, this variation is not linear. However, in the second panes of the figure the central wavelength range around 830 nm is plotted, and in this region the phasematched wavelength is approximately proportional to the angle. The gradient of this section demonstrates the sensitivity of wavelength to angle — a change in angle of only  $1^\circ$  will move the central collinear wavelength by over 10 nm.

The effect that this has on the joint spectrum is more pronounced for the e-ray than the o-ray due to the orientation of the phasematching function. A change in the central downconversion wavelength appears primarily as a translation of the

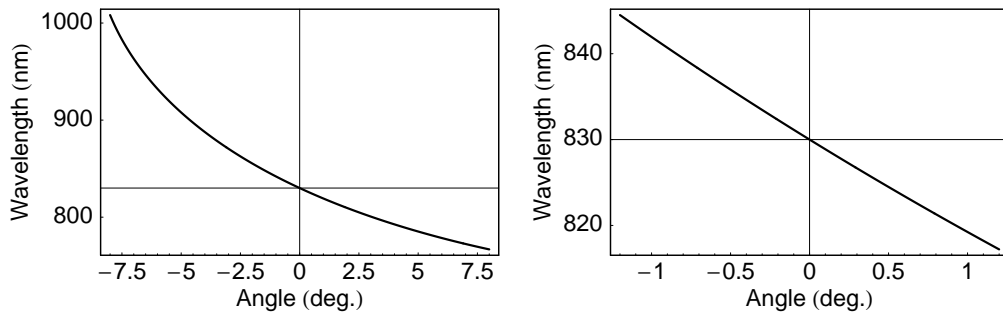


**Figure 4.5** Change in degenerate collinear phase-matching wavelength against collinear phase-matching angle in KDP. The phase-matching angle is expressed as the difference from the perfect collinear phase-matching angle at 830 nm. The right panel shows the approximately linear variation in wavelength over a small range of angles close to the zero.

centre of the phase-matching function. This shifts the e-ray wavelength but leaves the o-ray to be affected only through the energy conservation of the pump envelope function. The secondary effect is to introduce tilt to the degenerate section of the phase-matching function as the group velocity matching condition between pump and o-ray is no longer fulfilled at the new wavelengths.

However, simply changing the collinear phase-matching angle is not sufficient to represent pump focusing as it assumes that the angle at which the output is collected also changes. In a situation where the output is collected at a certain fixed angle, as happens in the scenario of focused PDC, we have to consider noncollinear phase-matching. The outcome is similar to the collinear case, as changing the pump propagation angle while leaving the output angle fixed also translates the centre of the phase-matching function. A schematic diagram of pump focusing with a fixed output angle is shown in Figure 4.6, while Figure 4.7 illustrates the associated change

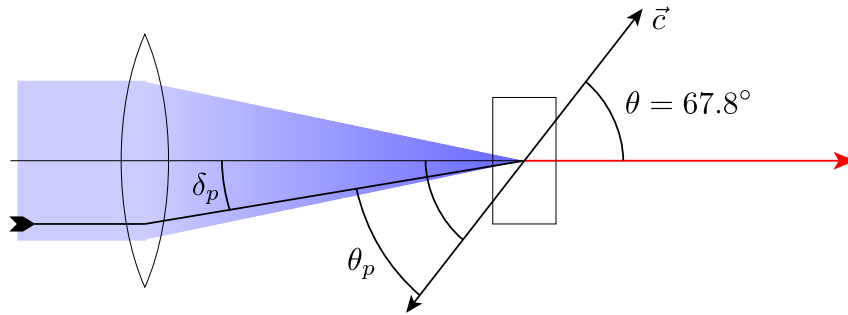


**Figure 4.6** Schematic of pump focusing with a fixed downconversion collection angle.

in the noncollinear phasematching function as the angle of the pump is varied. Nine noncollinear phasematching functions are plotted for nine pump propagation angles, with the output angle constant at the angle of perfect collinear phasematching at 830 nm,  $\theta = 67.8^\circ$ .

As the e-ray wavelength changes with pump angle, the e-ray distribution is broadened as, even for weak focusing, the shift in wavelength will be of the same order as the collinear e-ray bandwidth. In itself, this would not introduce any additional correlations to the state, but, as mentioned in the previous paragraph, the o-ray wavelength is coupled to that of the e-ray by the energy conservation condition. Therefore, as the e-ray wavelength gets shorter, so the o-ray must get longer and vice versa. Clearly, through this relationship, focusing has the potential to bring correlations to a state that for collinear pumping would have none. Thus tilt could be introduced to the overall joint spectrum through focusing, reducing the factorability of the two-photon state.

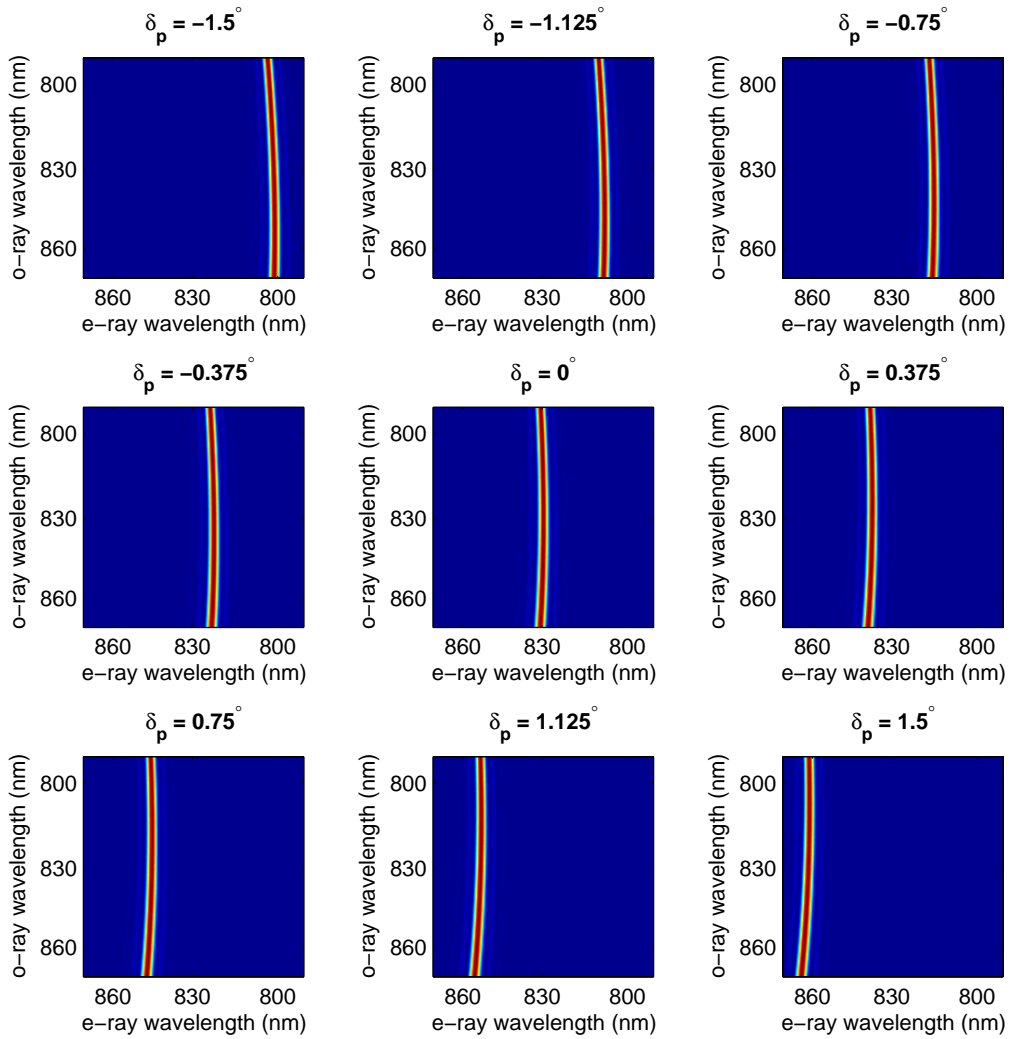


**Figure 4.7** Illustration of how changing the pump angle of non-collinear KDP affects the phasematching function. Angles are in steps of  $0.375^\circ$ , running from the largest angle between the pump and the optic axis at the top left to the smallest at the bottom right and centered on collinear phasematching at 830 nm.

### 4.1.2 Fibre coupling collection angle

Another related focusing effect arises from the collection of the downconversion into single-mode fibres. For a downconversion system pumped with a collinear beam, the output is still distributed in the “two cones” pattern explained in Section 1.6. Each photon pair with given e- and o-ray frequencies is emitted along a specific pair of cones with opening angles that are defined by the pair of frequencies. Therefore the frequency of the light within the distribution has an angular dependence due to the dependence of the e-ray refractive index on the angle of propagation. Figure 4.8 is a schematic of downconversion collection over a range of angles for a collimated pump, the effect of which upon the noncollinear phasematching function is demonstrated in Figure 4.9. This figure shows plots of the phasematching function for KDP with a collimated pump incident at  $\theta = 67.8^\circ$  but varying the angle of emission of the e-ray (and by association the o-ray also). As this emission angle is varied, the phasematching function again shifts sideways, but note now that this change is not monotonic. As the e-ray angle is scanned in one direction, the phasematching function initially moves one way but then, close to the collinear point, this movement reverses and the function turns back on itself. This is a result of the group velocity matching condition for collinear phasematching being at a turning point in  $\Delta k(\omega_e, \omega_o)$  relative to  $\omega_o$ .

This dependence of the phasematched wavelength on the e-ray emission angle means that, even for a downconversion system pumped with a collimated beam, the frequency of the pairs are dependent on the angle of emission. Therefore, the

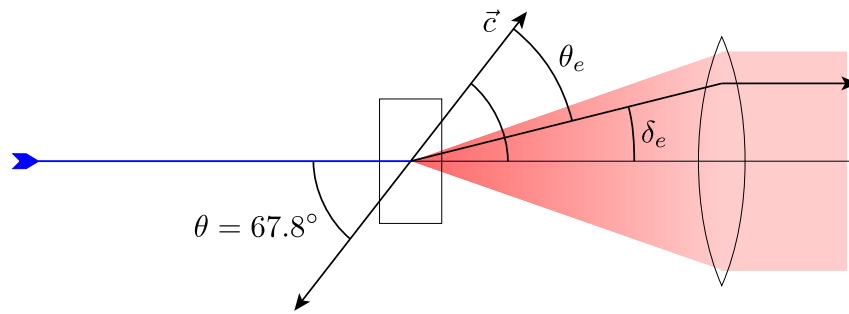


**Figure 4.8** Schematic of downconversion collection over a range of angles with a collimated pump.

joint spectrum of the overall state is related to the angle over which the pairs are collected. The situation is similar for a system with a focused pump, however the effects of pump focusing and collection angle are now compounded as for each angle in the pump distribution the corresponding distribution of frequencies over e-ray emission angle will change.

One function of the collection apparatus is to select a certain angular range of output from the downconverter and discard everything else. For collection into a single-mode fibre, the effect is to project the output state onto a Gaussian transmission function that is dependent on the emission angle. This angular distribution can be estimated in the same way as that of the pump — the angular distribution coupled into the fibre is the ratio of the diameter of the beam coupled into the fibre over the distance from the crystal to the coupling lens. Similarly to the pump focusing condition, it is desirable to have the Fresnel number of the collection optics equal to one for good coupling, corresponding to a one-to-one mapping of the pumped volume in the crystal onto the fibre collection mode.

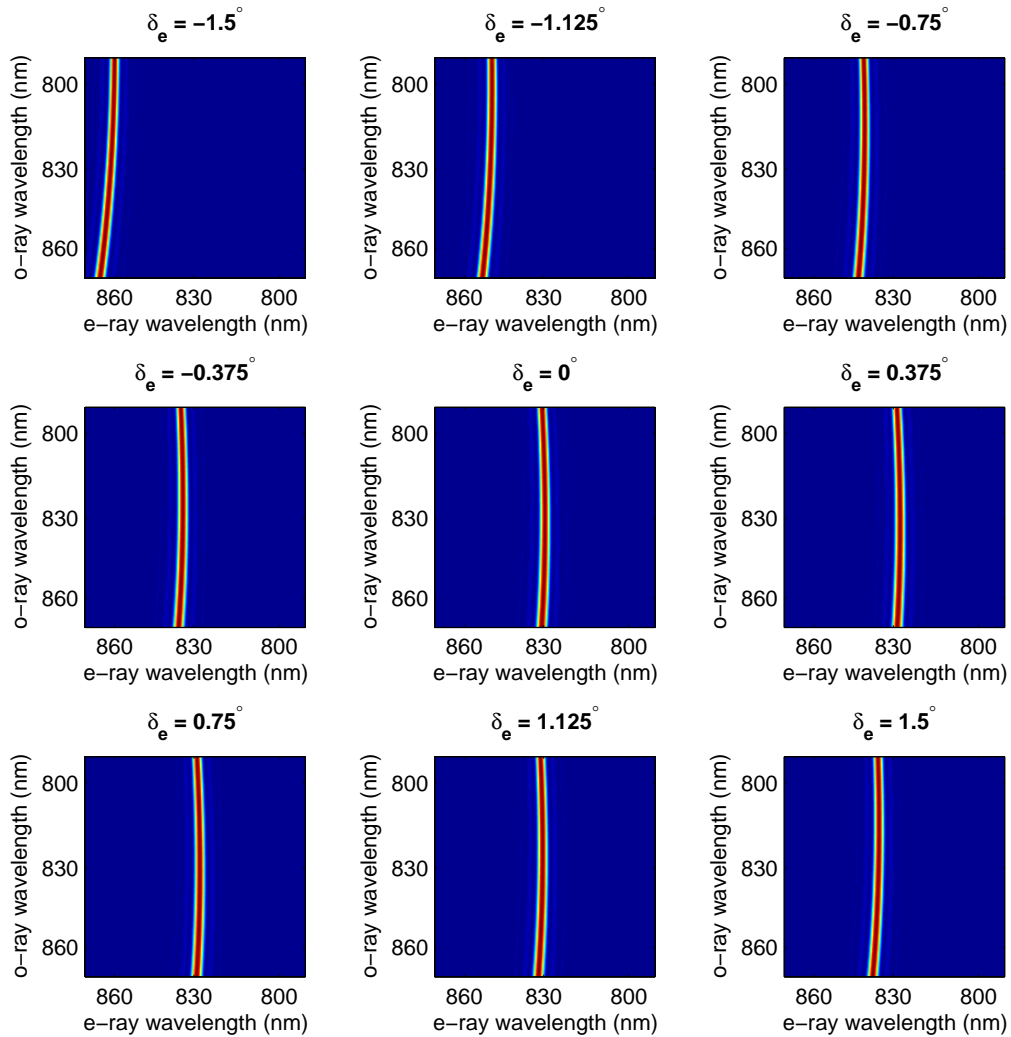


**Figure 4.9** Illustration of how changing the e-ray emission angle of noncollinear KDP affects the phasematching function. Angles are in steps of  $0.375^\circ$ , running from the largest angle between the e-ray emission and the optic axis at the top left to the smallest at the bottom right and centered on collinear phasematching at 830 nm.

### 4.1.3 Spatial chirp

The last factor that one has to consider arises from the method of generating the pump pulses at 415 nm. In order to obtain high efficiency in the second harmonic generation (SHG) of the titanium:sapphire laser, it is necessary to maximise the intensity of the pulses in the SHG crystal. To that end, the fundamental beam needs to be focused tightly into the nonlinear medium. Hence a range of phasematching angles is present in the SHG crystal also, though this distribution is much broader than that in the downconversion crystal. Similarly to the downconversion situation, the differing phasematching conditions across the beam correlates the frequency of the upconverted pulses with their angle of propagation. This angle is mapped onto transverse beam position by the collimating lens following the SHG crystal and the frequency-doubled pulses, destined to pump the downconversion, are therefore spatially chirped — their central wavelength changes with position across the beam.

In the experiments presented here, BBO angled for type-I phasematching at 830 nm is used for frequency doubling due to its high nonlinearity and consequent high conversion efficiency. As this crystal is uniaxial it is only the change in angle in the principal plane that makes a significant difference to the phasematching conditions; changes of angle perpendicular to this do not. It is for this reason that the output beam is spatially chirped in only one dimension. Compared to downconversion, the roles of e- and o-ray are reversed — here two photons from the o-ray pump combine to produce one e-ray output photon. Therefore the spatial chirp, which is in the plane of the optic axis, appears in the same plane as the output polarisation.

In the perpendicular direction the central frequency is independent of position.

When focused into the KDP crystal, position in this spatially chirped beam is once again mapped back onto angle. Therefore each of the different phasematching angles present in the pump distribution in the downconversion crystal will have a different central pump wavelength, hence the effective pump envelope function will be angularly dependent. Graphically, this corresponds to translating the pump function along the line  $\omega_e = \omega_o$ . Without any focusing, this would not significantly increase the level of correlation in the two-photon state as the chirped pump would just act like a more broadband unchirped pump. However, when combined with the changes in phasematching function as a result of focusing, this angular variation in the pump function can introduce much stronger correlations into the joint spectral distribution than simply the focusing alone. The effects of a spatially chirped pump beam are demonstrated in Figure 4.10 by plotting a series of five joint spectra corresponding to five collinear phasematching functions at different angles. These are similar to those shown in Figure 4.7, but here each phasematching function is multiplied by a pump function centered at a different wavelength to simulate a spatially chirped beam. It is clear that, in the case of positive correlation between pump frequency and phasematching angle, one could sum over the joint spectra in the range displayed and end up with a total joint spectral intensity uncorrelated in e- and o-ray frequency, whereas in the negatively correlated situation, summing over the joint spectra shown would give a highly correlated state. This situation becomes more complicated when the e-ray output angle is also varied.

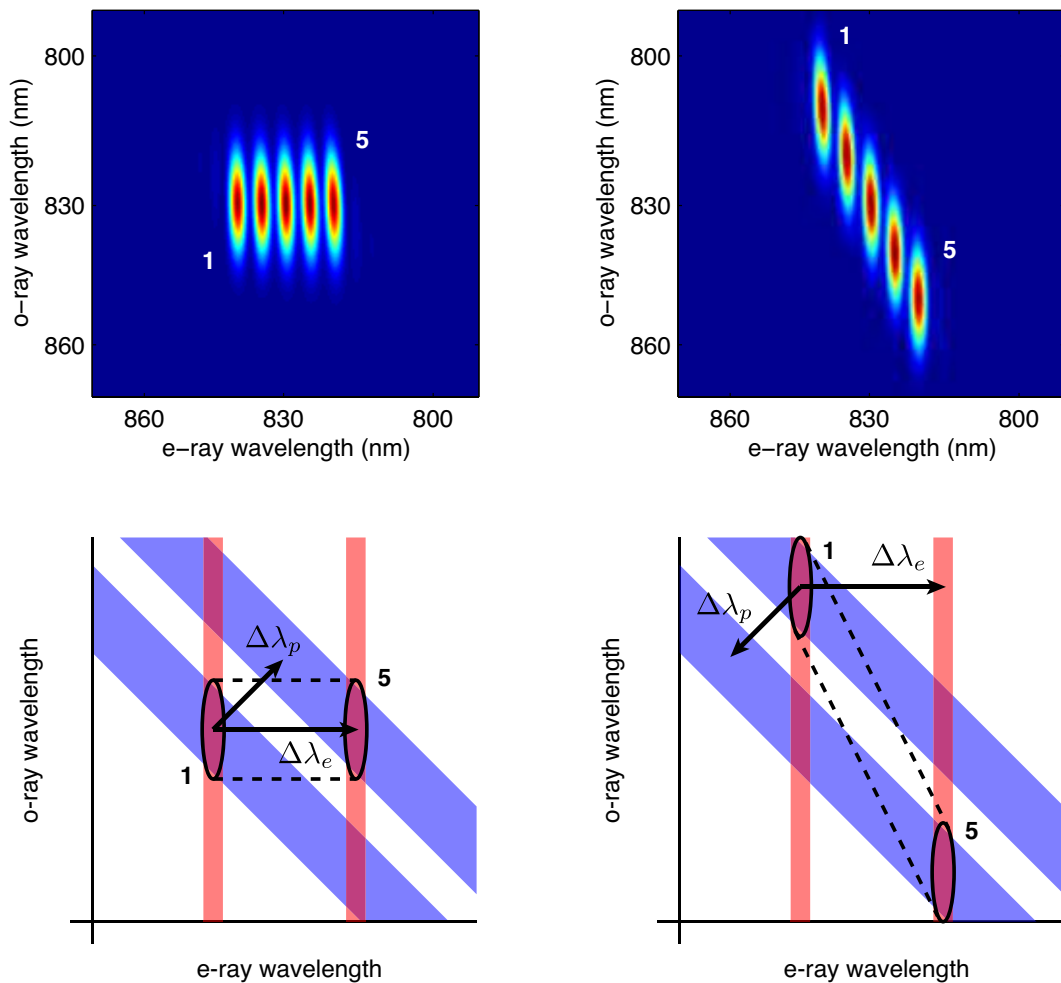


**Figure 4.10** An illustration of how pump spatial chirp can affect the joint spectrum in the case of a focused pump in KDP. Five discrete directions of propagation within a continuous pump distribution are considered; the left column shows positive correlation of pump frequency with phasematching angle, the right shows negative correlation. At the top, the five discrete joint spectra resulting from the multiplication of five collinear phasematching functions at different phasematching angles by five pump functions whose central wavelength depends on the angle of propagation in the crystal are shown labelled 1 to 5. Angles change in half degree steps, centered on collinear phasematching at 830 nm, while pump wavelengths are separated by 5 nm. The lower half is a schematic representation of the difference between the two cases above, with the phasematching functions in red and the pump functions in blue. Both phasematching functions move by  $\Delta\lambda_e$ ; both pump functions move by  $\Delta\lambda_p$  but in opposite directions for positive and negative spatial chirp. For positive chirp, the change in the phasematching function is compensated by the corresponding change in the pump wavelength, whereas for negative chirp the phasematching and pump movements compound one another. For a continuous pump distribution, one would sum over the range of the five joint spectra shown, hence resulting in a factorable distribution in the case of positive spatial chirp but a correlated state for negative spatial chirp.

## 4.2 Numerical modelling

The familiar phasematching conditions and two-photon state derived in Section 2.1 form the basis of a model that allows the selection of the correct parameters to give factorability taking into account the three issues outlined above. Due to the complexity of the phasematching landscape once all the required angles and wavelengths have been included, an analytic solution for the overall two-photon state is impossible. However, by considering the superposition of a set of numerically-calculated plane-wave solutions, a good approximation of the output state can be found, allowing the effects of changes in individual settings to be distinguished.

An accurate representation of downconversion including focusing must handle more than simply collinear phasematching, and therefore a three-dimensional model could be required, immediately complicating the situation enormously. However, for the experiment presented herein, this can be simplified to only include two dimensions. As the downconversion process takes place in a uniaxial crystal and all the angles considered are small, the angle of propagation out of the principal plane does not cause a significant change in the phasematching conditions. The important angle is the projection of the angle of propagation onto the principal plane as, to within a small error, this sets the e-ray refractive index. In addition, the beam from the second harmonic generation is spatially chirped in only one direction. If the polarisation of the SHG beam is not rotated before it reaches the downconversion crystal, this spatial chirp will also lie in the principal plane of the downconverter as the pump must be an e-ray and the spatial chirp is in the same plane as the pump's

polarisation. Therefore all the important angles and wavelength dependences lie in the principal plane of the KDP crystal and the problem reduces to only two dimensions.

The phasematching conditions must therefore be adapted to two dimensions to give relationships linking the input and output angles that can be phasematched at each wavelength. The pump and downconverted momenta are resolved into components in the  $x$ -,  $y$ -, and  $z$ -directions, with the  $z$ -axis lying along the direction of perfect collinear phasematching and making an angle of  $\theta_{pm}$  with the optic axis of the crystal. The optic axis, and hence the principal plane, is set in the  $xz$ -plane and all the  $y$ -components of the wavevectors can then be set to zero. This leaves the wavevector mismatches as:

$$\begin{aligned}\Delta k_x &= k_{e,x}(\omega_p, \delta_p) - k_{e,x}(\omega_e, \delta_e) - k_{o,x}(\omega_o) \\ \Delta k_z &= k_{e,z}(\omega_p, \delta_p) - k_{e,z}(\omega_e, \delta_e) - k_{o,z}(\omega_o).\end{aligned}\tag{4.3}$$

where the components of the pump wavevector are found from Figure 4.11 to be

$$\begin{aligned}k_{e,x}(\omega_p, \delta_p) &= k_e(\omega_p, \theta_p) \sin \delta_p, \\ k_{e,z}(\omega_p, \delta_p) &= k_e(\omega_p, \theta_p) \cos \delta_p,\end{aligned}\tag{4.4}$$

where  $k_\mu(\omega_\mu, \theta_\mu) = |\vec{k}_\mu(\omega_\mu, \theta_\mu)|$  and  $\theta_\mu$  is the angle subtended by each ray and the optic axis,  $\theta_\mu = \theta_{pm} - \delta_\mu$ . Similar expressions can be written down for the e- and o-ray components. As in Equation 2.17, perfect transverse phasematching is assumed

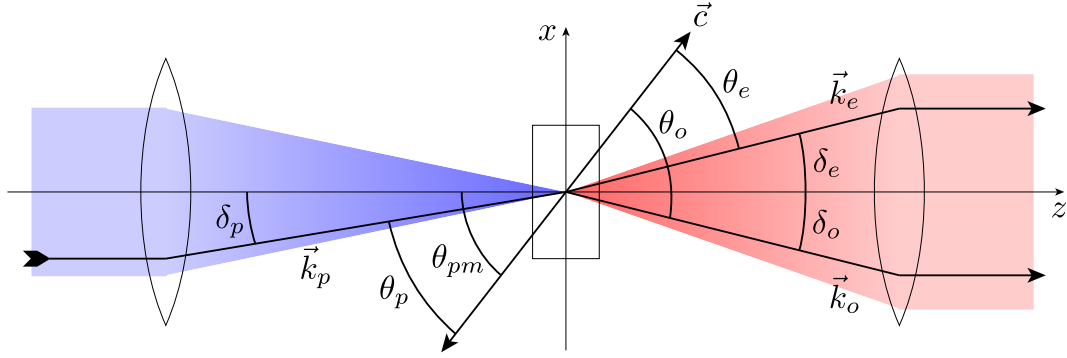


**Figure 4.11** Definition of angles in the numerical model.

in the  $x$ -direction so that

$$k_e(\omega_p, \theta_p) \sin \delta_p = k_e(\omega_e, \theta_e) \sin \delta_e - k_o(\omega_o) \sin \delta_o. \quad (4.5)$$

Note that, for a given value of  $\delta_p$ , Equation 4.5 cannot be solved analytically for  $\delta_e$  due to the dependence of the e-ray wavevector on angle. However, a simple solution does exist for  $\delta_o$ :

$$\delta_o = \arcsin \frac{k_{e,x}(\omega_p, \delta_p) - k_{e,x}(\omega_e, \delta_e)}{k_o(\omega_o)} \quad (4.6)$$

where the pump and e-ray wavevectors have been written as their  $x$ -components for clarity, with the  $\theta_\mu$  dependences implicit in this. So for a given set of  $\{\omega_p, \delta_p, \delta_e\}$  the angle  $\delta_o$  that gives perfect transverse phasematching at every pair of e- and o-ray frequencies can be found.

The wavevector mismatch in the  $z$ -direction is subsequently given by Equations

4.3 and 4.6 as

$$\begin{aligned} \Delta k_z(\omega_e, \omega_o, \delta_p, \delta_e) &= k_e(\omega_e + \omega_o, \theta_p) \cos \delta_p - k_e(\omega_e, \theta_e) \cos \delta_e \\ &\quad - k_o(\omega_o) \cos \left[ \arcsin \left( \frac{k_{e,x}(\omega_e + \omega_o, \delta_p) - k_{e,x}(\omega_e, \delta_e)}{k_o(\omega_o)} \right) \right], \end{aligned} \quad (4.7)$$

where the  $x$ -components are as defined in Equation 4.4. Therefore, for set values of the pump angle and e-ray collection angle, from this relationship can be found the wavevector mismatch for each pair of frequencies of the daughter photons. For phasematching in the longitudinal direction, the relationship from Equation 2.17 is again used:

$$\phi(\omega_e, \omega_o, \delta_p, \delta_e) = e^{\frac{i\Delta k_z L}{2}} \text{sinc} \left( \frac{\Delta k_z L}{2} \right). \quad (4.8)$$

By substituting the mismatch from Equation 4.7 the plane-wave phasematching function and hence the joint spectrum can be plotted for any pair of angles  $\delta_p$  and  $\delta_e$ .

In order to calculate the joint spectrum of a realistic photon pair, however, a set of these plane wave solutions must be taken over the full range of pump and collection angles. Firstly, the focused pump is represented by a superposition of plane waves, summed over the angle  $\delta_p$ :

$$E_p^{(+)}(\vec{r}, t) = A_p \int_0^\infty d\omega_p \int_{-\frac{\pi}{2}}^{\frac{\pi}{2}} d\delta_p \alpha(\omega_p, \delta_p) \exp \left[ i \left( \vec{k}_e(\omega_p, \delta_p) \cdot \vec{r} - \omega_p t \right) \right]. \quad (4.9)$$

The Gaussian angular dependence of the pump is written implicitly in  $\alpha(\omega_p, \delta_p)$ , and

for linear spatial chirp the central pump frequency becomes a function of the same angle,  $\delta_p$ :

$$\begin{aligned}\alpha(\omega_p, \delta_p) &= \alpha(\omega_e + \omega_o, \delta_p) \\ &= \exp \left[ - \left( \frac{\omega_e + \omega_o - 2(\omega_0 + q\delta_p)}{\sigma} \right)^2 \right] \exp \left[ - \left( \frac{\delta_p}{\sigma_L} \right)^2 \right],\end{aligned}\quad (4.10)$$

where  $q$  is a constant, defined at  $\omega_0$ , describing the rapidity with which the central pump frequency changes across the angular distribution of the pump. The angular bandwidth of the pump, set by the strength of the lens before the downconversion crystal, is given by  $\sigma_L$  and the central wavevector of the pump distribution lies along the  $z$ -axis. Secondly, the collection of the downconversion into single-mode fibres is modelled by two Gaussian filter functions, one dependent on  $\delta_e$  and the other on  $\delta_o$ :

$$g_F(\delta_e) = \sqrt[4]{\frac{2}{\pi\sigma_F^2}} \exp \left[ - \left( \frac{\delta_e}{\sigma_F} \right)^2 \right], \quad g_F(\delta_o) = \sqrt[4]{\frac{2}{\pi\sigma_F^2}} \exp \left[ - \left( \frac{\delta_o}{\sigma_F} \right)^2 \right], \quad (4.11)$$

where it is assumed that the angular acceptance bandwidth  $\sigma_F$  is identical for both photons and the peak transmission is along the  $z$ -axis (at  $\delta_e = \delta_o = 0$ ).

Substituting these expressions into the derivation of the two-photon state in Section 2.1, the result then becomes

$$\begin{aligned}|\psi(\omega_e, \omega_o)\rangle &= \int_0^\infty d\omega_e \int_0^\infty d\omega_o \int_{-\frac{\pi}{2}}^{\frac{\pi}{2}} d\delta_p \int_{-\frac{\pi}{2}}^{\frac{\pi}{2}} d\delta_e \int_{-\frac{\pi}{2}}^{\frac{\pi}{2}} d\delta_o \alpha(\omega_e + \omega_o, \delta_p) \\ &\quad \phi(\omega_e, \omega_o, \delta_p, \delta_e) g_F(\delta_e) g_F(\delta_o) \hat{a}_e^\dagger(\omega_e, \delta_e) \hat{a}_o^\dagger(\omega_o, \delta_o) |0\rangle.\end{aligned}\quad (4.12)$$

For small angles of emission,  $\delta_o \approx -\delta_e$ ; this effectively assumes that if the e-ray photon passes the filter and is collected into the fibre, the o-ray photon is also. Making this approximation reduces by one the number of sums in the numerical calculation hence reducing the processing time required. Equation 4.12 reduces to

$$|\psi(\omega_e, \omega_o)\rangle = \int_0^\infty d\omega_e \int_0^\infty d\omega_o \int_{-\frac{\pi}{2}}^{\frac{\pi}{2}} d\delta_p \int_{-\frac{\pi}{2}}^{\frac{\pi}{2}} d\delta_e \alpha(\omega_e + \omega_o, \delta_p) \phi(\omega_e, \omega_o, \delta_p, \delta_e) g_F^2(\delta_e) \hat{a}_e^\dagger(\omega_e, \delta_e) \hat{a}_o^\dagger(\omega_o, -\delta_e) |0\rangle \quad (4.13)$$

and the joint spectral amplitude distribution is then given by

$$f(\omega_e, \omega_o) = \int_{-\frac{\pi}{2}}^{\frac{\pi}{2}} d\delta_p \int_{-\frac{\pi}{2}}^{\frac{\pi}{2}} d\delta_e \alpha(\omega_e + \omega_o, \delta_p) \phi(\omega_e, \omega_o, \delta_p, \delta_e) g_F^2(\delta_e). \quad (4.14)$$

Note that the Gaussian filter function  $g_F^2(\delta_e)$  is the angular distribution of the *pairs* that are collected into the fibre. This set of equations form the basis upon which the two-photon state generated by a focused pump and collected into single-mode fibre can be modelled numerically. The results of such a model are discussed in Section 4.2.2.

### 4.2.1 Measurements of angular distributions

To obtain meaningful results from this model, the range of angles over which one should sum for a given experimental configuration must be known, along with the amount of spatial chirp on the pump. In order to quantify these, three measurements were made: the pump beam diameter, the pump spectrum as a function of position

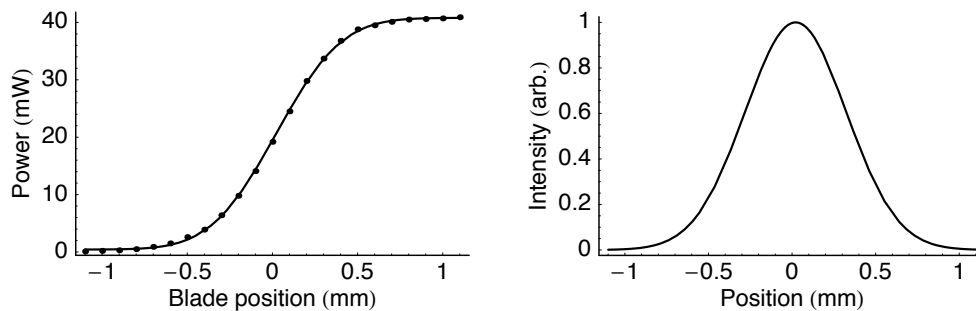


**Figure 4.12** Data for pump beam diameter and associated intensity distribution. From the fit statistics, the resulting error in the Gaussian width was determined to be approximately 1%.

in the beam, and the collected mode diameter. Through these parameters and knowledge of the focal lengths of the lenses used in a particular configuration, the values of  $\sigma_L$ ,  $q$ , and  $\sigma_F$  can be calculated and inserted into the model.

First the diameter of the pump intensity distribution was measured using a razor blade on a translation stage to cut the beam. The power after the blade was recorded as a function of the blade position as it was translated through the beam in the  $x$ -direction. The data, fitted with an error function, are displayed in Figure 4.12. This error function was differentiated to find the intensity distribution of the pump. The FWHM of this intensity distribution, measured to be 0.71 mm, and the focal length of the pump lens were used to obtain the FWHM of the angular intensity distribution and thence  $\sigma_L$  for the angular amplitude distribution.

Next, the spatial dependence of the central pump wavelength was characterized. By mounting an Ocean Optics USB2000 spectrometer (serial number USB2G3493) on a single-axis translation stage that could be orientated either horizontally or

vertically, the  $10\ \mu\text{m}$ -wide entrance slit of the spectrometer could be scanned across the beam, first in the  $x$ -direction and then in the  $y$ -direction. For each data set, the position of the spectrometer in the orthogonal direction was set to maximise the signal. The pump spectra were recorded at intervals of  $0.1\ \text{mm}$  in each direction, and the results for each direction are shown in Figure 4.13. As anticipated, the pump wavelength in the vertical ( $y$ ) direction is independent of position as the optic axis of the SHG crystal was orientated horizontally and therefore the e-ray refractive index is only weakly dependent on angle in the vertical direction. However, the effects of spatial chirp in the horizontal ( $x$ ) direction are significant; this is manifest in Figure 4.13 in the dramatic shift of the pump spectrum as the position of the entrance slit of the spectrometer was scanned horizontally across the beam. The amount of spatial chirp in the horizontal direction was quantified by fitting each of the measured spectra with a Gaussian function and then plotting the central wavelengths of these distributions as a function of position in the beam. The results of this process are also shown in Figure 4.13. The wavelength range of the spectrometer went only as low as  $650\ \text{nm}$ , hence the pump at  $415\ \text{nm}$  had to be viewed in the second diffracted order of its grating. Therefore, although the pump was at about  $415\ \text{nm}$ , these spectra were measured to be around  $830\ \text{nm}$ . It is for this reason that in Equation 4.10 the spatial chirp was defined at the central downconversion frequency rather than the central pump frequency. Therefore the value of the dependence of the pump frequency on angle in the horizontal plane,  $q$ , obtained directly from the second-order diffracted spectral data is the correct value for the model.

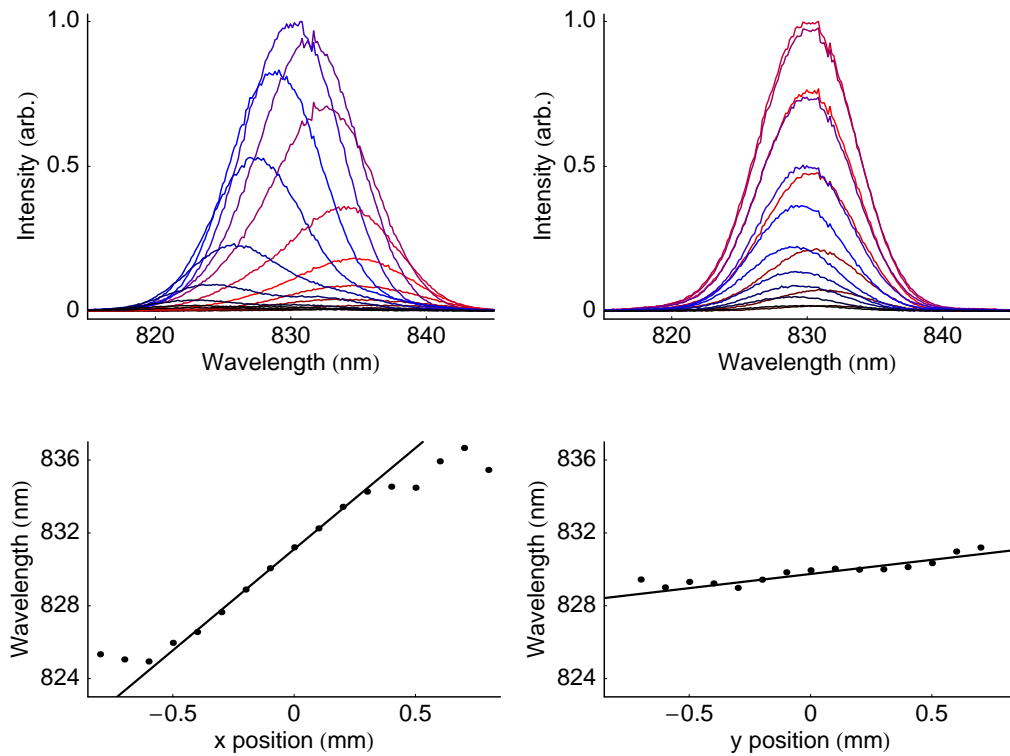


**Figure 4.13** Spatial chirp data. The top panels show the raw spectral data (viewed in the second order of the spectrometer) at different positions across the second harmonic beam scanning the spectrometer slit in 0.1 mm steps in the  $x$ -direction (left) and the  $y$ -direction (right). The central wavelengths of Gaussian fits to the data are displayed below each set of spectra along with linear best fit lines to the central seven data points. The gradients of the linear fits are 11.1 nm/mm and 1.56 nm/mm in the  $x$  and  $y$  directions respectively and the largest of the errors on the central wavelengths for the fits is similar in size to the points.

From the lower left plot in Figure 4.13 it can be seen that, close to the centre of the beam, the  $x$ -dependence of the central wavelength is approximately linear. This high-intensity central region contains most of the power in the pump beam, and hence it is the downconversion arising from this part of the pump that makes the predominant contribution to the final joint spectrum. Hence for the purposes of modelling the output, we can consider the spatial chirp to be linear and ignore any deviations from this in the low-intensity wings of the distribution. The gradient of a linear fit to the central seven points, found to be 11.1 nm per millimetre at 830 nm, was therefore taken as the dependence of the pump wavelength on position for insertion in the model. This result together with the measured FWHM diameter of the intensity distribution allowed the value of  $q$  to be found.

The observed behaviour of the central SHG wavelength can be explained by considering the intensity dependence of the conversion efficiency for the process of frequency doubling. The constraints imposed by phasematching alone would give, over a small range of angles such as we are dealing with here, a linear dependence of SHG wavelength upon angle (and therefore also position). This linear dependence of the degenerately-phasematched wavelength was shown in the case of KDP in Figure 4.5 but is also true for BBO, though with a different gradient. This trend is followed close to the centre of the spatial distribution as in this region the intensity is high and the output wavelength is controlled only by the phasematching conditions. However, moving away from this central section towards the wings of the intensity distribution, the conversion efficiency from fundamental to second harmonic drops

off with the falling intensity. The reduction in intensity is correlated with a shift in wavelength away from the wavelength that is phasematched at the centre of the spatial distribution (in this case, 415 nm). This corresponds to a correlation of conversion efficiency with wavelength within the spatial distribution: the most efficient upconversion takes place at the centre of the spatial distribution and hence at the centre of the wavelength distribution. Therefore, when selecting with the spectrometer slit a single output angle towards the edge of the beam, although the perfectly phasematched wavelength is linearly dependent on the spectrometer position, the measured spectral distribution is skewed towards the median wavelength (415 nm) due to the higher conversion efficiency there. This effect is manifest in two places in the data: firstly it can be seen that the individual spectra at the edges of the spatial (and spectral) distribution are markedly non-Gaussian as the tails closer to the centre of the entire distribution are larger than those on the outlying side, and secondly in the wings of the beam the centres of the fits to the spectra deviate away from linear behaviour towards the median wavelength.

The final requirement was the width of the mode coupled into the fibre. This was found with a similar technique to that employed in the measurement of the pump diameter. The fundamental beam from the laser system was coupled into a single-mode fibre and sent from the output of the fibre back through the PDC coupling system in the reverse direction. The blade was then positioned adjacent to a lens placed one focal length after the crystal to collimate the downconversion before its journey to the fibre coupling optics. A power meter was put in the reverse

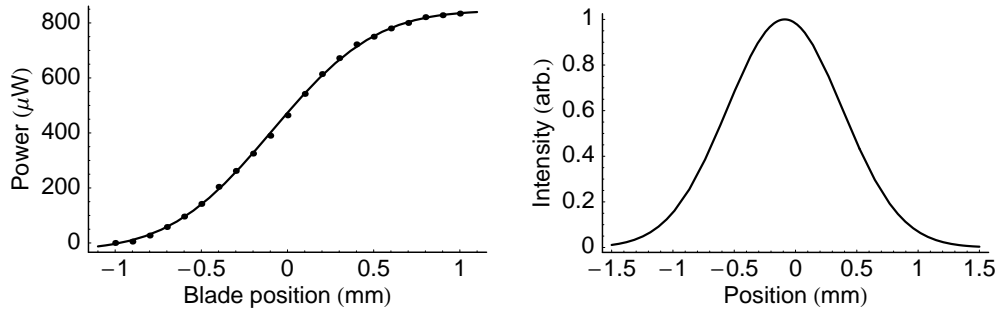


**Figure 4.14** Data for collected mode diameter and associated intensity distribution. From the fit statistics, the resulting error in the Gaussian width was determined to be approximately 2%.

beam after the blade and the power recorded as a function of the transverse blade position. Figure 4.14 shows the variation of the power against the blade insertion. This set of data was also fitted with an error function, the derivative of which gave the intensity distribution of the fibre-coupled mode for single counts. From this and the focal length of the collimating lens, the angular bandwidth for the amplitude distribution of the mode for pair collection,  $g_F^2(\delta_e)$ , was calculated.

#### 4.2.2 Results of the model

A numerical simulation based on the equations in this section was implemented in Matlab. The program was run to generate joint spectra over a range of values of parameters such as the pump angular distribution, collected mode angle, crystal length, and the central phasematching angle (the crystal angle,  $\theta_{pm}$ ). This allowed the effects of different experimental configurations upon the properties of the joint spectrum, in particular its factorability, to be observed. The factorability in each

configuration was quantified using the Schmidt number,  $K$ , found from the SVD of the final joint spectral amplitude summed over the relevant angles.

From an experimental viewpoint, some parameters are easier to control than others. For example, the magnitude of the spatial chirp on the pump beam is set by the type of crystal used for SHG, its length, and how tightly the pump is focused into it. However, the need for as much pump power as possible means that, once a good combination of lens and SHG crystal has been found for efficient upconversion of a particular laser, it is desirable that these remain fixed for the duration of the experiments in hand. Hence the spatial chirp on the pump beam is essentially predefined and difficult to change, although it could be removed entirely with an additional prism pair at the cost of some lost pump power. On the other hand, the direction of the spatial chirp can be switched simply by rotating the downconversion crystal by  $180^\circ$  about the central pump direction (the  $z$ -direction). As the spatial chirp has been defined in the principal plane of the crystal, this direction is either positive or negative; for the purposes of this discussion, positive spatial chirp is defined as pump wavelength increasing with  $\delta_p$ , or in other words, pump frequency dropping as the angle between the pump and the optic axis is reduced (see Figure 4.11). It then becomes clear that rotating the optic axis of the crystal about the  $z$ -direction by  $180^\circ$  effectively reverses the sign of the spatial chirp while maintaining the same overall phasematching conditions for the final summed two-photon state. This is achieved in the model simply by switching the sign of the spatial chirp that is input.

Other PDC source parameters that are relatively simple to change experimentally include the pump focusing, collection angle, crystal angle, and crystal length (so long as a range of crystals are available for use). This still suggests that a large number of parameters must be searched over to find the optimum configuration for factorable state generation. However, it can be narrowed down by a number of considerations, some as a result of the conditions required for factorability and others from experimental limitations.

The pump focusing conditions on one hand should be set to get as close to  $\mathcal{F}_{\text{pump}} = 1$  as possible to maximise generation in the single mode that gets coupled into the fibres, but on the other hand, due to the effect of spatial walkoff in the crystal, the spot size cannot be made too small. For a given crystal length and pump beam diameter, this criterion sets a limit on the minimum focal length of the pump lens and hence the maximum angular distribution of the pump. For KDP phasematched at 830 nm, the walkoff angle is just over  $1^\circ$ , so for a 5 mm long crystal the total walkoff is  $90 \mu\text{m}$  — larger than the optimum spot size for  $\mathcal{F}_{\text{pump}} = 1$ . These two considerations must therefore be balanced against one another. In addition, the angular range for a given pump beam diameter is restricted to a few discrete values as suitable lenses (see Section 5.3.1) are only available in a limited range of focal lengths.

There is a similar tradeoff for the collection angle. It should be set so that the fibre coupling apparatus maps the pumped volume of the crystal onto the mode volume of the fibre to maximise the coupling efficiency. This condition can most

successfully be found by testing experimentally various focusing configurations before the fibres to maximise the collected count rates. This is obviously dependent on the pump focusing conditions — for tighter pump focusing, a larger angular range must be collected into the fibres to obtain good count rates. However, as described earlier in this section, increasing the collection angle can introduce additional correlations to the joint spectrum. These two requirements must be satisfactorily balanced against one another, again taking into account the available optics.

The crystal length must be sufficiently large relative to the inverse pump bandwidth that Equation 3.45 is valid and factorable state generation is possible, but not so long that spatial walkoff becomes a problem. The crystal angle can be set to whatever value gives the best factorability, but as the angle is changed away from phasematching at 830 nm the central frequencies of the approximately collinearly phasematched signal and idler photons will move away from degeneracy. This in itself does not cause a problem as the range over which the silicon APDs are sensitive is sufficient for large changes in angle, however, some of the downstream optical elements (particularly the fibre-based 50:50 coupler used in subsequent experiments) are not broadband enough to cope with large deviations. Therefore the angle must be restricted to be close to  $\theta_{pm} = 67.8^\circ$ .

Figures 4.15 and 4.16 demonstrate some of the results of the model for positive and negative spatial chirps respectively. The joint spectra were all evaluated on a  $100 \times 100$  grid in frequency space over a range of 40 nm for both the e- and o-rays. These plots are for a 5 mm crystal and 7.5 nm of spatial chirp across the  $700 \mu\text{m}$

FWHM diameter of the pump intensity distribution. The intensity FWHM pair collection angle is  $0.15^\circ$ ,  $0.3^\circ$ , and  $0.45^\circ$  left to right while the FWHM angular intensity of the pump distribution is  $0.02^\circ$ ,  $0.08^\circ$ ,  $0.16^\circ$ , and  $0.27^\circ$  top to bottom, corresponding to focal lengths of 2000 mm, 500 mm, 250 mm, and 150 mm respectively for this pump beam diameter. The sums were performed over all combinations of 11 equally spaced angles in both the pump and collected distributions. It can be seen that the behaviour of the joint spectrum is very different for opposite spatial chirps. However, generally the distributions become broader and more correlated as the level of focusing is increased. As expected, spatial chirp does not affect the two-photon state generated by light focusing as all the frequencies in the pump beam experience approximately the same phasematching conditions.

By running the model repeatedly it was possible to generate plots of the expected purity to show the optimum values of various parameters for factorable state generation. Some of these are shown in Figures 4.17 and 4.18; note that in these calculations the joint spectra were evaluated on a  $50 \times 50$  grid to reduce the processing time. Although it would have been difficult to control some of these parameters experimentally (for example the magnitude of the spatial chirp), it is nonetheless interesting to be able to see their effects on the expected purity and to find the optimal values. In fact, a positive spatial chirp with the experimentally observed value (7.5 nm across the FWHM beam diameter) yields almost the highest purity for a pump beam centered at 415 nm.

The clearest result from this model is that, in order to prepare a state that

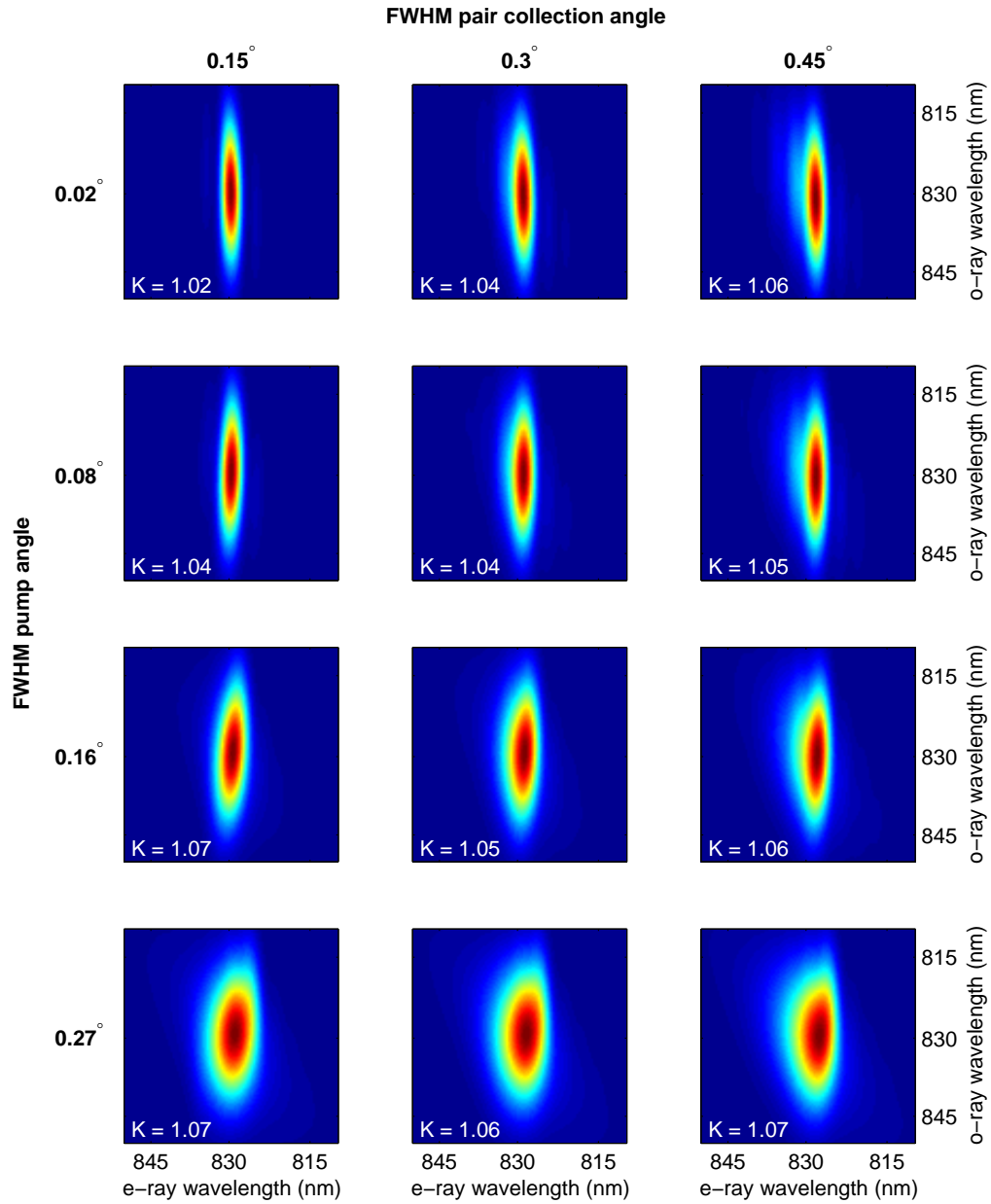


**Figure 4.15** Predicted joint spectral intensities for a range of pump and collection angles for positive spatial chirp. See text for details.

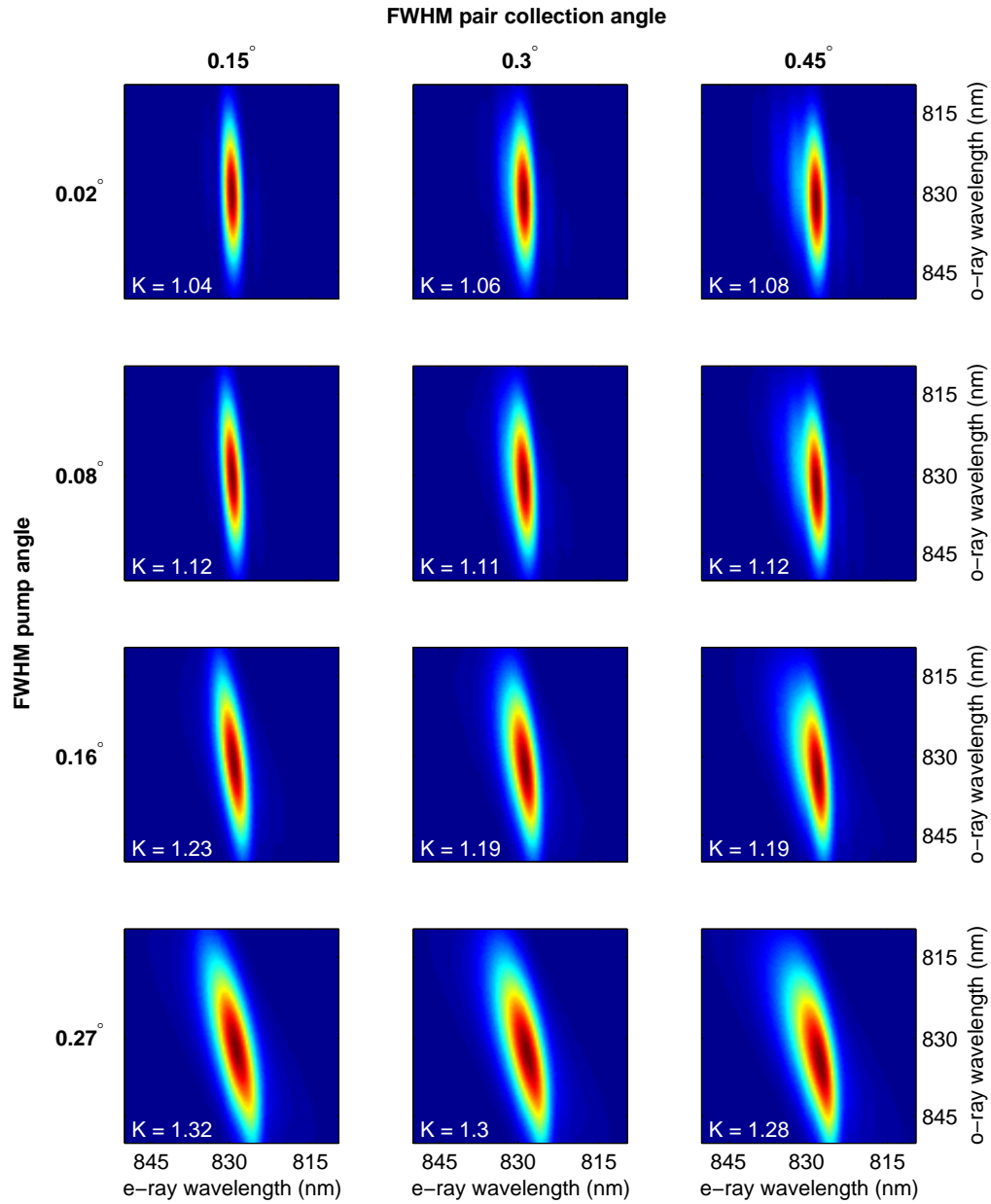


**Figure 4.16** Predicted joint intensities for a range of pump and collection angles for negative spatial chirp. See text for details.

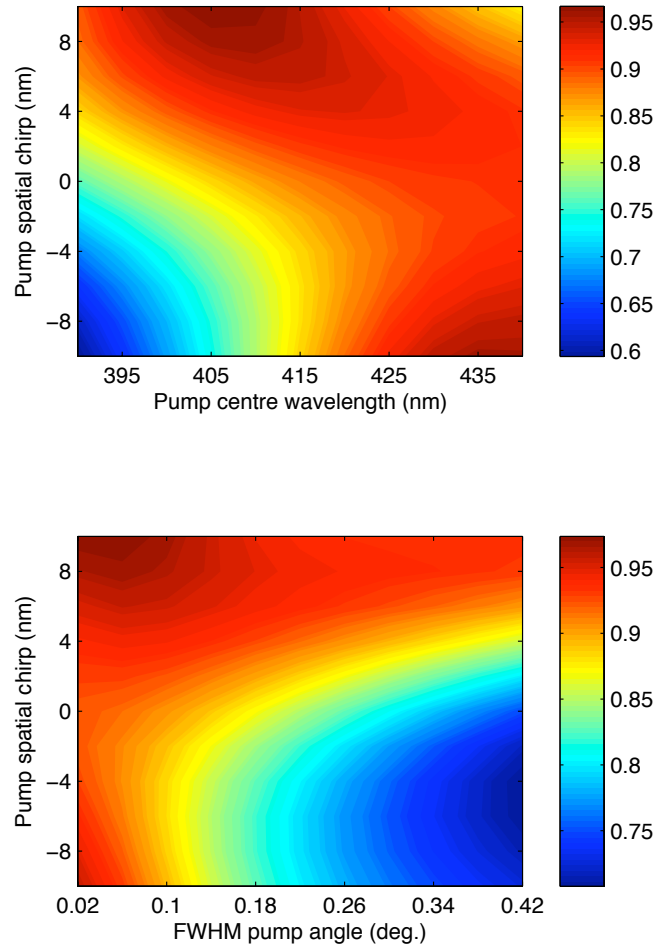


**Figure 4.17** Numerical optimisation plots showing the expected purity as a function of pump centre wavelength (top) and FWHM pump angle (bottom) against spatial chirp. In the first plot, the FWHM pump angle was  $0.16^\circ$  and in the second the pump wavelength was 415 nm. In both the pair collection angle was  $0.3^\circ$ . Note that in neither case does zero spatial chirp give the highest anticipated purity.

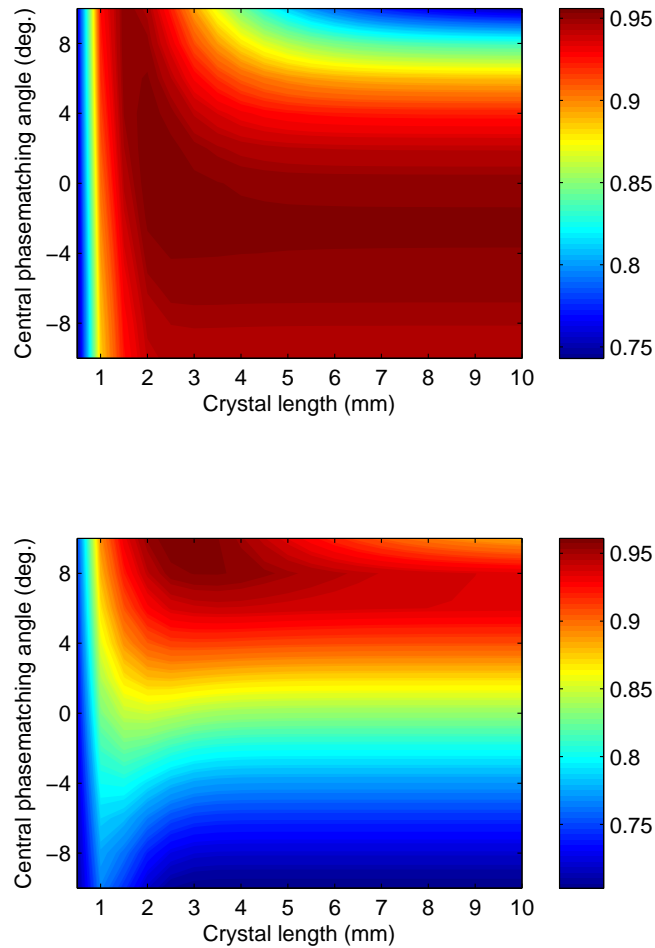


**Figure 4.18** Numerical optimisation plots showing the expected purity as a function of crystal length against central phasematching angle for 7.5 nm of spatial chirp in the positive direction (top) and negative direction (bottom). The central phasematching angle ( $\theta_{pm}$  in Figure 4.11) is expressed as the difference from collinear phase-matching at 830 nm. The FWHM pump angle was  $0.16^\circ$  and the pair collection angle was  $0.3^\circ$ .

is anywhere close to factorable, it is essential to understand the effects of spatial chirp. Although it was not considered in the initial proposals for factorable state generation, some spatial chirp can in fact be a help rather than a hinderance on the road to factorability, as shown in Figure 4.17. However, the spatial chirp and the crystal must be correctly orientated relative to one another — if they are not, the resulting state will be correlated. If the spatial chirp, pump focusing, and crystal are carefully matched though, the resulting state can be made highly factorable. This can be thought of as the change in pump frequency with angle due to the spatial chirp offsetting the shift in central downconversion wavelength that occurs as a result of the different phasematching conditions across the beam due to focusing. Hence these two effects can be made to cancel one another out and produce a factorable state. The exact focusing and crystal parameters required to achieve this are most easily found through the numerical model presented here as no simple relationship exists.

### 4.3 Joint spectral measurements

The final source configuration decided upon to yield the best combination of factorability and pair generation rate was a 5 mm KDP crystal cut for type-II phasematching at 830 nm, with the pump focused by a 250 mm focal length lens, and the emission from the crystal collimated by a 150 mm lens placed one focal length afterwards. This gave a FWHM pump angular intensity distribution of  $0.16^\circ$  and an intensity FWHM pair collection angle of  $0.30^\circ$ . A more detailed description of

the source setup is given in Chapter 5.

The predicted Schmidt number of the amplitude distribution resulting from a source using this set of parameters is  $K = 1.05$  for positive spatial chirp but  $K = 1.20$  if the spatial chirp is negative, as estimated using the numerical model outlined above. However, it was necessary to confirm this prediction by a direct measurement of the joint spectrum of the photon pairs<sup>149</sup> to check that such a source performs to the level suggested by the model.

To this end, two grating spectrometers were used to map the joint spectral intensity of the photon pairs<sup>111</sup>. This can quantify the degree of spectral correlation between the downconverted pairs, although it provides no information about the phase of the joint spectral amplitude and therefore the degree of temporal correlation remains unknown. With the e-ray downconverted photons having been coupled into one single-mode fibre and the o-rays into another (see Chapter 5 for details of the source alignment procedure), the exit faces of these two fibres replaced the entrance slits in two commercial grating spectrometers. The broadband o-rays were sent to an Andor Shamrock spectrometer (model number SR303I-B) with a 150 lines/mm grating blazed for 800 nm and the narrower e-rays to a Jobin-Yvon Triax 320 spectrometer with a 600 lines/mm grating blazed for 1  $\mu\text{m}$ . These gratings were chosen so that the angular dispersion of the e-ray photons would be about four times that of the o-ray photons and hence approximately equal to the inverse of the ratio of their spectral widths.

The output of each spectrometer was collected directly into a multimode fibre

without any coupling optics. The core diameter of these fibres therefore defined the effective resolution of the spectrometers: larger diameter fibres gave increased count rates but reduced the resolution. Three different core diameter fibres were available: 62.5  $\mu\text{m}$ , 105  $\mu\text{m}$ , and 200  $\mu\text{m}$  diameter. The fibre tips were both mounted on motorized  $x$  and manual  $yz$  translation stages. The two manual translation axes allowed for accurate positioning of the fibre tips at both the correct height and longitudinal position in the focal planes of the spectrometers. The motorized  $x$  translation moved the fibres transversely across the focal planes and hence controlled the central wavelength that each fibre collected. The motorised translation axes were carefully aligned to be parallel to the focal planes of each spectrometer, and both spectrometers were levelled to ensure that the gratings were not tilted away from vertical. Although the grating angles in both spectrometers could in theory have been computer controlled instead of moving the fibres, the age of this particular Triax spectrometer meant that the control software was not available. In addition, interfacing both spectrometers with the same LabView Virtual Instrument (VI) would have been much more time consuming than writing a VI to control the two stages. On the output end of each fibre was a silicon avalanche photodiode (APD) for photon counting (details of the detection scheme and counting electronics are also contained in Chapter 5). A diagram of the apparatus for the joint spectral intensity measurement is shown in Figure 4.19.

The resolution of the spectrometers was measured by coupling broadband pulses directly from the titanium:sapphire oscillator through each and plugging the outputs

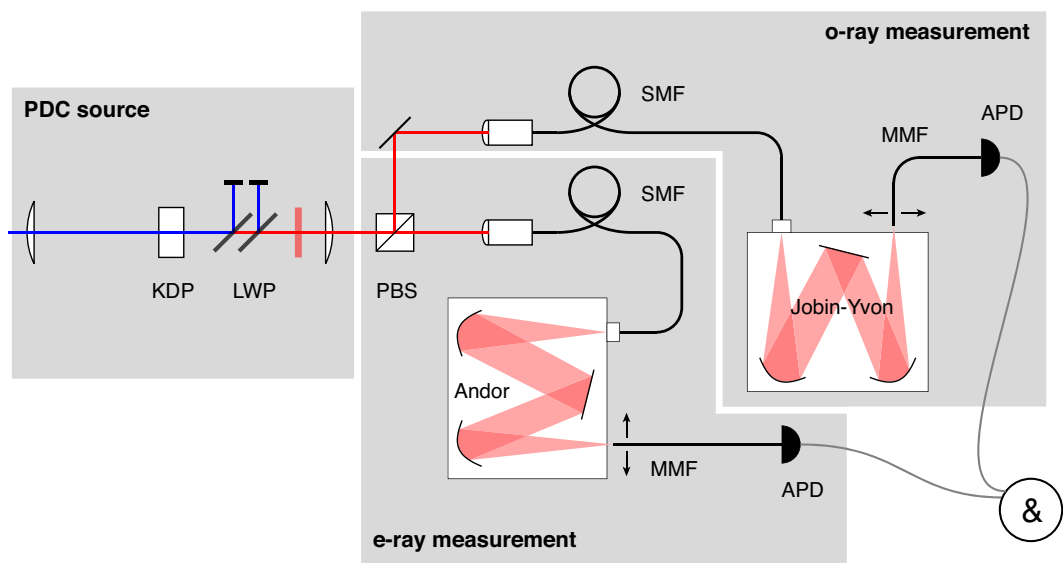


**Figure 4.19** Apparatus for measurement of joint spectra. KDP = downconversion crystal, LWP = long-wave-pass filter, PBS = polarising beamsplitter, SMF = single-mode fibre, MMF = multimode fibre, APD = avalanche photodiode.

of the multimode fibres into a high-resolution optical spectrum analyser (OSA, Ando AQ6317B). In order to make the measurement in an efficient manner, it is important to match the resolution of the spectrometers to the count rates available. Although it is clearly advantageous to make a high-resolution measurement of the joint spectrum, it must be mapped in two dimensions and therefore the time taken to make the measurement goes up with the square of the number of steps. In addition, to make the resolution high a smaller diameter fibre is required, and the number of photons collected goes down with the inverse square of the core diameter, and therefore it becomes necessary to count for longer at each position to obtain an adequate number of counts to ensure good statistics. Therefore the time required for each measurement is highly dependent on the fibre diameter and a compromise must be reached between count rates and resolution to make a good measurement (“good” being defined here as high enough resolution to show any correlations but not taking a prohibitively long time). So as not to waste counts, it is desirable to run each spectrometer at its resolution limit, so the size of each step should be the same as the resolution, i.e. approximately the core diameter of the fibre. For the count rates and resolution required here, the  $105\ \mu\text{m}$  core fibres gave the best performance, and it was these that were used for the measurements presented herein. OSA data for these fibres are shown for both spectrometers in Figure 4.20. The maximum resolution for each spectrometer with these fibres on the outputs was found from the FWHM of the OSA traces: 0.5 nm in the case of the Jobin-Yvon (e-ray) spectrometer and 2 nm for the Andor (o-ray).

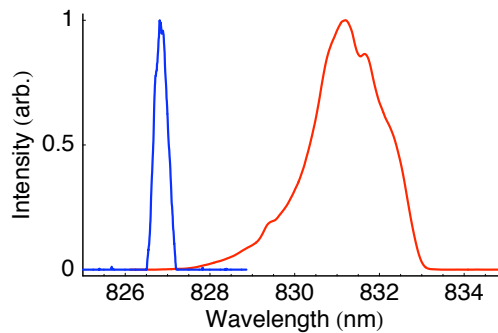


**Figure 4.20** Data from the OSA measurements demonstrating the resolutions of the two spectrometers with the  $105\mu\text{m}$  fibres on each output. The Andor spectrometer trace is shown in red, and the Jobin-Yvon in blue.

Both spectrometers were calibrated against the same factory-calibrated Ocean Optics USB2000 spectrometer. The narrowband spectrum obtained by running the oscillator in continuous wave (CW) mode was first measured with the Ocean Optics spectrometer to ascertain its central wavelength. The beam was then sent to each of the other two spectrometers in turn and, with a power meter on the output of the multimode fibre, the throughput was maximised by translating the fibre tip with only the motorised stage. The position of the stage was then recorded, and the process repeated at a number of different wavelengths spanning the range in which the downconversion was to be measured. In this way a calibration curve was built up for each spectrometer, as plotted in Figure 4.21.

With the downconversion coupled through the spectrometers, monitoring the coincidence rates between the two APDs while scanning independently the two stages allowed the joint spectral intensity to be mapped out. The movement of the stages and the photon counting was controlled by a custom-built LabView VI. The fibres

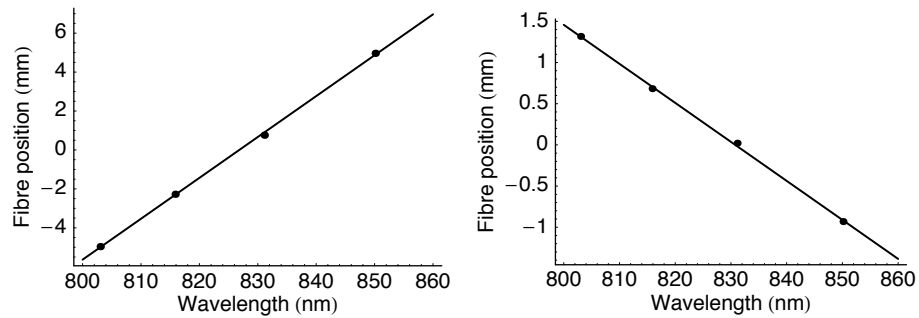


**Figure 4.21** Wavelength calibration data for the spectrometers. Jobin-Yvon on the left, Andor on the right.

were scanned across the required wavelength range in a series of 16 steps, covering approximately 10 nm by 40 nm for e- and o-ray respectively. The step sizes along each axis in this grid were therefore not equal; the e-ray was sampled at intervals of just over 0.5 nm, and the o-ray in steps slightly greater than 2 nm. Therefore both spectrometers were stepped in increments close to their respective resolutions. The joint spectral data was acquired by first setting the o-ray wavelength via the translation stage on the Andor spectrometer output, and then moving the stage after the Jobin-Yvon spectrometer to each of the proscribed e-ray wavelength settings in turn. For each pair of wavelengths the coincidence counts were recorded for a period of 60 s. After each e-ray scan was complete the o-ray stage moved to its next point and the process was repeated. The source configuration was as outlined at the beginning of this section and joint spectra were taken for both positive and negative spatial chirp by rotating the crystal about the  $z$ -direction.

The experimental data are presented in Figure 4.22 alongside the joint spectral

distributions predicted by the numerical model given the same source parameters. It can be seen that the agreement between the two is very good for both positive and negative spatial chirp. The experimental spectral intensity distribution is highly factorable in the case of positive chirp; if flat spectral phase is assumed across the corresponding joint amplitude distribution, the associated Schmidt number is 1.02. On the other hand, for negative chirp the joint state is much less factorable, with  $K = 1.14$ .

This can be compared more quantitatively with the output of the model by finding the Schmidt number for the amplitude distribution predicted by the model assuming that we have no information about the phase. This was done by calculating the SVD of the square root of the joint spectral intensity rather than directly from the joint amplitude. The comparison between the model and the data is displayed in Table 4.1, along with the figures for the model inclusive of its phase. It can be seen that the model accurately predicts the Schmidt number expected for the measured intensity distribution for both directions of chirp, but the true Schmidt number for the predicted amplitude distribution including phase is a little higher. It is from this final Schmidt number that the expected visibility for the interference of heralded photons from each distribution can be calculated. For a positively-chirped pump beam, this gives a projected maximum purity and visibility of just over 0.95.

A further method of comparing the correlations present in each spectrum is to plot the e-ray wavelength at which the maximum count rate occurs at every o-ray point. For the experimental data, this is most accurately done by fitting each data

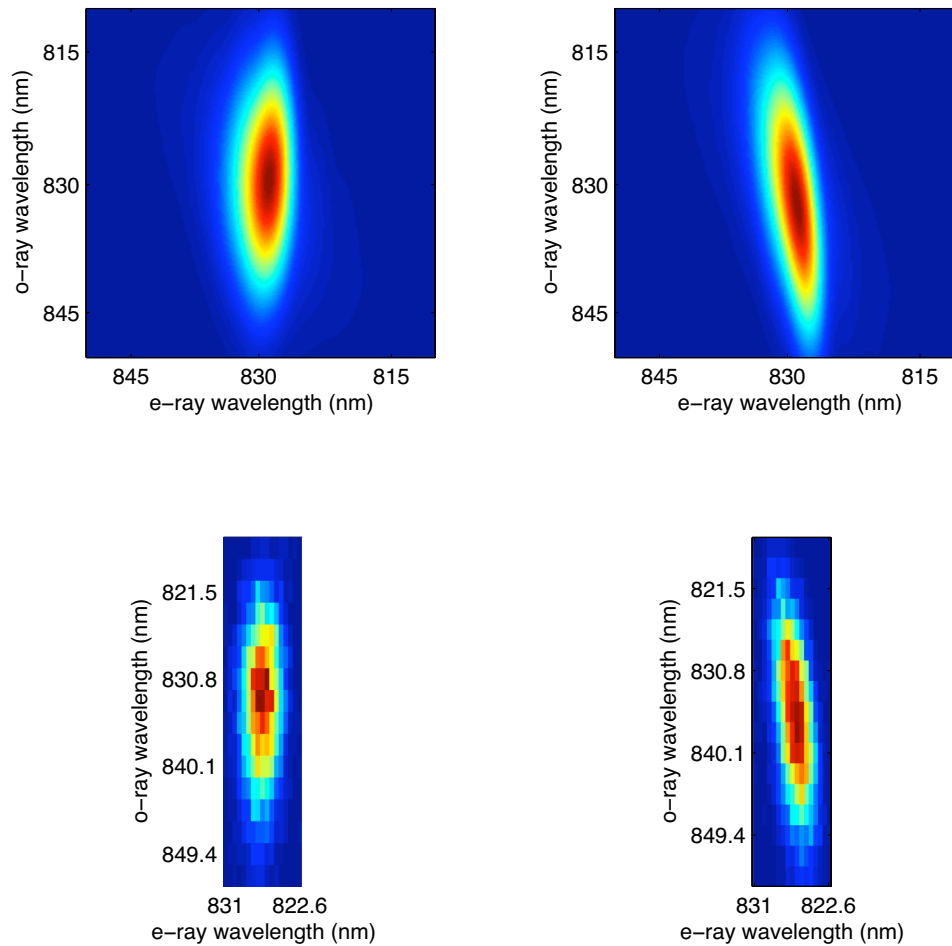


**Figure 4.22** Top: Joint spectra calculated from the numerical model for the measured experimental parameters with positive spatial chirp (left) and negative spatial chirp (right). Bottom: Measured joint spectral probability distributions for positive spatial chirp (left) and negative spatial chirp (right).

	Positive chirp		Negative chirp	
	$K$	$\mathcal{P}$	$K$	$\mathcal{P}$
Data	1.02	0.979	1.12	0.894
Model (no phase)	1.03	0.970	1.17	0.854
Model (with phase)	1.05	0.953	1.19	0.839

**Table 4.1** Comparison of Schmidt number ( $K$ ) and projected purity ( $\mathcal{P}$ ) for the measured joint intensity distributions, the model without any phase, and the model with phase for both spatial chirp directions.

slice at constant o-ray wavelength with a Gaussian distribution in e-ray wavelength. The centres of these fits can then be plotted against the o-ray wavelength at which they were taken. As the results from the model are at much higher resolution and are therefore more smoothly varying, it is adequate for these plots to simply take the e-ray wavelength that gives the maximum value of the intensity distribution at each o-ray wavelength.

The results of this process are shown in Figures 4.23 and 4.24. For the measured spectra, in the case of the uncorrelated spectrum resulting from positive spatial chirp on the pump beam, it can be seen that the centre of the e-ray spectrum is almost constant over the entire o-ray spectrum. The fit line to these e-ray central wavelength points changes by only half a nanometre over 30 nm of o-ray bandwidth, again demonstrating the factorable nature of this state. However, for negative spatial chirp, the e-ray centre wavelength is anti-correlated with o-ray wavelength and appears to exhibit a quadratic dependence. This can be compared to the results from the model in Figure 4.24 which display the same behaviour.

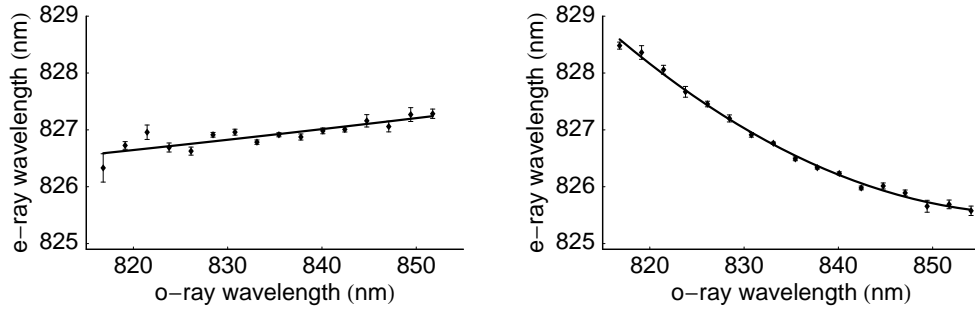


**Figure 4.23** Central e-ray wavelengths of Gaussian fits to slices of constant o-ray wavelength from measured joint spectra. The dependence in the case of positive pump spatial chirp is shown on the left and negative chirp on right. The lines are quadratic fits to the data to guide the eye.

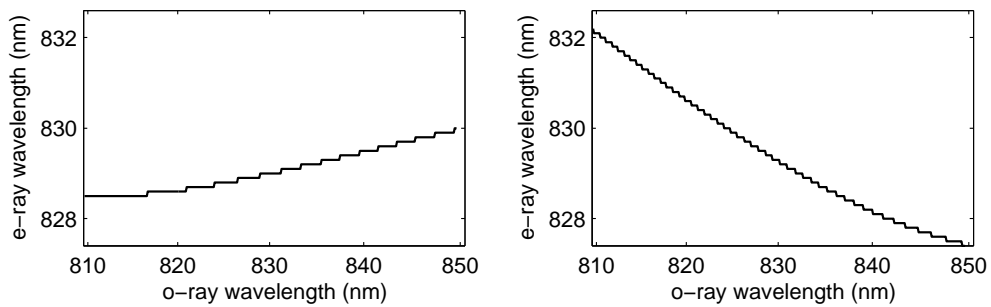


**Figure 4.24** e-ray wavelength giving maximum spectral intensity as a function of o-ray wavelength for joint spectra calculated by model using experimental parameters. Positive chirp on the left and negative chirp on the right.

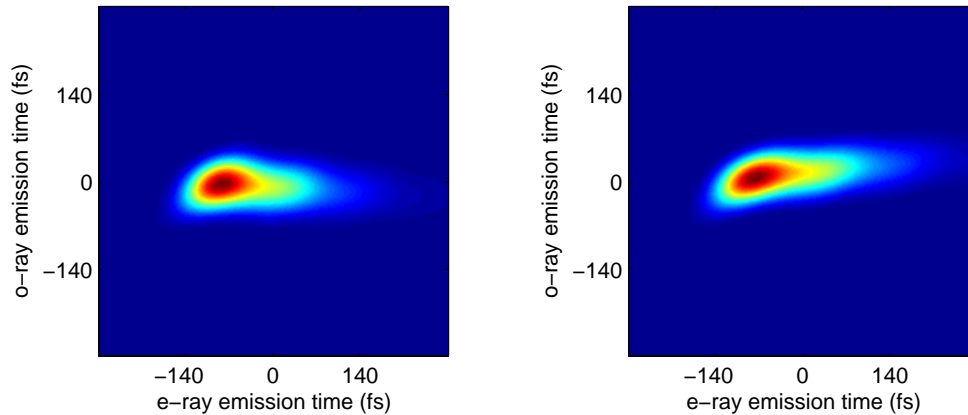


**Figure 4.25** The simulated joint temporal intensity distributions for downconversion from KDP in the case of positive (left) and negative (right) spatial chirp. For positive chirp, it can be seen that the temporal structure is approximately single mode. It is this that gives the photons their exceptionally low timing jitter.

The high level of agreement between the simulated and measured spectral data allows the numerical model to be used to estimate the temporal structure of the photon pairs. This cannot be done from the experimental spectra as the data is an intensity measurement alone and any phase information (that can lead to temporal correlations) is lost. However, by taking the numerical Fourier transform of the simulated spectral amplitudes in the case of positive and negative chirp, we gain some insight into the temporal distribution of the photon pairs. The results of this are shown in Figure 4.25; the difference between the lack of any temporal correlation in the case of positive spatial chirp and the tilt of the joint temporal intensity distribution for negative chirp can be clearly seen.

	Positive chirp		Negative chirp	
	e-ray	o-ray	e-ray	o-ray
Model	5.4 nm	21.0 nm	5.4 nm	25.0 nm
Data	3.5 nm	16.4 nm	3.4 nm	19.8 nm

**Table 4.2** Comparison of FWHM bandwidths of the marginal frequency distributions calculated from the model and the measured joint spectral data.

Finally, the measurements on the joint spectrum provide a means of estimating the bandwidths of the daughter photons from the marginal distributions of both the e-ray and o-ray. The marginal frequency distribution of each photon is found by integrating over the frequency of the other photon — the results of these sums on the joint spectral data are shown in the cases of both positive and negative chirp in Figure 4.26. These are compared with the estimations of the bandwidths found from the marginal distributions calculated by the numerical model in Table 4.2. The bandwidths from both agree reasonably well, especially in the trends displayed: the e-ray bandwidths remain approximately constant for both spatial chirps but the o-ray bandwidths are significantly broader in the case of negative chirp. However, the model overestimates the bandwidths in all cases.

## 4.4 Second order coherence measurement

An important test of the quality of a single photon source is to demonstrate that its output does indeed consist of single photons, and that, when a single photon is present in the output mode, the probability of there being a second photon present

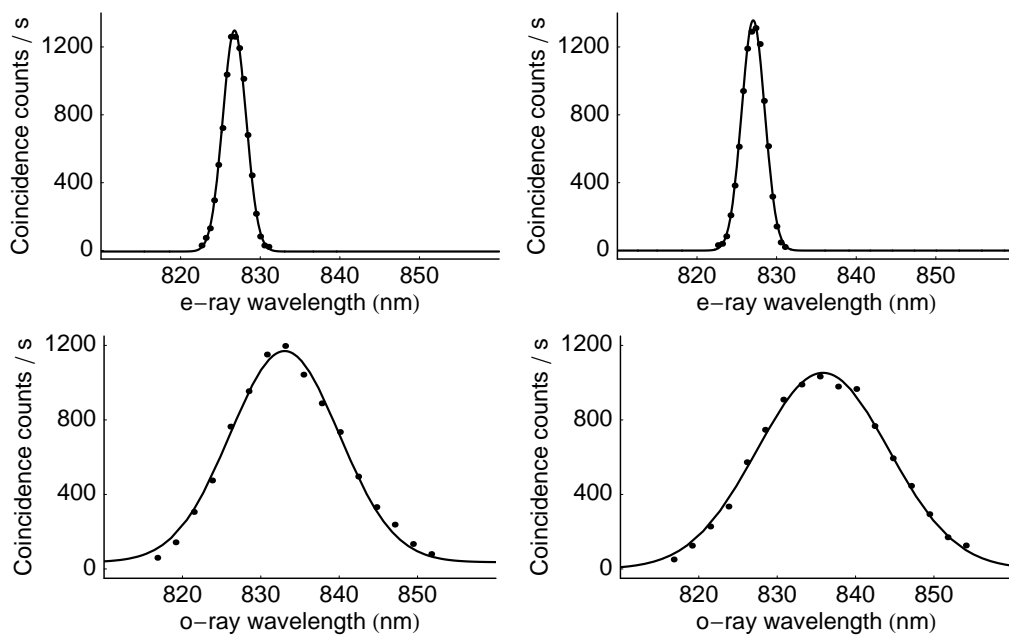


**Figure 4.26** Marginal distributions of measured joint spectra for e-rays (top) and o-rays (bottom) with positive chirp on the left and negative on the right.

simultaneously is low. In the case of a downconverter, this can be done by measuring the degree of second order coherence of the heralded beam in the manner of Hanbury-Brown and Twiss<sup>150</sup>. The classical definition of the second order coherence is<sup>23</sup>

$$g^{(2)}(\tau) = \frac{\langle \bar{I}(t)\bar{I}(t+\tau) \rangle}{\langle \bar{I}(t) \rangle^2} = \frac{\langle E^*(t)E^*(t+\tau)E(t+\tau)E(t) \rangle}{\langle E^*(t)E(t) \rangle^2}, \quad (4.15)$$

where  $\bar{I}(t)$  is the cycle-averaged intensity at time  $t$  and angle brackets denote a statistical average over a time long compared to the coherence time.  $g^{(2)}(\tau)$  is therefore a measure of the normalised level of intensity correlation for the same beam at times separated by  $\tau$ . For a classical light source, the definition of  $g^{(2)}(\tau)$  in terms of the real intensities  $\bar{I}(t)$  permits the application of Cauchy's inequality<sup>151</sup>, relating any real numbers  $\bar{I}_1$  and  $\bar{I}_2$  by

$$2\bar{I}_1\bar{I}_2 \leq \bar{I}_1^2 + \bar{I}_2^2. \quad (4.16)$$

Through this it can be demonstrated for any classical light source that the degree of second order coherence at  $\tau = 0$  must satisfy the inequality

$$1 \leq g_{\text{cl}}^{(2)}(0) \leq \infty. \quad (4.17)$$

To obtain an expression for  $g^{(2)}(\tau)$  that is valid for quantized fields, one simply replaces the classical field amplitudes in the final part of Equation 4.15 with their quantum mechanical field operator counterparts. However, in this case, it cannot be

proven that the inequality in Equation 4.17 holds, as the definition of  $g^{(2)}(\tau)$  does not reduce to the same relationship between the intensities. The only condition that must be fulfilled by  $g^{(2)}(0)$  for a nonclassical light source is that of positivity:

$$0 \leq g_{\text{qu}}^{(2)}(0) \leq \infty, \quad (4.18)$$

because the value of  $g^{(2)}(\tau)$  depends on the expectation values of the products of operators and their Hermitian conjugates. Therefore, any measurement that places  $g^{(2)}(0)$  in the range between zero and one suggests that a light source is nonclassical. Indeed, for a perfect single photon source one would always obtain  $g^{(2)}(0) = 0$ , demonstrating that it would never be possible to detect two photons emitted simultaneously by the source. Such measurements have been performed on a wide range of single photon sources<sup>26,41,152,153</sup>.

A straightforward measurement of  $g^{(2)}(0)$  for the KDP downconversion source was performed following the method set out by U'Ren *et al*<sup>154</sup>, a schematic of which is shown in Figure 4.27. The pairs from one downconverter were split; one half of each pair was sent directly to a detector as a herald, and the other half to a 50:50 beamsplitter (in this case actually a 50:50 single mode fibre coupler) with one detector on each output. The rate of single detection events (“singles”) for all detectors ( $R_h$ ,  $R_{s1}$ , and  $R_{s2}$  for herald, signal 1, and signal 2 respectively) and coincidence detection events (“coincidences”) between the herald detector and either ( $C_{h,1}$  and  $C_{h,2}$ ) or both ( $C_{h,1,2}$ ) of the signal detectors following the beamsplitter

were recorded. Thus, the probability of detecting a single photon in either of the signal arms for each heralding event that occurs is

$$P_1 = \frac{C_{h,1} + C_{h,2}}{R_h} \quad (4.19)$$

and the probability of detecting two signal photons for every herald is

$$P_2 = \frac{C_{h,1,2}}{R_h}. \quad (4.20)$$

The value of  $g^{(2)}(0)$  is then found from the ratio of the probability of generating two signal photons for one herald detection to the square of the probability of generating only one:

$$g^{(2)}(0) = \frac{2P_2}{P_1^2} = \frac{2R_h C_{h,1,2}}{(C_{h,1} + C_{h,2})^2} \quad (4.21)$$

where the factor of 2 in the numerator arises from the 50:50 split ratio of the beam-splitter. Putting the measured numbers for the KDP source into this formula gave the value of the second order coherence as  $g^{(2)}(0) = (5 \pm 1) \times 10^{-3}$ . This is very low for a bulk PDC source and is comparable with the best  $g^{(2)}(0)$  figures measured for other sources currently available. It demonstrates that this is a high-performance source in terms of the single photon nature of the heralded output.

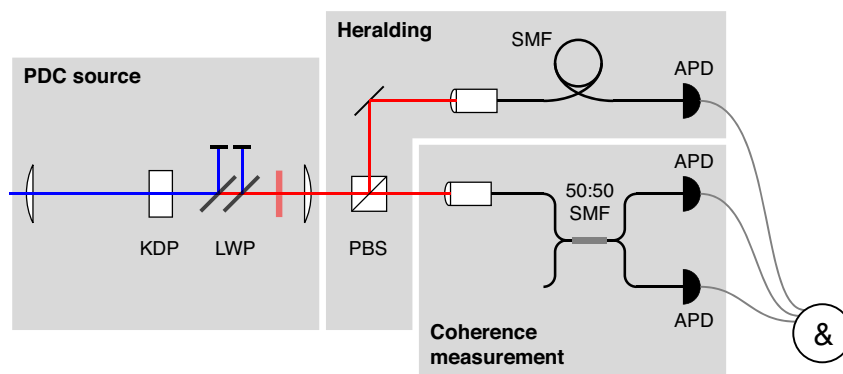


**Figure 4.27** Apparatus for  $g^{(2)}(0)$  measurement. Labels as in Figure 4.19, and 50:50 SMF = 50:50 single-mode fibre coupler.



## Chapter 5

# Multiple source interferometry:

## A purity test

At the beginning of Chapter 3 the HOMI visibility for two identically impure photons was found to be equal to their purity. This result, expressed in Equation 3.11, demonstrates that the condition for high-visibility interference between two single photons is not only that they are indistinguishable but also that they are both in pure states.

Furthermore it was shown in Section 3.1 that the heralded single photons from a downconversion source will only be pure if they are derived from factorable pairs. Considering these two findings in the light of one another, it becomes clear that high-visibility interference between single photons from two independent sources can only be achieved if those sources generate factorable pairs, or, conversely, that the visibility of the interference gives a measure of the factorability for two iden-

tical sources. This relationship can be derived from first principles by calculating the heralding and subsequent interference of photons from two initially pure pairs prepared in independent sources. A similar calculation was performed by Grice<sup>155</sup> in the context of factorable state generation.

This twin-source HOMI calculation is outlined in the first section of this chapter and the result used to study the dependence of the interference pattern on the overlap between the two photons being interfered. The relationship between the coherence time of the photons and the dip width is found. A new method of placing a lower bound on the purity of two partially distinguishable photons from their interference visibility is presented, based on the calculation at the beginning of Chapter 3 combined with an overlap measure. A detailed description of the construction, alignment, and operation of the apparatus to experimentally demonstrate pure heralded single photon generation is presented. Finally, the resulting data for the HOMI interference of both the e-ray and o-ray photons are shown, along with an optimization of the source heralding efficiency.

## 5.1 Twin-source HOMI calculation

A schematic of the experiment is shown in Figure 5.1. The initial four-photon state is the product of two photon pairs, created in two independent sources:

$$\begin{aligned}
 |\Psi_4\rangle = & \int_0^\infty d\omega_{e1} \int_0^\infty d\omega_{o1} \int_0^\infty d\omega_{e2} \int_0^\infty d\omega_{o2} \\
 & f_1(\omega_{e1}, \omega_{o1}) f_2(\omega_{e2}, \omega_{o2}) \hat{a}_{e1}^\dagger(\omega_{e1}) \hat{a}_{o1}^\dagger(\omega_{o1}) \hat{a}_{e2}^\dagger(\omega_{e2}) \hat{a}_{o2}^\dagger(\omega_{o2}) |0\rangle,
 \end{aligned} \tag{5.1}$$

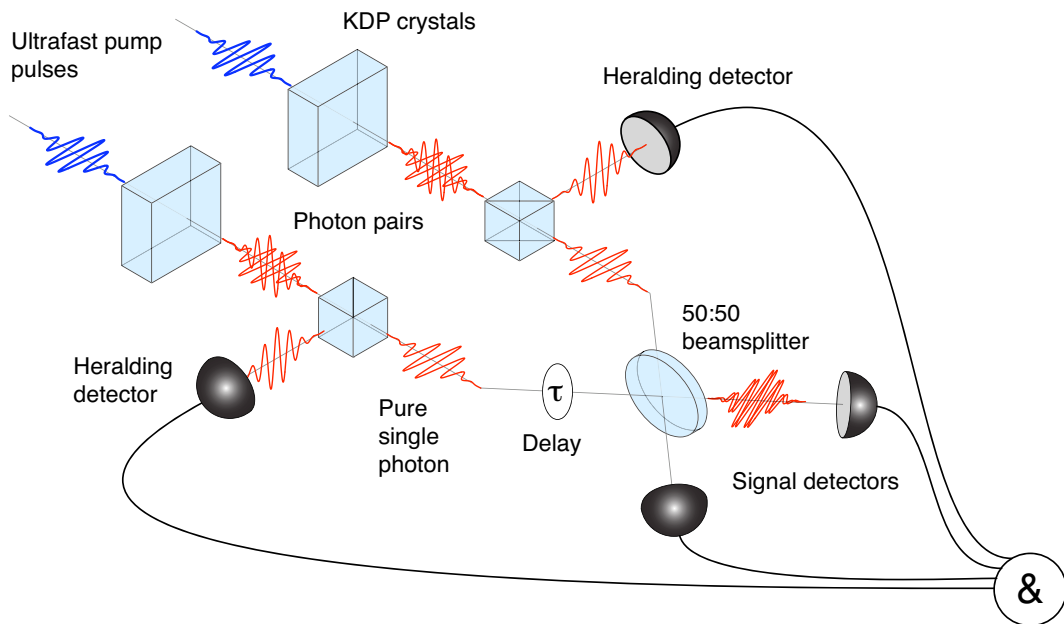


**Figure 5.1** Schematic representation of the twin-crystal HOMI experiment.

where the labels on the creation operators are to denote whether the photon is e- or o-ray and the source that they originated from (1 or 2). One photon from each pair is split off as a herald and the remaining photons are interfered at a 50:50 beamsplitter.

To observe the HOMI between the two heralded photons, we are interested in the rate of fourfold coincidences at both heralding detectors (labelled  $h1$  and  $h2$ ) and both signal detectors (labelled  $s1$  and  $s2$ ) as a function of the relative time delay  $\tau$  between the two pairs. The operator for detection of all four photons at times

$t_{h1}, t_{h2}, t_{s1}, t_{s2}$  for the two herald and two signal photons respectively is

$$\begin{aligned} \hat{\Pi}_{4C}(t_{h1}, t_{h2}, t_{s1}, t_{s2}) &= \hat{E}_{h1}^{(-)}(t_{h1})\hat{E}_{h2}^{(-)}(t_{h2})\hat{E}_{s1}^{(-)}(t_{s1})\hat{E}_{s2}^{(-)}(t_{s2})|0\rangle \\ &\langle 0|\hat{E}_{s2}^{(+)}(t_{s2})\hat{E}_{s1}^{(+)}(t_{s1})\hat{E}_{h2}^{(+)}(t_{h2})\hat{E}_{h1}^{(+)}(t_{h1}) \end{aligned} \quad (5.2)$$

where the electric field operators are defined as in Equation 2.9 but here we consider only the frequency degree of freedom. By mapping this operator onto the source modes using the beamsplitter relations (including an additional phase from the time delay) the positive frequency parts of these field operators are

$$\hat{E}_{h1}^{(+)}(t_{h1}) = \int_0^\infty d\omega_{h1} \hat{a}_{o1}(\omega_{h1})e^{-i\omega_{h1}t_{h1}} \quad (5.3)$$

$$\hat{E}_{h2}^{(+)}(t_{h2}) = \int_0^\infty d\omega_{h2} \hat{a}_{o2}(\omega_{h2})e^{-i\omega_{h2}t_{h2}} \quad (5.4)$$

$$\hat{E}_{s1}^{(+)}(t_{s1}) = \frac{1}{\sqrt{2}} \int_0^\infty d\omega_{s1} [\hat{a}_{e1}(\omega_{s1})e^{-i\omega_{s1}\tau} + \hat{a}_{e2}(\omega_{s1})] e^{-i\omega_{s1}t_{s1}} \quad (5.5)$$

$$\hat{E}_{s2}^{(+)}(t_{s2}) = \frac{1}{\sqrt{2}} \int_0^\infty d\omega_{s2} [\hat{a}_{e1}(\omega_{s2})e^{-i\omega_{s2}\tau} - \hat{a}_{e2}(\omega_{s2})] e^{-i\omega_{s2}t_{s2}}. \quad (5.6)$$

The probability of a fourfold detection event at times  $t_{h1}, t_{h2}, t_{s1}, t_{s2}$  can be found from

$$P_{4C}(t_{h1}, t_{h2}, t_{s1}, t_{s2}) = \langle \hat{\Pi}_{4C} \rangle = \langle \Psi_4 | \hat{\Pi}_{4C} | \Psi_4 \rangle = |\langle \hat{E}_{4C}^{(+)} | \Psi_4 \rangle|^2, \quad (5.7)$$

where  $\hat{E}_{4C}^{(+)}$  is the positive frequency part of  $\hat{\Pi}_{4C}$  and the time dependences have been dropped for clarity. Performing this calculation and making the assumption that the detectors used are slow compared to the interaction time at the beamsplitter, we can then integrate over all possible detection times to find the probability of a

fourfold coincidence as a function of the time delay  $\tau$ :

$$P_{4C}(\tau) = \frac{1}{4} \int_0^\infty \cdots \int_0^\infty d\omega_{h1} d\omega_{h2} d\omega_{s1} d\omega_{s2} \left| f_1(\omega_{s1}, \omega_{h1}) f_2(\omega_{s2}, \omega_{h2}) - f_1(\omega_{s2}, \omega_{h1}) f_2(\omega_{s1}, \omega_{h2}) e^{-i(\omega_{s2} - \omega_{s1})\tau} \right|^2. \quad (5.8)$$

For perfect interference we require  $P_{4C}(\tau)$  to go to zero when the two photons are coincident on the beamsplitter at  $\tau = 0$ . From Equation 5.8 it is clear that this can only happen if

$$f_1(\omega_{s1}, \omega_{h1}) f_2(\omega_{s2}, \omega_{h2}) = f_1(\omega_{s2}, \omega_{h1}) f_2(\omega_{s1}, \omega_{h2}). \quad (5.9)$$

To satisfy this condition for all  $\omega$ , firstly the two joint spectral amplitudes must be equal:

$$f_1(\omega_s, \omega_h) = f_2(\omega_s, \omega_h) = f(\omega_s, \omega_h), \quad (5.10)$$

and secondly they must both be factorable:

$$f(\omega_s, \omega_h) = g_s(\omega_s) g_h(\omega_h). \quad (5.11)$$

Equation 5.10 corresponds to indistinguishability between the photons and Equation 5.11 to the purity of each photon individually. So for perfect interference, the photon pairs must be in factorable states. Note that the situation of interfering independent photons from separate sources described here is distinct from that shown by Hong, Ou, and Mandel in the first HOMI experiment<sup>14</sup> and many subsequent single source

demonstrations. With a single PDC source, high-visibility HOMI interference can be seen upon interfering the two daughter photons from the same pair even when they exhibit strong correlations as long as the pair is symmetric. However, such a source cannot be used for pure single photon generation and, when two are operated independently, the interference between photons from different pairs will be poor.

For pairs satisfying the criteria for factorability, the integration over the herald frequencies in Equation 5.8 is trivial and the expression for the interference pattern becomes

$$P_{4C}(\tau) = \frac{1}{4} \int_0^\infty \int_0^\infty d\omega_{s1} d\omega_{s2} \left| g_{s1}(\omega_{s1}) g_{s2}(\omega_{s2}) - g_{s1}(\omega_{s2}) g_{s2}(\omega_{s1}) e^{-i(\omega_{s2} - \omega_{s1})\tau} \right|^2. \quad (5.12)$$

This holds for two pure photons with arbitrary frequency distributions. Taking the photon spectra to be normalised Gaussian frequency distributions

$$g_{s\mu}(\omega_{s\mu}) = \sqrt{\frac{2}{\pi\sigma_{s\mu}^2}} \exp \left[ - \left( \frac{\omega_{s\mu} - \omega_{s\mu,0}}{\sigma_{s\mu}} \right)^2 \right], \quad (5.13)$$

where  $\omega_{s\mu,0}$  is the mean frequency and  $\mu = 1,2$ , and substituting into Equation 5.12, the probability of a fourfold coincidence becomes

$$P_{4C}(\tau) = \frac{1}{2} - \frac{\sigma_{s1}\sigma_{s2}}{\sigma_{s1}^2 + \sigma_{s2}^2} \exp \left[ - \left( \frac{\sigma_{s1}^2\sigma_{s2}^2\tau^2 + 4(\omega_{s2,0} - \omega_{s1,0})^2}{2(\sigma_{s1}^2 + \sigma_{s2}^2)} \right) \right]. \quad (5.14)$$

Plots of this interference dip for various parameters are shown in Figure 5.2.

For two photons with equal frequency bandwidths  $\sigma_s$ , the FWHM of the dip is

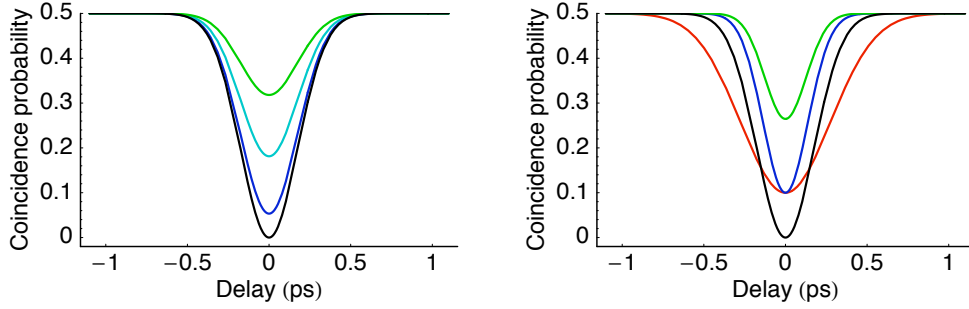


**Figure 5.2** Interference dips plotted for pure heralded photons. The black plots are for completely indistinguishable photons and therefore have  $V = 1$ . In the left panel, both photons have bandwidths of 3.5 nm, one is centered at 830 nm and the other is offset by 1 nm (dark blue,  $V = 0.89$ ), 2 nm (light blue,  $V = 0.64$ ), and 3 nm (green,  $V = 0.36$ ). In the right panel, both photons are centered at 830 nm, one has a bandwidth of 3.5 nm while the bandwidth of the other is multiplied by a half (red,  $V = 0.80$ ), two (blue,  $V = 0.80$ ), and four (green,  $V = 0.47$ ). Note that the halfwidth of the cases with varying central wavelength remains constant but changes with bandwidth.

found to be:

$$\delta\tau = \frac{4\sqrt{\ln 2}}{\sigma_s}. \quad (5.15)$$

Note that, as long as the photons are identical and can be assumed to have simple Gaussian distributions, the dip width does not depend on their temporal profile (for example any quadratic phase resulting in temporal chirp or other higher-order phase contributions), only on the inverse of their bandwidth. Hence the dip does not measure the photons' duration. Furthermore, in order to be considered to have any temporal overlap at the beamsplitter, two photons that are not transform-limited must be coincident to within their coherence time rather than their duration. Defining the coherence time as the halfwidth of the temporal intensity distribution,

taking the inverse Fourier transform of the spectral amplitude of these photons gives a coherence time of

$$t_c = \frac{2\sqrt{2 \ln 2}}{\sigma_s}, \quad (5.16)$$

and the relationship between the dip width and the coherence time is therefore

$$t_c = \frac{\delta\tau}{\sqrt{2}}. \quad (5.17)$$

This expression allows the coherence time of the photons as measured by the HOMI dip to be compared with that from the photon spectra.

The effect on the interference visibility of a beamsplitter whose split ratio is not exactly 50:50 can be investigated by modifying Equations 5.5 and 5.6 to include explicitly the amplitude coefficients for reflection and transmission,  $\mathcal{R}$  and  $\mathcal{T}$ , as in Section 1.8. The fourfold coincidence probability for identical pure photons is then

$$P_{4C}(\tau) = \mathcal{R}^4 + \mathcal{T}^4 - 2\mathcal{R}^2\mathcal{T}^2 \exp\left[-\frac{\sigma_s^2\tau^2}{4}\right]. \quad (5.18)$$

Applying the energy-conserving condition  $\mathcal{R}^2 + \mathcal{T}^2 = 1$ , the visibility is found from Equation 1.16 to be

$$V(\mathcal{R}) = \frac{2\mathcal{R}^2 - 2\mathcal{R}^4}{1 - 2\mathcal{R}^2 + 2\mathcal{R}^4} \quad (5.19)$$

This is plotted in Figure 5.3. It can be seen that, close to  $\mathcal{R}^2 = 0.5$  the visibility varies relatively slowly with changing  $\mathcal{R}$ . Hence a beamsplitter with a split ratio as poor as 40:60 can still give visibilities of over 90%.

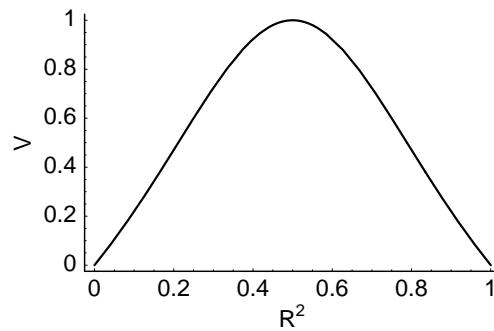


**Figure 5.3** Visibility of fourfold coincidence HOMI interference pattern as a function of beamsplitter reflectivity.

## 5.2 Resolving distinguishability and purity

Photon pairs with joint spectra calculated directly from the Sellmeier equations will, even in the case of KDP, exhibit some level of correlation, and pairs generated in independent sources will inevitably not be identical. In this more realistic situation, the integrals in Equation 5.8 can no longer be separated and performed analytically. It is therefore difficult to distinguish the contributions to the loss of visibility from impurity in the heralded photons from those due to imperfect overlap. However, we can bring to bear the tools introduced in earlier chapters and hence settle the question.

We wish to be able to resolve the contributions to any loss in visibility from the two distinct effects of imperfect mode matching resulting in distinguishability between the two photons and imperfect interference due to impurity in each individual photon. Referring back to the calculation of the interference of two mixed-state photons at a beamsplitter in Chapter 3 allows us to find an expression for the visibility

in the case of distinguishable photons. From Equations 3.10 and 3.11, if the two distributions are assumed to be different, the visibility is now given by

$$V = \sum_{i=j} p_{1i} p_{2j} = \text{Tr}(\hat{\rho}_1 \hat{\rho}_2). \quad (5.20)$$

This contains contributions to non-unit visibility from both poor overlap and impurity and, in order to successfully separate these two effects, we require a measure of the overlap of the two states. However, many commonly used benchmarks, such as the fidelity or the trace distance, are inappropriate to this application as they incorporate traces of square roots of matrices and therefore cannot be rearranged as necessary. Furthermore they cannot be easily related to experimentally measurable qualities. One more suitable criterion is the operational distance, also known as the Hilbert-Schmidt norm. This defines the distinguishability to be<sup>156</sup>:

$$O(\hat{\rho}_1, \hat{\rho}_2) = \|\hat{\rho}_1 - \hat{\rho}_2\|^2, \quad (5.21)$$

where  $\|\hat{A}\|^2$  is the Frobenius norm, defined as  $\text{Tr}\{A^\dagger A\}$ . Expanding Equation 5.21, we can write

$$\begin{aligned} O(\hat{\rho}_1, \hat{\rho}_2) &= \text{Tr}\{(\hat{\rho}_1 - \hat{\rho}_2)^\dagger (\hat{\rho}_1 - \hat{\rho}_2)\} \\ &= \text{Tr}\{(\hat{\rho}_1)^2\} + \text{Tr}\{(\hat{\rho}_2)^2\} - 2\text{Tr}\{\hat{\rho}_1 \hat{\rho}_2\}, \end{aligned} \quad (5.22)$$

and rearranging with the help of Equation 5.20 we find the result for the visibility

in terms of both the purities and the overlap:

$$V = \frac{\mathcal{P}_1 + \mathcal{P}_2 - O(\hat{\rho}_1, \hat{\rho}_2)}{2}. \quad (5.23)$$

The operational distance is zero for indistinguishable states and two for perfectly distinguishable states. This result confirms that, for indistinguishable states, the visibility is simply a measure of the mean purity.

In addition, Equation 5.23 can be used to find a minimum level of purity given a particular level of overlap between the states. For two photons in pure but distinguishable states, the visibility would be the maximum possible for that level of distinguishability. If the photon spectra were known, one could find the contribution to the loss of visibility from that distinguishability. This gives an upper bound on the visibility given the level of overlap and hence a lower bound on the purity. Substituting two distinguishable pure states,  $\hat{\rho}_1 = |\psi_1\rangle\langle\psi_1|$  and  $\hat{\rho}_2 = |\psi_2\rangle\langle\psi_2|$ , into Equation 5.20, the maximum visibility for any two distinguishable states is found to be

$$V_{\max} = \text{Tr}\{|\psi_1\rangle\langle\psi_1|\psi_2\rangle\langle\psi_2|\} = |\langle\psi_1|\psi_2\rangle|^2. \quad (5.24)$$

This overlap can be calculated by measuring the spectrum of each photon. Hence the minimum experimental purity can be found given that the maximum possible visibility,  $V_{\max}$ , is known for the level of spectral distinguishability present. Assuming that the purity of both photons is approximately the same, this minimum purity

is the ratio between  $V_{\max}$  and the measured visibility,  $V_{\text{expt}}$ :

$$\mathcal{P}_{\min} = \frac{V_{\text{expt}}}{V_{\max}}. \quad (5.25)$$

Therefore, for a given measured interference visibility we can place a definite lower bound on the purity of the heralded single photons. This result is used in Section 5.3.4 to find the minimum purity from the experimental data.

## 5.3 Twin-source HOMI experiment

### 5.3.1 Experimental apparatus

The experimental apparatus for the twin source HOMI experiment is displayed in Figure 5.4. A titanium:sapphire oscillator (500mW, 76 MHz,  $\lambda_0 = 830$  nm, 20 nm FWHM) was double-passed through an external prism line for dispersion compensation before passing through a half waveplate (HWP) and being focused by an  $f = 50$  mm achromatic lens into a  $700 \mu\text{m}$  BBO crystal angled for type-I phasematching at 830 nm. This produced horizontally polarised second harmonic pulses centered at 415 nm with a bandwidth of approximately 4 nm and an average power of around 150 mW (though this could be reduced using the HWP before the lens). The spatial chirp properties of these pulses were as illustrated in Figure 4.13. The frequency-doubled pulses were collimated with an  $f = 75$  mm fused silica ( $\text{SiO}_2$ ) lens and the remaining fundamental beam filtered out with a combination of two dichroic mirrors (highly reflecting (HR) at 415 nm and highly transmitting (HT) at 830 nm) and a

2 mm thick Schott BG39 short-wave-pass (SWP) coloured glass filter. The second harmonic power remaining after filtering, to use as the pump beam for the down-conversion, was over 100 mW. Upon moving a beam dump, an additional pair of dielectric mirrors (HR at 830 nm) placed behind the dichroic mirrors, in conjunction with a Schott BG665 long-wave-pass (LWP) glass filter, allowed the remaining fundamental beam to be used as an alignment tool. A polarising beamsplitter (PBS) was placed in this alignment beam to clean up its polarisation.

Two alignment apertures separated by 625 mm preceded a 45° incidence 50:50 beamsplitter (BS) that divided the pump beam into two. Both beams were then directed to the two downconversion crystals, the reflected beam off one steering mirror and the transmitted beam via a time delay controlled by an automated translation stage (Physik Instrumente M111.1DG) to match the arrival times of the two pulses at the crystals. The pump beams, each with a power of 40 mW, were both focused with  $f = 250$  mm  $\text{SiO}_2$  lenses into two 5 mm long KDP crystals cut for type-II phasematching placed one focal length away from the lenses. The KDP crystals were orientated with their optic axes in the horizontal plane and mounted in mirror mounts to allow fine control of the rotation angle about their vertical axes. Following the downconverters, the remaining pump light was filtered out firstly by a pair of  $\text{SiO}_2$  LWP dichroic mirrors in each arm and secondly by 2 mm thick anti-reflection (AR) coated RG665 LWP filters. Subsequently, the downconverted pairs were collimated with  $f = 150$  mm lenses.

The collimated pairs in each arm were then separated with PBSs, each preceded

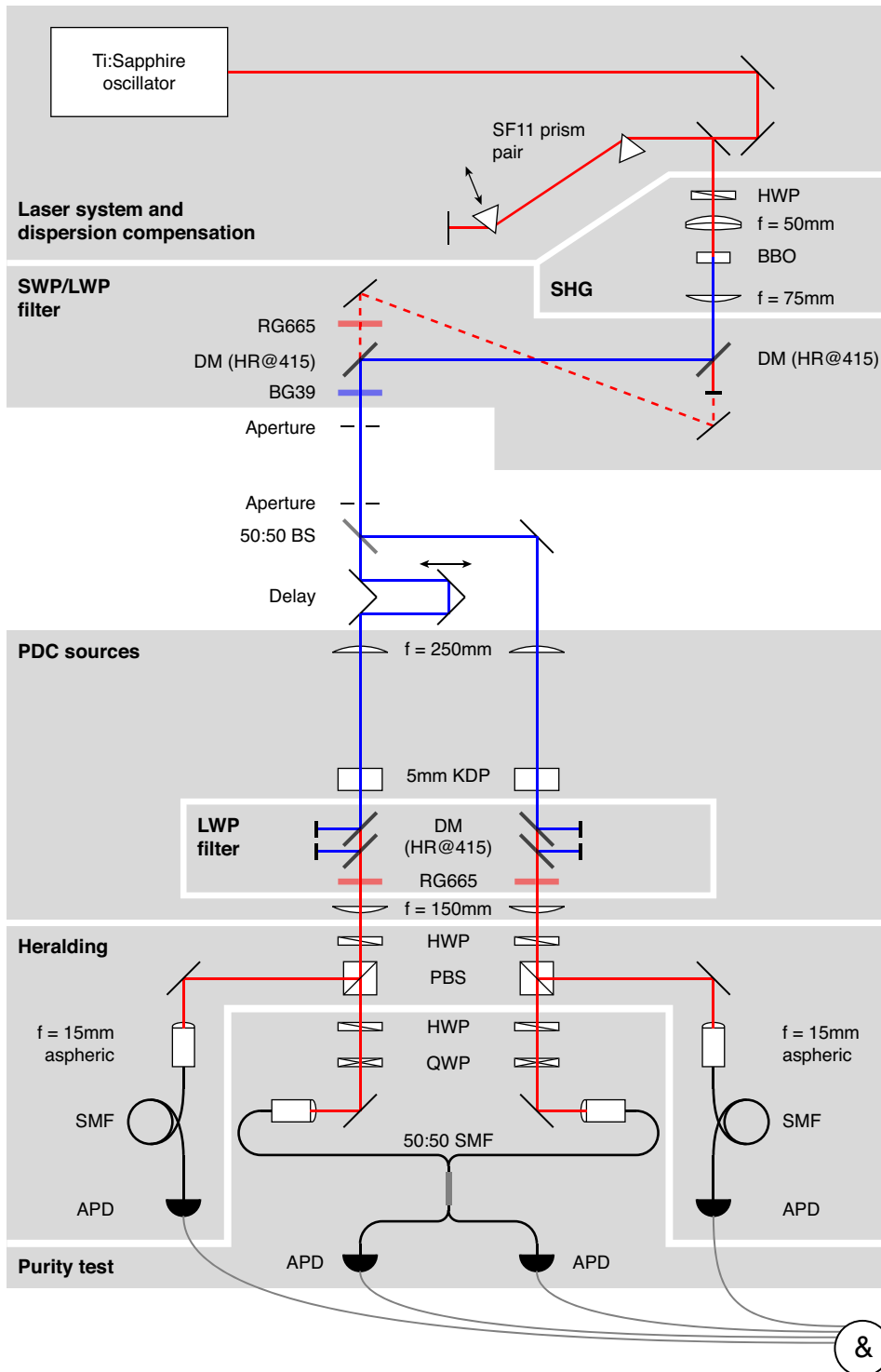


**Figure 5.4** Apparatus for two-crystal HOMI experiment. See text for details.

by a HWP. Setting the HWPs not to rotate their input polarisation led to the e-ray photons being transmitted at the PBSs and the o-rays reflected, whereas rotating the polarisation of the pairs by  $90^\circ$  gave the opposite outcome at the PBSs. The reflected beams were then each coupled into single-mode fibre (SMF) using a steering mirror, an  $f = 15$  mm aspheric lens, and Elliot Scientific single-mode 3-axis flexure stages. The other end of these fibres went directly to two Perkin-Elmer SPCM silicon avalanche photodiodes (APDs) to act as the herald detectors. Each transmitted beam from the two PBSs passed first through a HWP and then a quarter waveplate (QWP) for polarisation control and were then coupled into the two inputs of a 50:50 single-mode fibre coupler (also known as a fibre beamsplitter (FBS), in this case a Sifam FFS-830K62A11) with the same fibre coupling arrangement as for the reflected arm. The two outputs of the 50:50 FBS went to another two Si APDs, the signal detectors. This completed the optical setup.

It was crucial that all transmissive optics traversed by the SHG beam were manufactured from pure  $\text{SiO}_2$ . This material produces almost no fluorescence in response to incident light at the pump wavelength, whereas other more dispersive optical media, such as BK7 or any of the SF series of glasses, fluoresce heavily under illumination by short wavelength light. This fluorescence is of course at a longer wavelength than the pump, and hence has a high probability of passing through the LWP filters following the PDC. Therefore it has the potential to create a very high background signal of uncorrelated photons, resulting in many unwanted singles counts that reduce both the heralding efficiency and interference visibility. Addi-

tionally, these materials absorb a significant fraction of the pump beam, reducing the true coincidence count rates. It was for the same reason of fluorescence that each of the LWP glass filters following the PDC were placed after two dichroic mirrors — the dichroics remove most of the pump beam, so that the glass filters can then provide the remainder of the attenuation required at the pump wavelength while producing very little unwanted fluorescence.

The electronic TTL signals from the four APDs were split and one half sent directly to a National Instruments (NI) counting card connected to a PC to allow the single detection rates at each APD to be monitored. The other half of the signals were first inverted and attenuated before being discriminated using the single inputs of four NIM (Nuclear Instrumentation Module) OR logic gates to convert the original TTL pulses with lengths of around 40 ns to NIM signals approximately 3 ns in duration. The NIM pulses from the herald detectors passed through variable electronic time delays before arriving at two AND gates. The electronic time delays were fixed to match the arrival times of both signals input to each gate. One AND gate detected twofold coincidences between the herald and the signal detector on one side of the optical setup and the other gate monitored the twofolds between the herald and signal detector on the other side. The outputs of these two gates, one via another electronic time delay, became the inputs for a final AND gate to measure the fourfold coincidence rate. The outputs of all three AND gates went to the NI counter card via a NIM to TTL converter. As required, the resulting coincidence window for these electronics was approximately 5 ns — substantially smaller than

the 13 ns between consecutive pulses from the laser system.

The count rates of pulses arriving at the counter card were recorded by a bespoke LabView program. This was written to allow simultaneous control of the position of the optical time delay stage and hence the coincidence rates for different optical delays could be monitored over long time durations without requiring any further input from the experimentalist.

### 5.3.2 Alignment procedure

Although the optical setup was fairly complex, once aligned it would remain reasonable stable over days, if not weeks, at a time, requiring only small tweaks to keep it so. Notwithstanding this, the initial development of a consistently successful alignment procedure for setting up the optical apparatus from scratch was a significant step forward and hence warrants further discussion here.

After alignment of the SHG subassembly to generate blue pulses polarised horizontally, the HWP beforehand was then rotated so that the input polarisation of the fundamental to the SHG crystal was horizontal. This turned off the SHG process so that the horizontally polarised fundamental beam could be used for rough alignment of the downconversion crystals. The longitudinal position of the  $f = 75$  mm collimation lens following the SHG crystal was adjusted to ensure that the fundamental beam was collimated and the foci of the  $f = 250$  mm lenses were at the centres of the PDC crystals. This beam was then aligned on the two apertures before the downconverters with a power meter.

To manage properly the effects of spatial chirp, it was essential to mount both KDP crystals with their optic axes parallel and in the correct orientation with respect to the direction of the spatial chirp. Although manufacturers usually mark nonlinear crystals to indicate a plane in which the optic axis lies, in general they do not designate the direction of the axis. So it was with the KDP crystals used: here the plane of the optic axis was shown but it was still necessary to distinguish between the two possibilities for each of their directions. To this end, with the fundamental alignment beam incident on the crystals, a HWP was temporarily placed in the beam to rotate the polarisation to  $45^\circ$  and produce type-II SHG in the crystal. By placing a SWP filter and spectrometer after the crystal, the SHG spectrum was seen to shift as the crystal was rotated. In this way the orientation of the optic axes could be determined and the KDP crystals set in the correct direction to make the sign of the spatial chirp (as defined in Section 4.2) positive. Both crystals were then aligned to be at approximately normal incidence.

The split ratio of the 50:50 BS for the pump beam was specified at 415 nm and therefore at 830 nm most of the light was transmitted. However, enough was reflected to allow alignment of both crystals. The transmitted and reflected beams from both PBSs were coupled into their respective fibres, but, as the collection optics were optimized to obtain efficient coupling of the PDC into single-mode fibre, the coupling ratios were not especially high for the alignment beam. However, over 50% could still be expected.

In order to see interference between heralded single photons at a FBS, their po-

larisation has to match at the beamsplitter. However, the beams will experience arbitrary — and in general different — polarisation rotations during their passage through the two lengths of fibre leading to the interaction region. These rotations must be pre-compensated before the photons enter the fibre so that their polarisations are identical upon reaching the beamsplitter. The level of pre-compensation required was determined using the alignment beam and set with the waveplates in the transmitted arms of the PBSs. One of the outputs of the FBS was sent through another PBS and then to a power meter. The QWPs and HWPs in both arms were then rotated to minimise the power transmitted by this PBS for each input in turn. As the rotation in polarisation experienced in the output lead of the FBS was the same for both inputs, although this technique does not result in the light at the FBS being in a *known* polarisation state it does put the light from both inputs in the *same* polarisation state. This is enough to ensure good interference.

The approximate zero point of the optical time delay could then be set. The spectrum of the fundamental pulses was monitored at one of the outputs of the FBS with a spectrometer while scanning the time delay. As the delay passed through zero, fringes were observed on this spectrum, with the exact zero for the alignment pulses at the position where almost total interference occurred across the entire spectral bandwidth.

This concluded the approximate alignment performed with the fundamental beam. This was good enough to give some coincidence counts from each crystal to allow the coupling of the PDC into the fibres to be optimized. To do this, the

HWP before the SHG was rotated back to generate pulses at 415 nm, the  $f = 75$  mm lens returned to the position that gave the best collimation of this beam, and the SWP filter and beam dump replaced. With the HWPs before the PBSs set to transmit whichever set of photons were to be interfered, the twofold coincidence count rates were optimized by changing the position of the SMF tips using the flexure stages and the angle of incidence on the fibre tip with the steering mirrors before the aspheric lenses. For a pump power of about 40 mW per crystal, the measured twofold coincidence rates were around  $3000\text{ s}^{-1}$ , suggesting a true coincidence rate (without the FBS in place) of  $6000\text{ s}^{-1}$ . This resulted in a fourfold coincidence rate of approximately  $0.3\text{ s}^{-1}$  after the FBS, commensurate with the measured twofold rates and laser repetition frequency.

### 5.3.3 Mode matching and marginal spectra

We know from previous chapters that the modes of two photons that are to be interfered must be identical spatially, spectrally, temporally, and in polarisation to ensure indistinguishability and yield a high-visibility dip. The main advantage of a FBS over a free-space plate or cube BS is that, upon arrival at the interaction region, both photons are in well-defined single spatial modes and hence are automatically almost perfectly matched in that degree of freedom. The pre-compensation of both photons by the waveplates before the input fibres resulted in the highest level of polarisation indistinguishability that one could hope for at the FBS, and the temporal distinguishability was adjusted by the delay stage.

As no spectral filtering was used, it was vital to control precisely the spectral mode overlap of the photons sent to the FBS directly from the point of production through the parameters of the sources themselves. As described in Chapter 4 the overlap of the o-ray and, more crucially, the e-ray spectra is therefore controlled simply by the phasematching angles of the crystals. Due to the high sensitivity of the e-ray wavelength to the phasematching angle, it is the e-ray spectrum that requires the most care to fully mode match. With both crystals set to be near to normal incidence, the two e-ray spectra should be at least partially overlapped, but this is not good enough to see the highest visibilities as the spectra will usually still be offset by a significant fraction of their bandwidth. Two techniques can be used to maximise the spectral overlap.

The first is to make a direct measurement of both e-ray spectral distributions. This is the simplest method but it depends on the availability of a good grating spectrometer and high-sensitivity CCD camera. For this measurement the same fibre-coupled Andor Shamrock spectrometer from the joint spectral measurements was used in conjunction with an Andor iXon electron-multiplying CCD camera. Turning up the gain on the camera to its maximum setting and operating with the 1501/mm grating allowed the marginal spectra of both the e-ray and o-ray downconversion from each crystal to be measured. First the e-ray spectrum from one crystal was recorded and then the spectrum from the second was displayed and matched to the first by observing in real time the movement of the spectrum as the crystal angle was changed about its vertical axis. Through this technique, the

two spectra could be overlapped to a high degree of accuracy (within 0.1 nm or so) simply by eye. The final spectra from both crystals were then saved to be used in calculating the degree of spectral overlap in Equation 5.24.

The second technique is to observe an interference effect that can be seen in the twofold detection rates. With the HWPs before the PBSs set to rotate the polarisation of the e- and o-rays to  $\pm 45^\circ$ , there was a 25% chance that both photons from each pair would be transmitted towards the FBS. By reconfiguring the electronics to look for twofold coincidences between the outputs of the FBS (without heralding), the interference between the amplitude for creation of a pair in one crystal and creation of a pair in the other was observed as the time delay was scanned through zero. This interference between two possible (unheralded) paths involved the detection of only two photons, and therefore required only one pair to be generated per pump pulse (rather than two pairs in the case of the full HOMI interference). Hence the data could be monitored at each time delay setting for only a short time interval (0.5s) while still registering a significant number of counts.

The interference pattern created in this configuration can be calculated with a similar approach to that used to find the full four-photon HOMI dip. This time the state consists of a superposition of a pair created in one crystal or a pair in the other with equal probability:

$$\begin{aligned}
 |\Psi_2\rangle = & \frac{1}{\sqrt{2}} \int_0^\infty d\omega_{e1} \int_0^\infty d\omega_{o1} f_1(\omega_{e1}, \omega_{o1}) \hat{a}_{e1}^\dagger(\omega_{e1}) \hat{a}_{o1}^\dagger(\omega_{o1}) |0\rangle \\
 & + \frac{1}{\sqrt{2}} \int_0^\infty d\omega_{e2} \int_0^\infty d\omega_{o2} f_2(\omega_{e2}, \omega_{o2}) \hat{a}_{e2}^\dagger(\omega_{e2}) \hat{a}_{o2}^\dagger(\omega_{o2}) |0\rangle.
 \end{aligned} \tag{5.26}$$

We now look for twofold coincidences at the two signal detectors following the beam-splitter. The projection operator for a twofold detection measurement at times  $t_{s1}$  and  $t_{s2}$  is similar to the fourfold case:

$$\hat{\Pi}_{2C}(t_{s1}, t_{s2}) = \hat{E}_{s1}^{(-)}(t_{s1})\hat{E}_{s2}^{(-)}(t_{s2})|0\rangle\langle 0|\hat{E}_{s2}^{(+)}(t_{s2})\hat{E}_{s1}^{(+)}(t_{s1}), \quad (5.27)$$

but now a photon originating in either polarisation mode (e-ray or o-ray) could reach either detector. Hence the field operators must be summed over both polarisation modes

$$\hat{E}_{s1}^{(+)}(t_{s1}) = \frac{1}{\sqrt{4}} \sum_{\mu=e,o} \int_0^\infty d\omega_{s1} [\hat{a}_{\mu 1}(\omega_{s1})e^{-i\omega_{s1}\tau} + \hat{a}_{\mu 2}(\omega_{s1})] e^{-i\omega_{s1}t_{s1}} \quad (5.28)$$

$$\hat{E}_{s2}^{(+)}(t_{s2}) = \frac{1}{\sqrt{4}} \sum_{\mu=e,o} \int_0^\infty d\omega_{s2} [\hat{a}_{\mu 1}(\omega_{s2})e^{-i\omega_{s2}\tau} - \hat{a}_{\mu 2}(\omega_{s2})] e^{-i\omega_{s2}t_{s2}}, \quad (5.29)$$

where  $\mu = e, o$  represent the two polarisation modes emitted by each crystal. The probability of a twofold detection event occurring at times  $t_{s1}$  and  $t_{s2}$  is calculated in a similar manner to Equation 5.7 and the probability of obtaining a coincidence can be found by integrating this over the detection times to give the result

$$P_{2C}(\tau) = \frac{1}{4} \int_0^\infty \int_0^\infty d\omega_{s1} d\omega_{s2} |f_2(\omega_{s1}, \omega_{s2}) + f_2(\omega_{s2}, \omega_{s1}) - [f_1(\omega_{s1}, \omega_{s2}) + f_1(\omega_{s2}, \omega_{s1})] e^{-i(\omega_{s1} + \omega_{s2})\tau}|^2. \quad (5.30)$$

In order to interpret this result, consider first the condition for unit visibility,

$P_{2C}(0) = 0$ , requiring that

$$f_1(\omega_{s1}, \omega_{s2}) + f_1(\omega_{s2}, \omega_{s1}) = f_2(\omega_{s1}, \omega_{s2}) + f_2(\omega_{s2}, \omega_{s1}) \quad (5.31)$$

$$\Rightarrow f_1(\omega_{s1}, \omega_{s2}) = f_2(\omega_{s1}, \omega_{s2}) \quad (5.32)$$

This equality makes no demands on the factorability of the joint spectral amplitude function from each crystal, only that they are identical to one another. Therefore this interference effect provides a perfect method of matching the spectral modes from the two crystals.

Secondly, as the separability of the joint amplitude does not matter here, the form of the interference effect can be studied most simply by calculating  $P_{2C}(\tau)$  for two factorable but distinguishable pairs with Gaussian amplitudes. In this case, the joint spectral amplitude from crystal 1 is of the form

$$f_1(\omega_{e1}, \omega_{o2}) = g_{e1}(\omega_{e1})g_{o1}(\omega_{o1}), \quad (5.33)$$

and similarly for crystal 2, where the functions  $g_{e1}(\omega_{e1})$  are defined in Equation 5.13. Plots of the interference pattern for different central frequencies and overlaps of the photons in each pair are shown in Figure 5.5. The parameters were chosen to model the situation encountered for KDP. It is interesting to note that the width of the narrow central area is dependent on the spectral bandwidth of the spectrally broad o-ray photons, yet the overall visibility (essentially the visibility of these central fringes) depends mainly on the overlap of the narrowband e-ray photons.

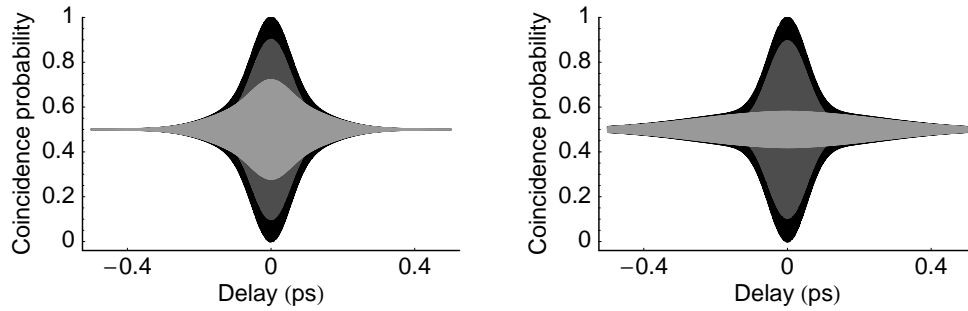


**Figure 5.5** Theoretical plots of the twofold coincidence interference between the amplitudes for creation of a pair in one crystal or the other. Left: photon bandwidths are  $\text{FWHM}_{\lambda_e} = 3.5 \text{ nm}$ ,  $\text{FWHM}_{\lambda_o} = 16.5 \text{ nm}$ ; mean wavelength mismatches are 0 nm (black,  $V = 1$ ), 10 nm in the o-rays (dark grey,  $V = 0.80$ ), 5 nm in the e-rays (light grey,  $V = 0.44$ ). Right: FWHM photon bandwidths are  $\text{FWHM}_{\lambda_e} = 1.75 \text{ nm}$ ,  $\text{FWHM}_{\lambda_o} = 16.5 \text{ nm}$ ; mean wavelength mismatches are 0 nm (black,  $V = 1$ ), 10 nm between the o-rays (dark grey,  $V = 0.79$ ), 5 nm between the e-rays (light grey,  $V = 0.16$ ).

Real-time observation of this twofold interference effect allowed one crystal angle to be adjusted to maximise the interference visibility and once this optimization had taken place, the spectra from the two crystals were maximally overlapped. Note that the changes in angle required were fractions of a degree and hence the adjustments to the crystal angle made little difference to the delay. The necessary range of angles could therefore be accessed without changing the zero point of the delay noticeably. Data showing this interference effect are displayed in Figure 5.6. An additional benefit of the observation of this secondary interference was to check the time delay zero point.

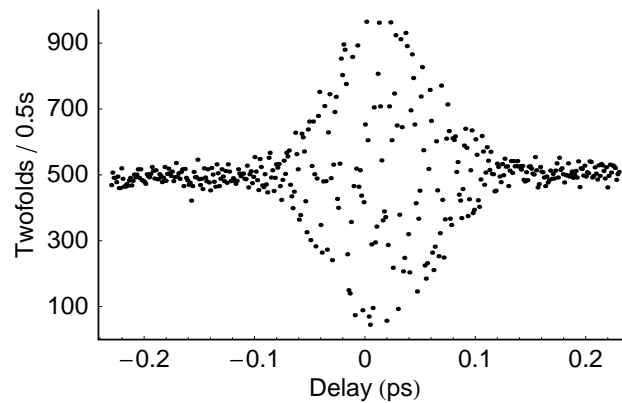


**Figure 5.6** Twofold coincidence data for the alignment interference between the amplitudes for creation of a pair in one crystal or the other.

### 5.3.4 Interference of e-ray photons

First the interference of the two e-ray photons was studied by setting the HWPs to transmit these at the PBSs. The fourfold count rates we recorded for periods of 900 s at a series of 13 equidistant delay stage positions over a range of about  $200 \mu\text{m}$ , corresponding to a total delay range of approximately 1.5 ps. The twofold rates from each crystal were also recorded for periods of 1 s at the same delay settings.

The resulting data are displayed in Figure 5.7. The fourfold coincidence data were fitted with a Gaussian dip function with four free parameters: the value for large delay, the visibility, the width, and the position of the zero delay point. The HOMI dip for the heralded e-ray photons from independent sources recorded without any spectral filters was thus found to have a visibility of  $V = 0.944 \pm 0.016$  (standard error on the fit) and a FWHM of 440 fs. The measured visibility agrees remarkably well with the value of 0.95 calculated from the numerical model in Chapter 4. The

temporal width of the dip corresponds to a coherence time of 310 fs, commensurate with the measured spectral bandwidth of the e-ray photons — a pulse at 830 nm with 3.5 nm of bandwidth would have a coherence time of 290 fs.

The central wavelengths of the fits to the two e-ray spectra (shown in Figure 5.8) were measured to differ by just over 0.1 nm, corresponding to approximately 2% of their FWHM bandwidths. Calculating the overlap of these two fits as in Equation 5.24, the value of the maximum possible visibility was found to be  $V_{\max} = 0.981$ . Using the measured visibility,  $V_{\text{expt}} = 0.944$ , the minimum purity of the e-ray photons is  $\mathcal{P}_{\min} = 0.962$ , proving that the heralded photons were prepared in states of exceptionally high purity. Additionally, this figure is in good agreement with the measurement made on the joint spectral intensity distribution and suggests that the joint spectral amplitude has little phase across it.

### 5.3.5 Interference of o-ray photons

Secondly, the two o-ray photons were interfered by rotating the polarisation before the PBSs by  $90^\circ$ . The fourfold coincidences were again recorded for 900 s per point, but this time for 15 points over a smaller range of delays ( $70 \mu\text{m}$ , corresponding to 400 fs) to account for the greater spectral bandwidth of the o-ray photons.

The data are displayed in Figure 5.9, with the fourfold coincidences again fitted with a Gaussian dip function. The visibility of the HOMI dip for the o-ray photons was  $V = 0.891 \pm 0.030$  with a FWHM width of 92 fs. This width gives a coherence time of approximately 65 fs, also consistent with the broad measured

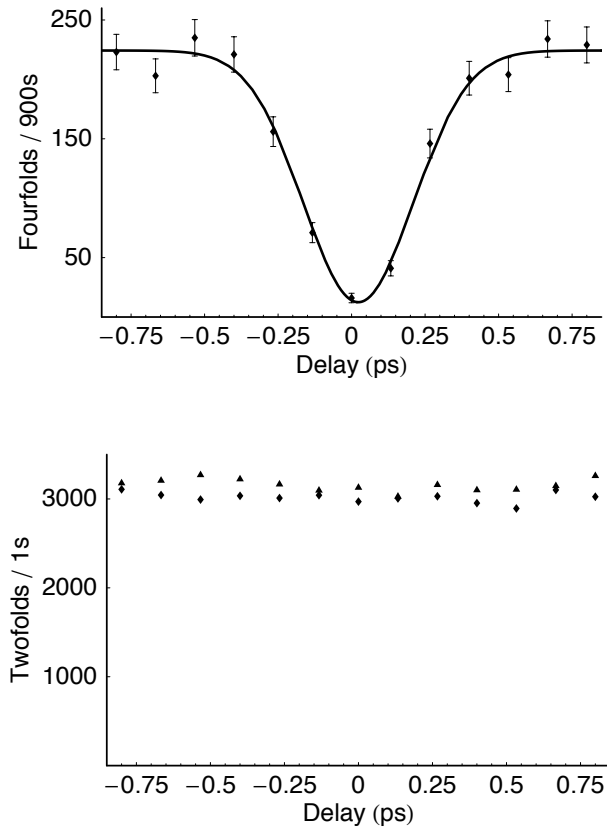


**Figure 5.7** Interference of the unfiltered heralded e-ray photons. Top: Fourfold coincidence data for e-ray HOMI dip, displaying  $V = 0.944 \pm 0.016$ . Bottom: Constant twofold coincidence rates. The error bars, simply from Poissonian counting statistics, are equal to the square root of the number of counts at each point.

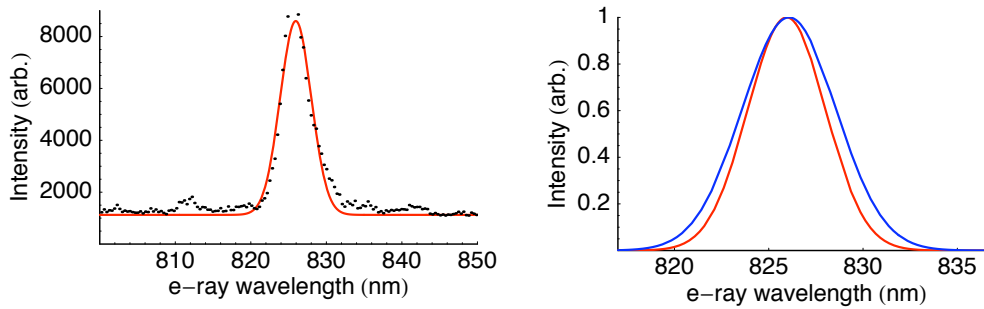


**Figure 5.8** Spectral overlap of two e-ray photons. Left: Data for marginal distribution of e-ray photons from crystal 1 as measured with the Andor spectrometer and camera along with Gaussian fit. Right: Comparison of normalised fits to both e-ray spectra. Centres differ by just over 0.1 nm and FWHM bandwidths by approximately 1 nm. The common spectrum in both plots is red.

spectral bandwidth (16.5 nm bandwidth suggests a coherence time of 62 fs). As there is little phase on the joint spectrum, shown by the high interference visibility, the time-bandwidth product of these photons should be almost Fourier transform limited, and their temporal duration will therefore only be slightly longer than their coherence time.

## 5.4 Heralding efficiency

The heralding efficiency of a source measured with perfect detectors was defined in Equation 3.28 as the ratio of the rate of coincidence counts in both arms to that of singles in the trigger arm. However, in any experimental situation the quantum efficiency of the detectors will inevitably be less than one, and hence sometimes a coincidence event will not be registered when the signal photon reaches its detector

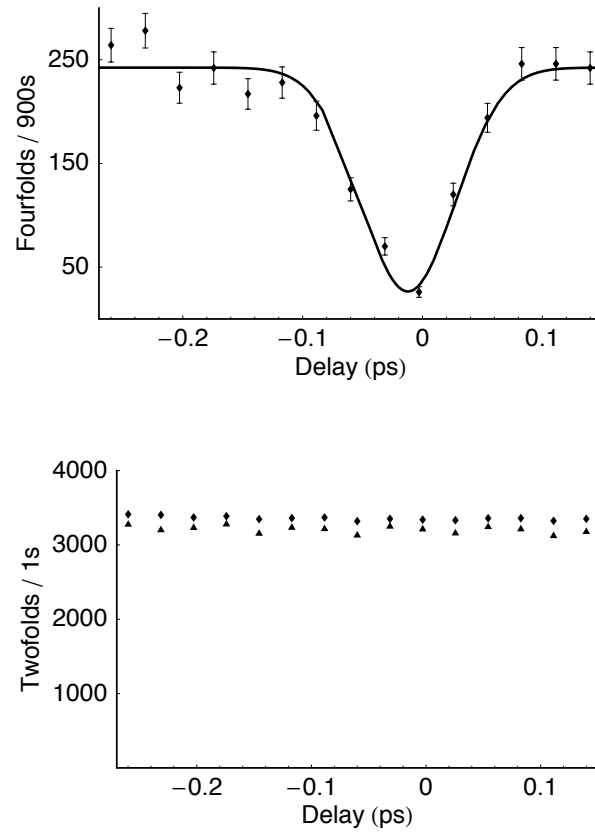


**Figure 5.9** Interference of the unfiltered heralded o-ray photons. Top: Fourfold coincidence data for e-ray HOMI dip, displaying  $V = 0.891 \pm 0.030$ . Note much narrower temporal width than for the e-ray interference. Bottom: Constant twofold coincidence rates. The error bars represent Poissonian counting statistics.

after a trigger event. This artificially reduces the measured ratio of coincidences to singles, which is then known as the detection efficiency. The relation of the detection efficiency,  $\eta_D$ , to the heralding efficiency,  $\eta_H$ , is through the quantum efficiency of the detector in the signal arm,  $\eta_q$ :

$$\eta_H = \eta_q \eta_D = \eta_q \frac{R_C}{R_T}. \quad (5.34)$$

Knowledge of  $\eta_q$  therefore allows an estimate to be made of the heralding efficiency of a source in the presence of imperfect detectors. During the data runs for the interference dips presented in the previous sections the typical detection efficiency was around 6.5%. However, in this case we must also take into account that the presence of the FBS in the signal arm reduced the number of coincidence events to half the value that would have been measured were the FBS replaced with a single length of fibre. The true detection efficiency at which the system was performing could then be inferred as twice the measured efficiency, or about 13%.

However, when using the e-ray photons as heralds the asymmetry of the joint spectral distribution can be exploited to increase the heralding efficiency of the source by careful spectral filtering. By placing in the e-ray arm only a high-transmission filter whose bandwidth just exceeds that of the e-ray photons (around 4 nm), many of the background counts (most of which come from the fundamental titanium:sapphire beam that has a bandwidth around five times that of the e-ray photons) can be cut out without affecting the e-ray PDC photons. Therefore the

singles rate in the herald arm can be reduced dramatically while not changing the form of the two-photon state or discarding any PDC photons.

To test this proposal, a spectral filter with a bandwidth of 3 nm (slightly narrower than the ideal, but the only suitable filter available) and peak transmission well over 95% at 830 nm was placed in the e-ray arm of one of the downconversion sources configured to use the e-rays as heralds. The filter was angle tuned to set its central transmission wavelength to maximise the twofold coincidence rate from the source. In this way the detection efficiency was measured to be over 13% with the FBS in place, giving a true detection efficiency of 26.3%. Furthermore, taking into account the quantum efficiency of the APD in the signal arm (about 60% at this wavelength), the source heralding efficiency can be estimated at almost 44%. Although higher heralding efficiencies have been measured from spectrally correlated PDC sources (notably from a pulsed waveguided source<sup>93</sup> and a pulsed type-I bulk crystal source<sup>94</sup> and a CW-pumped periodically-poled crystal<sup>96</sup>), this is still very high for a pulsed bulk PDC source.

## Chapter 6

# Conclusion

*The test of all knowledge is experiment. Experiment is the sole judge of scientific “truth.”*

R. P. Feynman<sup>157</sup>

Despite the ubiquitous usage of parametric downconversion in quantum optics laboratories during the last twenty years, it was only recently that the potential benefits resulting from the ability to control the spectral emission properties of downconversion sources became apparent. It was first demonstrated theoretically by Grice *et al*<sup>102</sup> that the technique of spectral engineering was a promising route towards high-performance heralded single photon sources. The possibility of generating photon pairs in factorable states from a variety of nonlinear crystals through the use of an ultrafast pump laser suggested that single photons could be prepared directly in pure quantum states and hence the lossy spectral filters that had been widely used to date could be discarded. The work contained in this thesis has built

on the foundations of these previous studies and vindicated the concept of factorable state generation by successfully demonstrating the interference of pure single photons from two such engineered sources.

## 6.1 Summary

Chapter 1 introduced the concept of a photon and the difference between pure states and mixed states. The properties of an ideal single photon source were outlined and then a general introduction to single photon sources, including parametric downconversion, was given. The principle of phasematching in a birefringent nonlinear crystal was described along with how it gives rise to correlations in the pairs emitted by a downconversion source. The phenomenon of Hong-Ou-Mandel interference between two pure and indistinguishable single photons at a beamsplitter was calculated.

The second chapter gave some more details of the nonlinear properties of  $\chi^{(2)}$  crystals that can lead to photon pair generation through phasematched interactions in which the oscillations of every emitter in the ensemble remain in phase with the pump field. The spectral dependence of the two-photon state created in PDC was derived from the interaction Hamiltonian, and during this calculation the mathematical origins of the energy and momentum phasematching conditions became clear. Subsequently, the mechanics of phasematching in a birefringent medium were studied in more depth, firstly by considering a toy model of a two-dimensional type-I interaction and how dispersion and birefringence affect the emission structure, and secondly through the picture of a type-II process in both the collinear and

noncollinear regimes. The re-expression of the collinear two-photon joint spectral amplitude as the product of the pump function with the phasematching function was emphasized and the effects of these upon the joint state was examined in the case of both type-I and type-II BBO.

Engineering a factorable two-photon state in the ideal collinear case was the subject of Chapter 3. First it was shown that pure single photons are required for high-visibility interference and then, through the reduced density operators for individual heralded photons, that factorable states are needed to prepare pure single photons directly from the source. The Schmidt decomposition was introduced as a means of quantifying the degree of correlation in a bipartite state, and hence the purity of heralded photons from a PDC source. As the Schmidt decomposition can only be found analytically for a small class of states, the singular value decomposition was presented as a numerical method of determining the Schmidt number of any arbitrary state. The detrimental effects of the most common method of removing correlations from photon pairs — spectral filtering — were examined upon the available pair generation rate and heralding efficiency of a typical type-II BBO downconverter. It was demonstrated that there is a direct tradeoff between these two parameters and the purity that one could reasonably expect given that no source engineering has been carried out. The method of factorable state generation based on group velocity matching between the pump and either the average velocity of the daughter photons or the velocity of just one of them was outlined through the exponential approximation to the phasematching function. Factorabil-

ity was demonstrated to first order in both the spectral and temporal domains with a truncated expansion of the wavevector mismatch. The analytic Schmidt decompositions of the resulting approximate states were calculated in BBO and KDP for the symmetric and asymmetric group velocity matching cases respectively.

Chapter 4 took the idea of group velocity matching, previously shown to give factorability in the approximate two-photon states, and applied this concept to a more realistic experimental situation. The effects on the joint spectrum of focusing a spatially chirped pump beam into a downconversion crystal and then collecting the PDC output into single-mode fibres were considered by calculating the exact state for variations of the relevant angles. A method of modelling numerically the joint state by enforcing phasematching in two dimensions and summing the resulting amplitudes over a range of input and output angles was shown. Measurements of both the pump and collection angles along with the pump spatial frequency distribution were made for the source in question and through inputting these figures to the numerical model the expected joint spectral intensity could be plotted. Using two fibre-coupled grating monochromators, a direct measurement of the joint intensity was made and compared to the predictions of the model. It was shown that the agreement between the two was very good and that factorable states could indeed be generated under the correct conditions. The degree of second order coherence of the source was measured to be almost zero demonstrating that the source produced true single photons.

The penultimate chapter initially proved that the method for verifying the single

photon purity, Hong–Ou–Mandel interference between the heralded emission from independent sources, also provides a direct measurement of the factorability of the two-photon states generated. However, to make an accurate estimate of the purity, the inevitable presence of a small spectral mode mismatch between the heralded photons required a means of distinguishing between this reduction in visibility and that resulting from impurity in the individual photons. A detailed description of the downconversion sources followed, along with the apparatus needed to measure the interference effect. A reliable method of aligning the sources was presented, including two techniques that enable the spectral distributions of the photons to be matched as accurately as possible. The data for the interference of both the e-ray photons and the o-ray photons were shown, demonstrating that both were highly pure without the need for any spectral filters. Finally, the heralding efficiency of the source was optimized by exploiting the form of the joint spectrum through the use of a filter in the heralding arm that did not affect the photon pairs but cut out many of the background singles counts. The resulting efficiency was exceptionally high for a pulsed PDC source in a bulk medium.

## 6.2 Outlook

### 6.2.1 Future work with the KDP sources

The experimental demonstration of pure single photon preparation directly from the spectrally engineered KDP crystals without any narrowband filtering is impor-

tant in the context of downconversion as a viable source of photons for real-world QIP applications. The next stage is to perform some proof-of-principle experiments showing that worthwhile operations can be carried out with the output from these sources. Two such experiments are described in this section.

### Heralded NOON states

In order to move beyond probabilistic quantum tasks whose successful outcomes must be post-selected on a particular pattern of detection events, one must have the ability to reliably create nonclassical states with unit probability. If this could be achieved, rather than waiting until the correct state happens to enter the apparatus, the quantum state required to perform the given information processing or measurement task can be input with certainty on every shot. This approach is, unlike the post-selected one, scalable to large devices requiring many operations.

As an example we consider quantum-enhanced phase measurement. Through the application of nonclassical states of light, the precision with which one can estimate the relative phase  $\varphi$  between the arms of an interferometer can be higher for a given level of resource use than would ever be possible with classical light<sup>158</sup>. In the ideal situation, for a resource of  $N$  photons, the classical uncertainty in the measurement scales as  $\Delta\varphi \propto 1/\sqrt{N}$ , whereas for the optimal quantum input<sup>159</sup> the uncertainty improves at a rate of  $\Delta\varphi \propto 1/N$ . In a lossless optical system the quantum state that gives the largest enhancement of this precision is a so-called NOON state — a

superposition of  $N$  photons in one arm and none in the other or vice versa:

$$|\psi_{\text{NOON}}\rangle = \frac{1}{\sqrt{2}} (|N_a, 0_b\rangle + |0_a, N_b\rangle). \quad (6.1)$$

Precision phase measurements using similar states formed from the output of PDC sources have been demonstrated<sup>160,161</sup> but all were based on post-selected measurements. Hence the effective resources used for a single NOON state measurement were significantly greater than  $N$  photons as many of the photons that passed through the interferometer were subsequently discarded and did not contribute to the measurement outcome.

This problem of post-selection could be mitigated if one could generate an entangled state that was conditioned on the detection of heralding photons before the measurement apparatus<sup>162</sup>. In this case, one would know for sure when the correct state had been prepared, and only then send it through the interferometer. To date, heralded entanglement generation has not been demonstrated in the laboratory. However, if we consider the quantum state in the two output arms of the 50:50 fibre coupler in the HOMI experiment presented in Chapter 5, at zero time delay we find

$$|\psi_{\text{out}}\rangle \approx \frac{1}{\sqrt{2}} (|2_a, 0_b\rangle + |0_a, 2_b\rangle), \quad (6.2)$$

This is clearly a two-photon NOON state that has already been conditioned on the arrival of two photons at the heralding detectors. Due to the ability of the KDP sources to produce high-purity photons without any spectral filtering, these heralded

NOON states can potentially be produced with high efficiency.

The next experiment that will be performed with the KDP sources is a demonstration of heralded NOON state preparation. The scheme is to combine at a polarising beamsplitter the two fibre coupler output modes into two polarisation modes in a single spatial mode, hence creating a polarisation-encoded NOON state. A variable relative phase can then be introduced between the two polarisation modes with a birefringent element, and the second interference performed by rotating both polarisations by  $45^\circ$  and mixing them at a polarising beamsplitter. By monitoring the coincidence counts between the two output modes of the final beamsplitter as a function of the phase  $\varphi$ , interference fringes that oscillate at  $\cos(2\varphi)$  should be observed. As long as the visibility of the fringes is sufficient then the precision with which the phase measurement can be made is greater than would be possible classically with the same resources, as in the classical case the fringes would only vary at  $\cos\varphi$ . This experiment is currently under way and some preliminary data demonstrating the  $2\varphi$  fringes have been recorded.

### **Continuous variable entanglement distillation**

Information can be encoded not only in the discrete degrees of freedom of a quantum entity (such as polarisation or number in the case of photons) but also in the continuous degrees of freedom, for example position or momentum. Encoding on these continuous variables (CVs) allows more information to be carried by a single photon than would be possible in the discrete case. Typically for optical CV encoding, the

electric field itself is used as the variable through the field quadrature amplitudes  $\hat{X}$  and  $\hat{P}$ , analogous to the position and momentum operators.

Having prepared a system entangled in these field quadratures, upon distribution across any realistic quantum network the inevitable effects of loss and decoherence will be to reduce the entanglement between the elements of the system, eventually to the point at which no entanglement remains<sup>163</sup>. In a fibre-based network operating at telecommunications wavelengths, this will occur after transmission over a distance of about 100 km. Therefore any protocol for long-distance distribution of entanglement must include repeater substations between the sender and the receiver where the entanglement can be restored to its initial level before being sent on towards the destination. These “signal-boosting” intermediaries rely on a process known as *entanglement distillation*<sup>164</sup> — through performing certain operations on a subset of the elements (and thereby destroying them) one can increase the entanglement between the remainder. Techniques for entanglement distillation of quantum states whose description in phase space is initially Gaussian in form require<sup>165</sup> operations that are capable of “de-Gaussification” of the states, for example by removing a single photon<sup>166,167</sup>. Entanglement distillation has been demonstrated in discrete variables<sup>168,169</sup> and the increase of entanglement shown through de-Gaussification of quadrature-entangled beams<sup>170</sup>.

A method of entanglement distillation between photons from two pairs has been designed using photon subtraction from each pair and subsequent interference of the remaining modes at two beamsplitters, based on proposals by Browne *et al*<sup>171</sup> and

Eisert *et al*<sup>172</sup>. This scheme is dependent on the pairs initially being in factorable states to give high-visibility interference at the beamsplitters, and hence the KDP downconversion sources are ideal for its implementation. A second pair of KDP sources has now been built with a view to accomplishing this goal. Additionally, the recent implementation of a time-multiplexed photon-number-resolving detector<sup>173</sup> should enable more efficient detection of the increased entanglement than would otherwise be possible with binary APDs.

### 6.2.2 Factorable state generation in other media

The experiments contained in this thesis have demonstrated that factorable state generation by group velocity matching is feasible in a bulk second-order nonlinear crystal. However, using such a medium has inherent drawbacks, principally that the spatial emission pattern is not naturally single mode and hence efficient coupling of the pairs into single-mode fibre can be difficult. Other disadvantages are that the interaction length between the pump and the crystal is generally limited to a few millimetres or a couple of centimetres at most, and with a limited range of crystals available, factorable state generation is only possible at certain wavelengths. Therefore, to fulfil certain requirements one may need to consider other pair generation systems that do not suffer from the same difficulties and whether the technique of group velocity matching could be generalised to these media.

### Factorable states from fibre

Spontaneous pair generation by four-wave mixing in fibre has the twin benefits of an almost unlimited interaction length between the pump and the medium (this can compensate for the very small third-order nonlinearity), and pairs that are automatically guided in a well-defined (usually single) spatial mode. Each set of modes are subject to energy and momentum phasematching conditions similar to those for PDC, so the pairs generated are in general highly spectrally correlated. Due to the inverse dependence of the width of the phasematching function on the length of the medium, the joint amplitude is especially narrow in the case of long fibres so extremely tight filters would be required to eliminate these spectral correlations.

Nonetheless, very recently it has been shown theoretically<sup>174</sup> that by satisfying group velocity matching conditions between the pump and generated photons, factorable pair generation is possible in fibre. The criteria that must be fulfilled are very similar to those for downconversion — the group velocities can be matched either symmetrically or asymmetrically, resulting in states that have similar or very different photon bandwidths respectively. As the photon pair frequencies straddle the pump frequency, group velocity matching can be achieved in any fibre, but in a typical fibre the frequency at which it occurs may not lie within an advantageous range.

The use of microstructured photonic crystal fibre (PCF) consisting of a small solid silica core surrounded by a matrix of air-filled spaces separated by silica filaments allows the properties of the fibre to be engineered. The modal dispersion can

be set through the control of two parameters: the core diameter (typically around  $2\ \mu\text{m}$ ) and the ratio of air to silica in the surrounding cladding, known as the fill fraction (anything from 30% to 95% air). Adjustments to these two parameters change the two wavelengths at which zero group velocity dispersion (GVD) occurs and hence the points where the phasematching curves will intersect the zeros of group velocity mismatch. For PCF without birefringence, the pairs are generated co-polarised with the pump and these crossing points are far from the pump wavelength — therefore the photons are not within the efficient range of silicon APDs. Indeed, this has to be the case for pair generation, as the output of the fibre must be dispersed spectrally to split the pairs from the pump and close to the pump wavelength there will be overwhelming uncorrelated background from Raman scattering of the pump. On the other hand, with a birefringent PCF, the pairs are polarised perpendicular to the pump, making their separation from the pump more straightforward, and the group velocity matching condition can be satisfied with both close enough to the pump to be easily detectable with silicon APDs.

The ability to construct the nonlinear material with exactly the desired properties is a great advantage of PCF. However, only a limited variety of PCFs are available off-the-shelf, and to draw fibre to a custom specification is expensive. Therefore, one must find among the standard designs a PCF with characteristics that match as closely as possible those required for factorable state generation. An experimental demonstration of pure single photon generation from a fibre source is now being worked on.

### Factorable states from waveguide sources

Downconversion can also take place in an optical waveguide that is written into a plain or patterned nonlinear crystal and will channel the pairs in a single optical mode. This process will inevitably have a similar interaction length to that in a bulk crystal, as it is simply limited by the size of the crystal that can be manufactured. Although this is much shorter than a typical fibre, it is compensated for by the relative strength of the second-order coupling in nonlinear crystals compared to that of the third-order in fibres, so pair generation rates could be made similar to those possible from fibre sources. The spatial confinement of the pairs in two dimensions has allowed the observation of raw heralding efficiencies over 50% from a waveguide written in quasi-phasematched periodically-poled KTP<sup>93</sup>.

The potential of PDC in waveguides for building high-efficiency, user-friendly heralded single photon sources is clear, but restricting the interaction region to a single dimension does nothing to reduce the spectral correlations within each pair. Therefore, similarly to standard bulk sources, the generation of pure-state single photons is not in general possible from waveguided sources. However, a recent proposal by Raymer *et al*<sup>175</sup> suggested that by constructing a cavity around the waveguide, one could accomplish factorable state generation.

By placing a downconverter in a high-finesse cavity that contains the daughter fields, emission can be restricted to a set of discrete cavity modes. Hence the effect on the joint spectrum is to set up a regularly-spaced grid of probability amplitudes where the allowed signal and idler longitudinal cavity modes intersect<sup>97</sup>.

For a macroscopic cavity consisting of dichroic mirrors placed before and after a nonlinear crystal, these modes are closely spaced in frequency. Inevitably many will fall under the downconversion phasematching function and pump envelope, whereas for factorable state generation, we require that only one joint cavity mode will be picked out by the phasematching and pump functions. For this to be the case, the cavity must be very small (around 0.1 mm in length) and the resulting frequency modes widely spaced. Such a microcavity can be fashioned around a waveguide by longitudinally microstructuring either end of the waveguide itself. A periodic modulation in the refractive index of the waveguide can form a distributed Bragg reflector (DBR) that will reflect only the daughter fields and allow the pump to pass. In this way a short cavity, designed such that only a single joint cavity mode is within the phasematching function, can be built directly into the waveguide chip. The primary excitation of only one joint cavity mode provides a high degree of factorability, but it is almost inevitable that other modes will overlap to a small degree with the phasematching and pump functions. These side modes can be made relatively far from the desired mode and can easily be removed by filtering outside the cavity with negligible decrease in expected count rates.

Constructing microcavities within a waveguide in a nonlinear medium presents a significant technical challenge<sup>176</sup> and is not possible with current fabrication techniques. Hopefully though, new waveguide writing technology and microstructuring methods will enable preliminary devices to be realised in the next few years.

### **Integrated single chip source and processing**

The potential for creating a source of factorable pairs in a single spatial mode along with the ability to write ever-more complex waveguide-based components into a variety of media<sup>177,178</sup> herald the prospect of an integrated device that would be capable of both generating pairs and performing processing tasks. A network of UV-written beamsplitters and phase shifters on an optical chip could implement photonic quantum logic operations on photons either generated in waveguides on the same chip or delivered by fibres pigtailed onto the inputs of the device. Additional fibres could be joined to the outputs to take the photons to either fibre-based photon-number-resolving detectors or ordinary binary APDs. In this way, one can envisage a compact and robust photonic QIP system built from a network of these devices that would be capable of complex information-processing protocols. The demonstration of heralded pure-state photon preparation contained in this thesis is an important step along the road towards engineering such a device.



# Appendix A

## A recipe for purity

Hopefully having read this thesis you will have a good idea of what is required to build a parametric downconversion source capable of preparing pure heralded single photons. However, for those readers who are in a hurry, here follows a summary of the salient considerations that the experimentalist must bear in mind to obtain a high-visibility HOMI dip without spectral filtering. They are organised approximately in order from laser to detection electronics.

1. Ensure that the fundamental beam is approximately transform limited before second harmonic generation. If necessary use a prism line to compensate for any quadratic phase.
2. Use a negative uniaxial crystal for frequency doubling. This restricts the spatial chirp in the second harmonic beam to be in the same plane as the output (e) polarisation and the optic axis.

3. Fully characterise the SHG beam. Measure the spatial chirp along both transverse directions (though if you have followed point 2 there should be no chirp orthogonal to the polarisation of the beam) and the beam diameter.
4. Do not use any heavy glass transmissive optics (e.g. any SF-series glass, BK7, etc.) between the frequency doubler and the long-wave-pass filters following the downconverters. This applies to any downconversion experiment and ensures that there is as little unwanted fluorescence as possible.
5. Unless you really know what you are doing, do not pump both crystals using the whole pump beam with the downconversion from the first crystal split off with a dichroic mirror. Divide the pump before the crystals to ensure the same focusing conditions in each crystal.
6. Build the setup as symmetrically as possible. Put the delay before the crystals not after so that everything downstream of the lenses preceding the downconverters is identical between the two sides.
7. Make sure that you know not only the plane in which the optic axis of each crystal resides but also the direction that it points in. This is important to get the spatial chirp direction correct. Check this by performing SHG in each crystal and observing with a spectrometer the direction in which the spectrum moves as the crystal is rotated. Do not rely on any markings on the crystal made by the manufacturer to tell you the direction of the optic axis — this will probably indicate the plane of the axis but not the direction. Even if a

pair of crystals are marked in the same way, do not assume that their axes point in the same direction relative to the marking, they may well not.

8. Do a numerical calculation to make sure that the focusing parameters, spatial chirp, and fibre mode collection angle match up to give a factorable state. Check the optic axes are in the correct orientation to give the right direction of spatial chirp.
9. Do not rotate the polarisation of the pump beam between the SHG and the downconverters. In this way the spatial chirp will be in the same plane as the incident polarisation and optic axes of the KDP and one only needs to consider phasematching in two dimensions rather than three.
10. Use a 50:50 fibre coupler rather than a free-space beamsplitter. This will make your life much easier.
11. Do not worry too much about having a 50:50 coupler split ratio that is exactly 50:50. The visibility is only weakly dependent on this — assuming it is better than about 45:55 it will do. Do not trust the singles count rates to give you a good estimate of the split ratio. Fibre 50:50 couplers are highly wavelength dependent so any background counts that are not at the central frequency will not experience the same split ratio, possibly leading to higher singles rates in one arm than the other when using only one input.
12. Match the polarisations arriving at the 50:50 coupler, then do not touch the fibres on the inputs.

13. Optimise the fibre coupling, then leave it alone.
14. Make sure that your time delay zero point is set correctly. The zero for down-conversion may not be in exactly the same place as that for the alignment pulses.
15. Ensure that both crystals are at exactly the same angle, especially if interfering the e-ray photons. Initially set this by eye with the back reflection from the front faces. If there is a single-photon sensitive spectrometer available, use it to match the two spectra. Check the alignment interference and tweak the angle of one of the crystals to maximise the visibility. This also serves as a check on the time delay zero.
16. Check that the coincidence electronics are working properly.
17. If all else fails, measure the joint spectra from both crystals. If the state is not factorable, think about why this might be.

# Bibliography

- [1] T. H. Maiman, *Stimulated Optical Radiation in Ruby*, *Nature*, **187**, pp. 493–494 (1960).
- [2] C. H. Townes, *How the Laser Happened: Adventures of a Scientist*, OUP (1999).
- [3] J. S. Bell, *On the Einstein Podolsky Rosen Paradox*, *Physics*, **1**, pp. 195–200 (1964).
- [4] S. J. Freedman and J. F. Clauser, *Experimental Test of Local Hidden-Variable Theories*, *Physical Review Letters*, **28** (1972).
- [5] E. S. Fry and R. C. Thompson, *Experimental Test of Local Hidden-Variable Theories*, *Physical Review Letters*, **37** (1976).
- [6] A. Aspect, P. Grangier, and G. Roger, *Experimental Tests of Realistic Local Theories via Bell's Theorem*, *Physical Review Letters*, **47**, pp. 460–463 (1981).
- [7] A. Aspect, J. Dalibard, and G. Roger, *Experimental Test of Bell's Inequalities Using Time-Varying Analyzers*, *Physical Review Letters*, **49**, pp. 1804–1807 (1982).
- [8] A. Aspect, P. Grangier, and G. Roger, *Experimental Realization of Einstein-Podolsky-Rosen-Bohm Gedankenexperiment: A New Violation of Bell's Inequalities*, *Physical Review Letters*, **49**, pp. 91–94 (1982).
- [9] Z. Y. Ou and L. Mandel, *Violation of Bell's Inequality and Classical Probability in a Two-Photon Correlation Experiment*, *Physical Review Letters*, **61** (1988).
- [10] K. B. Davis, M. O. Mewes, M. R. Andrews, N. J. van Druten, D. S. Durfee, D. M. Kurn, and W. Ketterle, *Bose-Einstein Condensation in a Gas of Sodium Atoms*, *Physical Review Letters*, **75**, pp. 3969–3973 (1995).
- [11] D. Bouwmeester, A. Ekert, and A. Zeilinger, *The Physics of Quantum Information: Quantum Cryptography, Quantum Teleportation, Quantum Computation*, Springer (2001).

- 
- [12] E. Knill, R. Laflamme, and G. J. Milburn, *A scheme for efficient quantum computation with linear optics*, *Nature*, **409**, pp. 46–52 (2001).
- [13] D. E. Browne and T. Rudolph, *Resource-Efficient Linear Optical Quantum Computation*, *Physical Review Letters*, **95**, 010501 (2005).
- [14] C. K. Hong, Z. Y. Ou, and L. Mandel, *Measurement of Subpicosecond Time Intervals between Two Photons by Interference*, *Physical Review Letters*, **59**, pp. 2044–2046 (1987).
- [15] P. P. Rohde and T. C. Ralph, *Frequency and temporal effects in linear optical quantum computing*, *Physical Review A*, **71**, 032320 (2005).
- [16] L. Mandel, *Quantum effects in one-photon and two-photon interference*, *Reviews of Modern Physics*, **71**, pp. 274–282 (1999).
- [17] C. Roychoudhuri and R. Roy, *The nature of light: what is a photon?*, *Optics and Photonics News* October 2003, p. S1 (2003).
- [18] W. E. Lamb and M. O. Scully, *The Photoelectric Effect Without Photons*, in S. F. de Physique (editor), *Polarization: Matiere et Rayonnement*, Presses Universitaires de France, Paris (1969).
- [19] J. F. Clauser, *Experimental distinction between the quantum and classical field-theoretic predictions for the photoelectric effect*, *Phys. Rev. D*, **9**, pp. 853–860 (1974).
- [20] G. N. Lewis, *Nature*, **118**, pp. 874–875 (1926).
- [21] A. Zajonc, *Light reconsidered*, *Optics and Photonics News* October 2003, pp. S2–S5 (2003).
- [22] A. Muthukrishnan, M. O. Scully, and M. Suhail Zubairy, *The concept of the photon — revisited*, *Optics and Photonics News* October 2003, pp. S18–S27 (2003).
- [23] R. Loudon, *The Quantum Theory of Light*, OUP, third edition (2000).
- [24] R. Glauber, *The Quantum Theory of Optical Coherence*, *Physical Review*, **130**, pp. 2529–2539 (1963).
- [25] M. A. Nielsen and I. L. Chuang, *Quantum Computation and Quantum Information*, Cambridge University Press, Cambridge (2000).
- [26] H. J. Kimble, M. Dagenais, and L. Mandel, *Photon Antibunching in Resonance Fluorescence*, *Physical Review Letters*, **39**, pp. 691–695 (1977).
- [27] B. Lounis and M. Orrit, *Single-photon sources*, *Reports on Progress in Physics*, **68**, pp. 1129–1179 (2005).

- [28] M. Oxborrow and A. Sinclair, *Single-photon sources*, Contemporary Physics, **46**, pp. 173–206 (2005).
- [29] J. Beugnon, M. P. A. Jones, J. Dingjan, B. Darquié, G. Messin, A. Browaeys, and P. Grangier, *Quantum interference between two single photons emitted by independently trapped atoms*, Nature, **440**, pp. 779–782 (2006).
- [30] A. D. Boozer, A. Boca, R. Miller, T. E. Northup, and H. J. Kimble, *Reversible State Transfer between Light and a Single Trapped Atom*, Physical Review Letters, **98**, p. 193601 (2007).
- [31] A. Kuhn, M. Hennrich, and G. Rempe, *Deterministic Single-Photon Source for Distributed Quantum Networking*, Physical Review Letters, **89**, p. 067901 (2002).
- [32] J. McKeever, A. Boca, A. D. Boozer, R. Miller, J. R. Buck, A. Kuzmich, and H. J. Kimble, *Deterministic Generation of Single Photons from One Atom Trapped in a Cavity*, Science, **303**, pp. 1992–1994 (2004).
- [33] M. Hijlkema, B. Weber, H. P. Specht, S. C. Webster, A. Kuhn, and G. Rempe, *A single-photon server with just one atom*, Nature Physics, **3**, pp. 253–255 (2007).
- [34] P. Maunz, D. L. Moehring, S. Olmschenk, K. C. Younge, D. N. Matsukevich, and C. Monroe, *Quantum interference of photon pairs from two remote trapped atomic ions*, Nature Physics, **3**, pp. 538–541 (2007).
- [35] D. L. Moehring, P. Maunz, S. Olmschenk, K. C. Younge, D. N. Matsukevich, L. M. Duan, and C. Monroe, *Entanglement of single-atom quantum bits at a distance*, Nature, **449**, pp. 68–71 (2007).
- [36] P. Michler, A. Kiraz, C. Becher, W. V. Schoenfeld, P. M. Petroff, L. Zhang, E. Hu, and A. Imamoglu, *A Quantum Dot Single-Photon Turnstile Device*, Science, **290**, pp. 2282–2285 (2000).
- [37] K. Hennessy, A. Badolato, M. Winger, D. Gerace, M. Atature, S. Gulde, S. Falt, E. L. Hu, and A. Imamoglu, *Quantum nature of a strongly coupled single quantum dot-cavity system*, Nature, **445**, pp. 896–899 (2007).
- [38] N. Akopian, N. H. Lindner, E. Poem, Y. Berlatzky, J. Avron, D. Gershoni, B. D. Gerardot, and P. M. Petroff, *Entangled Photon Pairs from Semiconductor Quantum Dots*, Physical Review Letters, **96**, 130501 (2006).
- [39] A. Kiraz, M. Atature, and A. Imamoglu, *Quantum-dot single-photon sources: Prospects for applications in linear optics quantum-information processing*, Physical Review A, **69**, 032305 (2004).

- [40] C. Santori, D. Fattal, J. Vuckovic, G. S. Solomon, and Y. Yamamoto, *Indistinguishable photons from a single-photon device*, *Nature*, **419**, pp. 594–597 (2002).
- [41] R. Brouri, A. Beveratos, J. P. Poizat, and P. Grangier, *Photon antibunching in the fluorescence of individual color centers in diamond*, *Optics Letters*, **25**, pp. 1294–1296 (2000).
- [42] C. Kurtsiefer, S. Mayer, P. Zarda, and H. Weinfurter, *Stable Solid-State Source of Single Photons*, *Physical Review Letters*, **85** (2000).
- [43] A. Beveratos, R. Brouri, T. Gacoin, A. Villing, J. Poizat, and P. Grangier, *Single Photon Quantum Cryptography*, *Physical Review Letters*, **89**, p. 187901 (2002).
- [44] V. Jacques, E. Wu, F. Grosshans, F. Treussart, P. Grangier, A. Aspect, and J.-F. Roch, *Experimental Realization of Wheeler’s Delayed-Choice Gedanken Experiment*, *Science*, **315**, pp. 966–968 (2007).
- [45] T. Chaneliere, D. N. Matsukevich, S. D. Jenkins, S.-Y. Lan, R. Zhao, T. A. B. Kennedy, and A. Kuzmich, *Quantum Interference of Electromagnetic Fields from Remote Quantum Memories*, *Physical Review Letters*, **98**, 113602 (2007).
- [46] Z.-S. Yuan, Y.-A. Chen, S. Chen, B. Zhao, M. Koch, T. Strassel, Y. Zhao, G.-J. Zhu, J. Schmiedmayer, and J.-W. Pan, *Synchronized Independent Narrow-Band Single Photons and Efficient Generation of Photonic Entanglement*, *Physical Review Letters*, **98**, 180503 (2007).
- [47] C. W. Chou, S. V. Polyakov, A. Kuzmich, and H. J. Kimble, *Single-Photon Generation from Stored Excitation in an Atomic Ensemble*, *Physical Review Letters*, **92**, 213601 (2004).
- [48] D. Felinto, C. W. Chou, J. Laurat, E. W. Schomburg, H. de Riedmatten, and H. J. Kimble, *Conditional control of the quantum states of remote atomic memories for quantum networking*, *Nature Physics*, **2**, pp. 844–848 (2006).
- [49] J. K. Thompson, J. Simon, H. Loh, and V. Vuletic, *A High-Brightness Source of Narrowband, Identical-Photon Pairs*, *Science*, **313**, pp. 74–77 (2006).
- [50] J. Wen, S. Du, and M. H. Rubin, *Biphoton generation in a two-level atomic ensemble*, *Physical Review A*, **75**, 033809 (2007).
- [51] B. Julsgaard, J. Sherson, J. I. Cirac, J. Fiurasek, and E. S. Polzik, *Experimental demonstration of quantum memory for light*, *Nature*, **432**, pp. 482–486 (2004).
- [52] C. W. Chou, H. de Riedmatten, D. Felinto, S. V. Polyakov, S. J. van Enk, and H. J. Kimble, *Measurement-induced entanglement for excitation stored in remote atomic ensembles*, *Nature*, **438**, pp. 828–832 (2005).

- [53] J. Nunn, I. A. Walmsley, M. G. Raymer, K. Surmacz, F. C. Waldermann, Z. Wang, and D. Jaksch, *Mapping broadband single-photon wave packets into an atomic memory*, Physical Review A, **75**, 011401 (2007).
- [54] J. F. Sherson, H. Krauter, R. K. Olsson, B. Julsgaard, K. Hammerer, I. Cirac, and E. S. Polzik, *Quantum teleportation between light and matter*, Nature, **443**, pp. 557–560 (2006).
- [55] C.-W. Chou, J. Laurat, H. Deng, K. S. Choi, H. de Riedmatten, D. Felinto, and H. J. Kimble, *Functional Quantum Nodes for Entanglement Distribution over Scalable Quantum Networks*, Science, **316**, pp. 1316–1320 (2007).
- [56] J. Sharping, J. Chen, X. Li, P. Kumar, and R. Windeler, *Quantum-correlated twin photons from microstructure fiber*, Optics Express, **12**, pp. 3086–3094 (2004).
- [57] X. Li, J. Chen, P. Voss, J. Sharping, and P. Kumar, *All-fiber photon-pair source for quantum communications: Improved generation of correlated photons*, Optics Express, **12**, pp. 3737–3744 (2004).
- [58] J. Rarity, J. Fulconis, J. Duligall, W. Wadsworth, and P. Russell, *Photonic crystal fiber source of correlated photon pairs*, Optics Express, **13**, pp. 534–544 (2005).
- [59] J. Fulconis, O. Alibart, W. Wadsworth, P. Russell, and J. Rarity, *High brightness single mode source of correlated photon pairs using a photonic crystal fiber*, Optics Express, **13**, pp. 7572–7582 (2005).
- [60] O. Alibart, J. Fulconis, G. K. L. Wong, S. G. Murdoch, W. J. Wadsworth, and J. G. Rarity, *Photon pair generation using four-wave mixing in a microstructured fibre: theory versus experiment*, New J. Phys, **8**, pp. 67–86 (2006).
- [61] Q. Lin, F. Yaman, and G. P. Agrawal, *Photon-pair generation in optical fibers through four-wave mixing: Role of Raman scattering and pump polarization*, Physical Review A, **75**, 023803 (2007).
- [62] D. Burnham and D. Weinberg, *Observation of Simultaneity in Parametric Production of Optical Photon Pairs*, Physical Review Letters, **25**, pp. 84–87 (1970).
- [63] E. J. Galvez, C. H. Holbrow, M. J. Pysher, J. W. Martin, N. Courtemanche, L. Heilig, and J. Spencer, *Interference with correlated photons: Five quantum mechanics experiments for undergraduates*, American Journal of Physics, **73**, pp. 127–140 (2005).
- [64] S. Friberg, C. K. Hong, and L. Mandel, *Measurement of Time Delays in the Parametric Production of Photon Pairs*, Physical Review Letters, **54**, pp. 2011–2013 (1985).

- [65] C. K. Hong and L. Mandel, *Theory of parametric frequency down conversion of light*, Physical Review A, **31**, pp. 2409–2418 (1985).
- [66] P. A. Franken, A. E. Hill, C. W. Peters, and G. Weinreich, *Generation of Optical Harmonics*, Physical Review Letters, **7**, pp. 118–119 (1961).
- [67] P. A. Franken and J. F. Ward, *Optical Harmonics and Nonlinear Phenomena*, Reviews of Modern Physics, **35**, pp. 23–39 (1963).
- [68] A. Lamas-Linares, J. C. Howell, and D. Bouwmeester, *Stimulated emission of polarization-entangled photons*, Nature, **412**, pp. 887–890 (2001).
- [69] D. H. Johnston, *Otterbein Online Symmetry Tutorial - Inversion Symmetry*, <http://symmetry.otterbein.edu/jmol/inversion.html>.
- [70] R. Boyd, *Nonlinear Optics*, Academic Press, second edition (2003).
- [71] J. E. Midwinter and J. Warner, *The effects of phase matching method and of uniaxial crystal symmetry on the polar distribution of second-order non-linear optical polarization*, British Journal of Applied Physics, **16**, pp. 1135–1142 (1965).
- [72] J. A. Giordmaine, *Mixing of Light Beams in Crystals*, Physical Review Letters, **8**, pp. 19–20 (1962).
- [73] P. D. Maker, R. W. Terhune, M. Nisenoff, and C. M. Savage, *Effects of Dispersion and Focusing on the Production of Optical Harmonics*, Physical Review Letters, **8**, pp. 21–22 (1962).
- [74] V. G. Dmitriev, G. G. Gurzadyan, and D. N. Nikogosyan, *Handbook of Non-linear Optical Crystals*, Springer-Verlag, Berlin (1991).
- [75] M. H. Rubin, *Transverse correlation in optical spontaneous parametric down-conversion*, Physical Review A, **54**, pp. 5349–5360 (1996).
- [76] A. Migdall, *Polarization directions of noncollinear phase-matched optical parametric downconversion output*, Journal of the Optical Society of America B: Optical Physics, **14**, pp. 1093–1098 (1997).
- [77] C. Kurtsiefer, M. Oberparleiter, and H. Weinfurter, *Generation of correlated photon pairs in type-II parametric down conversion—revisited*, Journal of Modern Optics, **48**, pp. 1997–2007 (2001).
- [78] T. B. Pittman, D. V. Strekalov, D. N. Klyshko, M. H. Rubin, A. V. Sergienko, and Y. H. Shih, *Two-photon geometric optics*, Physical Review A, **53**, pp. 2804–2815 (1996).
- [79] W. P. Grice and I. A. Walmsley, *Spectral information and distinguishability in type-II down-conversion with a broadband pump*, Physical Review A, **56**, pp. 1627–1634 (1997).

- [80] H. d. Riedmatten, I. Marcikic, W. Tittel, H. Zbinden, and N. Gisin, *Quantum interference with photon pairs created in spatially separated sources*, Physical Review A, **67**, p. 022301 (2003).
- [81] R. Kaltenbaek, B. Blauensteiner, M. Zukowski, M. Aspelmeyer, and A. Zeilinger, *Experimental Interference of Independent Photons*, Physical Review Letters, **96**, 240502 (2006).
- [82] C.-Y. Lu, X.-Q. Zhou, O. Guhne, W.-B. Gao, J. Zhang, Z.-S. Yuan, A. Goebel, T. Yang, and J.-W. Pan, *Experimental entanglement of six photons in graph states*, Nature Physics, **3**, pp. 91–95 (2007).
- [83] J. Fulconis, O. Alibart, W. J. Wadsworth, and J. G. Rarity, *Quantum interference with photon pairs using two micro-structured fibres*, arXiv:quant-ph/0701129v1 (2007).
- [84] E. Brambilla, A. Gatti, M. Bache, and L. A. Lugiato, *Simultaneous near-field and far-field spatial quantum correlations in the high-gain regime of parametric down-conversion*, Physical Review A, **69**, 023802 (2004).
- [85] M. Atatüre, G. Di Giuseppe, M. D. Shaw, A. V. Sergienko, B. E. A. Saleh, and M. C. Teich, *Multiparameter entanglement in femtosecond parametric down-conversion*, Physical Review A, **65**, p. 023808 (2002).
- [86] G. J. Milburn, *Quantum optical Fredkin gate*, Physical Review Letters, **62**, pp. 2124–2127 (1989).
- [87] T. C. Ralph, *Quantum optical systems for the implementation of quantum information processing*, Reports on Progress in Physics, **69**, pp. 853–898 (2006).
- [88] P. Kok, W. J. Munro, K. Nemoto, T. C. Ralph, J. P. Dowling, and G. J. Milburn, *Linear optical quantum computing with photonic qubits*, Reviews of Modern Physics, **79**, 135 (2007).
- [89] K. J. Resch, K. L. Pagnell, R. Prevedel, A. Gilchrist, G. J. Pryde, J. L. O’Brien, and A. G. White, *Time-Reversal and Super-Resolving Phase Measurements*, Physical Review Letters, **98**, 223601 (2007).
- [90] B. P. Lanyon, T. J. Weinhold, N. K. Langford, M. Barbieri, D. F. V. James, A. Gilchrist, and A. G. White, *Experimental demonstration of Shor’s algorithm with quantum entanglement*, arXiv:0705.1398v1 (2007).
- [91] P. G. Kwiat, K. Mattle, H. Weinfurter, A. Zeilinger, A. V. Sergienko, and Y. Shih, *New High-Intensity Source of Polarization-Entangled Photon Pairs*, Phys. Rev. Lett., **75**, pp. 4337–4341 (1995).
- [92] C. Kurtsiefer, M. Oberparleiter, and H. Weinfurter, *High-efficiency entangled photon pair collection in type-II parametric fluorescence*, Physical Review A, **64**, p. 023802 (2001).

- [93] A. B. U'Ren, C. Silberhorn, K. Banaszek, and I. A. Walmsley, *Efficient Conditional Preparation of High-Fidelity Single Photon States for Fiber-Optic Quantum Networks*, Physical Review Letters, **93**, pp. 093601–4 (2004).
- [94] T. B. Pittman, B. C. Jacobs, and J. D. Franson, *Heralding single photons from pulsed parametric down-conversion*, Optics Communications, **246**, pp. 545–550 (2005).
- [95] S. Chen, Y.-A. C., T. Strassel, Z.-S. Yuan, B. Zhao, J. Schmiedmayer, and J.-W. Pan, *Deterministic and Storable Single-Photon Source Based on a Quantum Memory*, Physical Review Letters, **97**, 173004 (2006).
- [96] A. Fedrizzi, T. Herbst, T. Jennewein, and A. Zeilinger, *A fiber-coupled wavelength tunable source of narrowband entangled photons*, arXiv:0706.2877 (2007).
- [97] J. S. Neergaard-Nielsen, B. M. Nielsen, H. Takahashi, A. I. Vistnes, and E. S. Polzik, *High purity bright single photon source*, Opt. Express, **15**, pp. 7940–7949 (2007).
- [98] J. Fulconis, O. Alibart, J. L. O'Brien, W. J. Wadsworth, and J. G. Rarity, *Non-classical Interference and Entanglement Generation Using a Photonic Crystal Fiber Pair Photon Source*, Physical Review Letters, **99**, 120501 (2007).
- [99] M. Halder, A. Beveratos, N. Gisin, V. Scarani, C. Simon, and H. Zbinden, *Entangling independent photons by time measurement*, Nat Phys, **3**, pp. 692–695 (2007).
- [100] M. H. Rubin, D. N. Klyshko, Y. H. Shih, and A. V. Sergienko, *Theory of two-photon entanglement in type-II optical parametric down-conversion*, Physical Review A, **50**, pp. 5122–5133 (1994).
- [101] A. B. U'Ren, *Multi-Photon State Engineering for Quantum Information Processing Applications*, Ph.D. thesis, University of Rochester (2004).
- [102] W. P. Grice, A. B. U'Ren, and I. A. Walmsley, *Eliminating frequency and space-time correlations in multiphoton states*, Physical Review A, **64**, p. 063815 (2001).
- [103] S. J. van Enk and H. J. Kimble, *Comment on “Quantum state transfer between matter and light”*, Science, **306**, pp. 663–6 (2005).
- [104] C. K. Law, I. A. Walmsley, and J. H. Eberly, *Continuous Frequency Entanglement: Effective Finite Hilbert Space and Entropy Control*, Physical Review Letters, **84**, pp. 5304–5307 (2000).
- [105] K. W. Chan, C. K. Law, and J. H. Eberly, *Quantum entanglement in photon-atom scattering*, Physical Review A, **68** (2003).

- [106] R. Grobe, K. Rzazewski, and J. Eberly, *Measure of electron-electron correlation in atomic physics*, Journal of Physics B: Atomic, Molecular, and Optical Physics, **27**, pp. L503–L508 (1994).
- [107] J. H. Eberly, *Schmidt Analysis of Pure-State Entanglement*, Laser Physics, **16**, pp. 921–926 (2006).
- [108] L. Lamata and J. Leon, *Dealing with entanglement of continuous variables: Schmidt decomposition with discrete sets of orthogonal functions*, Journal of Optics B: Quantum and Semiclassical Optics, **7**, pp. 224–229 (2005).
- [109] J.-W. Pan, D. Bouwmeester, M. Daniell, H. Weinfurter, and A. Zeilinger, *Experimental test of quantum nonlocality in three-photon Greenberger-Horne-Zeilinger entanglement*, Nature, **403**, pp. 515–519 (2000).
- [110] J. F. Hodelin, G. Khoury, and D. Bouwmeester, *Optimal generation of pulsed entangled photon pairs*, Physical Review A, **74**, 013802 (2006).
- [111] H. S. Poh, C. Y. Lum, I. Marcikic, A. Lamas-Linares, and C. Kurtsiefer, *Joint spectrum mapping of polarization entanglement in spontaneous parametric down-conversion*, Physical Review A, **75**, 043816 (2007).
- [112] P. G. Kwiat, E. Waks, A. G. White, I. Appelbaum, and P. H. Eberhard, *Ultrabright source of polarization-entangled photons*, Physical Review A, **60**, pp. R773–R776 (1999).
- [113] N. A. Peters, J. B. Altepeter, D. Branning, E. R. Jeffrey, T.-C. Wei, and P. G. Kwiat, *Maximally Entangled Mixed States: Creation and Concentration*, Physical Review Letters, **92**, 133601 (2004).
- [114] J. Altepeter, E. Jeffrey, and P. Kwiat, *Phase-compensated ultra-bright source of entangled photons*, Optics Express, **13**, pp. 8951–8959 (2005).
- [115] W. Tittel, J. Brendel, B. Gisin, T. Herzog, H. Zbinden, and N. Gisin, *Experimental demonstration of quantum correlations over more than 10 km*, Physical Review A, **57**, pp. 3229–3232 (1998).
- [116] W. Tittel, J. Brendel, H. Zbinden, and N. Gisin, *Quantum Cryptography Using Entangled Photons in Energy-Time Bell States*, Physical Review Letters, **84**, pp. 4737–4740 (2000).
- [117] M. P. Almeida, S. P. Walborn, and P. H. S. Ribeiro, *Experimental investigation of quantum key distribution with position and momentum of photon pairs*, Physical Review A, **72**, 022313 (2005).
- [118] I. Ali-Khan, C. J. Broadbent, and J. C. Howell, *Large-Alphabet Quantum Key Distribution Using Energy-Time Entangled Bipartite States*, Physical Review Letters, **98**, 060503 (2007).

- [119] D. Bouwmeester, J.-W. Pan, K. Mattle, M. Eibl, H. Weinfurter, and A. Zeilinger, *Experimental quantum teleportation*, *Nature*, **390**, pp. 575–579 (1997).
- [120] R. Ursin, T. Jennewein, M. Aspelmeyer, R. Kaltenbaek, M. Lindenthal, P. Walther, and A. Zeilinger, *Quantum teleportation across the Danube*, *Nature*, **430**, pp. 849–849 (2004).
- [121] Q. Zhang, A. Goebel, C. Wagenknecht, Y.-A. Chen, B. Zhao, T. Yang, A. Mair, J. Schmiedmayer, and J.-W. Pan, *Experimental quantum teleportation of a two-qubit composite system*, *Nature Physics*, **2**, pp. 678–682 (2006).
- [122] Z. Zhao, Y.-A. Chen, A.-N. Zhang, T. Yang, H. J. Briegel, and J.-W. Pan, *Experimental demonstration of five-photon entanglement and open-destination teleportation*, *Nature*, **430**, pp. 54–58 (2004).
- [123] T. Aichele, A. I. Lvovsky, and S. Schiller, *Optical mode characterization of single photons prepared by means of conditional measurements on a biphoton state*, *The European Physical Journal D-Atomic, Molecular and Optical Physics*, **18**, pp. 237–245 (2002).
- [124] P. P. Rohde, W. Mauerer, and C. Silberhorn, *Spectral structure and decompositions of optical states, and their applications*, *New Journal of Physics*, **9**, p. 91 (2007).
- [125] D. Klyshko, *Photons and Nonlinear Optics*, Gordon and Breach New York (1988).
- [126] J. L. O’Brien, G. J. Pryde, A. G. White, T. C. Ralph, and D. Branning, *Demonstration of an all-optical quantum controlled-NOT gate*, *Nature*, **426**, pp. 264–267 (2003).
- [127] R. Prevedel, P. Walther, F. Tiefenbacher, P. Bohi, R. Kaltenbaek, T. Jennewein, and A. Zeilinger, *High-speed linear optics quantum computing using active feed-forward*, *Nature*, **445**, pp. 65–69 (2007).
- [128] M. S. Tame, R. Prevedel, M. Paternostro, P. Bohi, M. S. Kim, and A. Zeilinger, *Experimental Realization of Deutsch’s Algorithm in a One-Way Quantum Computer*, *Physical Review Letters*, **98**, 140501 (2007).
- [129] M. Eibl, S. Gaertner, M. Bourennane, C. Kurtsiefer, M. Żukowski, and H. Weinfurter, *Experimental Observation of Four-Photon Entanglement from Parametric Down-Conversion*, *Physical Review Letters*, **90**, p. 200403 (2003).
- [130] T. Yang, Q. Zhang, T.-Y. Chen, S. Lu, J. Yin, J.-W. Pan, Z.-Y. Wei, J.-R. Tian, and J. Zhang, *Experimental Synchronization of Independent Entangled Photon Sources*, *Physical Review Letters*, **96**, 110501 (2006).

- [131] A. Ourjoumtsev, R. Tualle-Brouri, J. Laurat, and P. Grangier, *Generating Optical Schrodinger Kittens for Quantum Information Processing*, Science, **312**, pp. 83–86 (2006).
- [132] A. Ourjoumtsev, H. Jeong, R. Tualle-Brouri, and P. Grangier, *Generation of optical “Schrodinger cats” from photon number states*, Nature, **448**, pp. 784–786 (2007).
- [133] J. P. Torres, M. W. Mitchell, and M. Hendrych, *Indistinguishability of entangled photons generated with achromatic phase matching*, Physical Review A, **71**, 022320 (2005).
- [134] J. P. Torres, F. Macià, S. Carrasco, and L. Torner, *Engineering the frequency correlations of entangled two-photon states by achromatic phase matching*, Optics Letters, **30**, pp. 314–316 (2005).
- [135] M. Hendrych, M. Micuda, and J. P. Torres, *Tunable control of the bandwidth and frequency correlations of entangled photons*, arXiv:quant-ph/0612135 (2006).
- [136] S. Carrasco, J. P. Torres, L. Torner, A. Sergienko, B. E. A. Saleh, and M. C. Teich, *Spatial-to-spectral mapping in spontaneous parametric down-conversion*, Physical Review A, **70**, 043817 (2004).
- [137] S. Carrasco, A. V. Sergienko, B. E. A. Saleh, M. C. Teich, J. P. Torres, and L. Torner, *Spectral engineering of entangled two-photon states*, Physical Review A, **73**, 063802 (2006).
- [138] Z. D. Walton, M. C. Booth, A. V. Sergienko, B. E. A. Saleh, and M. C. Teich, *Controllable frequency entanglement via auto-phase-matched spontaneous parametric down-conversion*, Physical Review A, **67**, p. 053810 (2003).
- [139] Z. D. Walton, A. V. Sergienko, B. E. A. Saleh, and M. C. Teich, *Generation of polarization-entangled photon pairs with arbitrary joint spectrum*, Physical Review A, **70**, 052317 (2004).
- [140] G. Molina-Terriza, S. Minardi, Y. Deyanova, C. I. Osorio, M. Hendrych, and J. P. Torres, *Control of the shape of the spatial mode function of photons generated in noncollinear spontaneous parametric down-conversion*, Physical Review A, **72**, 065802 (2005).
- [141] J. P. Torres, A. Alexandrescu, S. Carrasco, and L. Torner, *Quasi-phase-matching engineering for spatial control of entangled two-photon states*, Optics Letters, **29**, pp. 376–378 (2004).
- [142] A. B. U’Ren, K. Banaszek, and I. A. Walmsley, *Photon engineering for quantum information processing*, arXiv:quant-ph/0305192v1 (2003).

- [143] A. B. U'Ren, C. Silberhorn, K. Banaszek, I. A. Walmsley, R. Erdmann, W. P. Grice, and M. G. Raymer, *Generation of pure-state single-photon wavepackets by conditional preparation based on spontaneous parametric downconversion*, *Laser Physics*, **15**, pp. 146–161 (2005).
- [144] A. B. U'Ren, R. K. Erdmann, M. de la Cruz-Gutierrez, and I. A. Walmsley, *Generation of Two-Photon States with an Arbitrary Degree of Entanglement Via Nonlinear Crystal Superlattices*, *Physical Review Letters*, **97**, pp. 223602–4 (2006).
- [145] A. B. U'Ren, E. Murkamel, K. Banaszek, and I. A. Walmsley, *Managing photons for quantum information processing*, *Philosophical Transactions of the Royal Society of London A*, **361**, pp. 1493–1506 (2003).
- [146] R. S. Bennink, Y. Liu, D. D. Earl, and W. P. Grice, *Spatial distinguishability of photons produced by spontaneous parametric down-conversion with a focused pump*, *Physical Review A*, **74**, p. 23802 (2006).
- [147] A. Dragan, *Efficient fiber coupling of down-conversion photon pairs*, *Physical Review A*, **70**, 053814 (2004).
- [148] D. Ljunggren and M. Tengner, *Optimal focusing for maximal collection of entangled narrow-band photon pairs into single-mode fibers*, *Physical Review A (Atomic, Molecular, and Optical Physics)*, **72**, 062301 (2005).
- [149] Y. H. Kim and W. P. Grice, *Measurement of the spectral properties of the two-photon state generated via type II spontaneous parametric downconversion*, *Optics Letters*, **30**, pp. 908–910 (2005).
- [150] R. H. Brown and R. Q. Twiss, *Correlation between photons in two coherent beams of light*, *Nature*, **177**, pp. 27–29 (1956).
- [151] A. L. Cauchy, *Cours d'analyse de l'École Royale Polytechnique, 1ère partie: Analyse algébrique* (1821).
- [152] P. Grangier, G. Roger, and A. Aspect, *Experimental Evidence for a Photon Anticorrelation Effect on a Beam Splitter: A New Light on Single-Photon Interferences*, *Europhysics Letters (EPL)*, **1**, pp. 173–179 (1986).
- [153] A. Joobeur, B. E. A. Saleh, T. S. Larchuk, and M. C. Teich, *Coherence properties of entangled light beams generated by parametric down-conversion: Theory and experiment*, *Physical Review A*, **53**, pp. 4360–4371 (1996).
- [154] A. B. U'Ren, C. Silberhorn, J. L. Ball, K. Banaszek, and I. A. Walmsley, *Characterization of the nonclassical nature of conditionally prepared single photons*, *Physical Review A*, **72**, p. 21802 (2005).
- [155] W. P. Grice, *Interference and Indistinguishability in Ultrafast Spontaneous Parametric Downconversion*, Ph.D. thesis, University of Rochester (1997).

- [156] J. Lee, M. S. Kim, and C. Brukner, *Operationally Invariant Measure of the Distance between Quantum States by Complementary Measurements*, Physical Review Letters, **91** (2003).
- [157] R. P. Feynman, R. B. Leighton, and M. Sands, *The Feynman Lectures on Physics*, Addison-Wesley, Reading, MA (1965).
- [158] M. Xiao, L.-A. Wu, and H. J. Kimble, *Precision Measurement beyond the Shot-Noise Limit*, Physical Review Letters, **59**, pp. 278–281 (1987).
- [159] Z. Y. Ou, *Fundamental quantum limit in precision phase measurement*, Physical Review A, **55**, pp. 2598–2609 (1997).
- [160] P. Walther, J.-W. Pan, M. Aspelmeyer, R. Ursin, S. Gasparoni, and A. Zeilinger, *De Broglie wavelength of a non-local four-photon state*, Nature, **429**, pp. 158–161 (2004).
- [161] M. W. Mitchell, J. S. Lundeen, and A. M. Steinberg, *Super-resolving phase measurements with a multiphoton entangled state*, Nature, **429**, pp. 161–164 (2004).
- [162] P. Walther, M. Aspelmeyer, and A. Zeilinger, *Heralded generation of multiphoton entanglement*, Physical Review A, **75**, 012313 (2007).
- [163] M. P. Almeida, F. de Melo, M. Hor-Meyll, A. Salles, S. P. Walborn, P. H. S. Ribeiro, and L. Davidovich, *Environment-Induced Sudden Death of Entanglement*, Science, **316**, pp. 579–582 (2007).
- [164] C. H. Bennett, H. J. Bernstein, S. Popescu, and B. Schumacher, *Concentrating partial entanglement by local operations*, Physical Review A, **53**, pp. 2046–2052 (1996).
- [165] J. Eisert, S. Scheel, and M. B. Plenio, *Distilling Gaussian States with Gaussian Operations is Impossible*, Physical Review Letters, **89**, p. 137903 (2002).
- [166] T. Opatrný, G. Kurizki, and D.-G. Welsch, *Improvement on teleportation of continuous variables by photon subtraction via conditional measurement*, Physical Review A, **61**, p. 032302 (2000).
- [167] S. Olivares, M. G. A. Paris, and R. Bonifacio, *Teleportation improvement by inconclusive photon subtraction*, Physical Review A, **67**, p. 032314 (2003).
- [168] P. G. Kwiat, S. Barraza-Lopez, A. Stefanov, and N. Gisin, *Experimental entanglement distillation and ‘hidden’ non-locality*, Nature, **409**, pp. 1014–1017 (2001).
- [169] J.-W. Pan, S. Gasparoni, R. Ursin, G. Weihs, and A. Zeilinger, *Experimental entanglement purification of arbitrary unknown states*, Nature, **423**, pp. 417–422 (2003).

- [170] A. Ourjoumtsev, A. Dantan, R. Tualle-Brouiri, and P. Grangier, *Increasing Entanglement between Gaussian States by Coherent Photon Subtraction*, Physical Review Letters, **98**, 030502 (2007).
- [171] D. E. Browne, J. Eisert, S. Scheel, and M. B. Plenio, *Driving non-Gaussian to Gaussian states with linear optics*, Physical Review A, **67**, p. 062320 (2003).
- [172] J. Eisert, M. B. Plenio, D. E. Browne, S. Scheel, and A. Feito, *On the experimental feasibility of continuous-variable optical entanglement distillation*, arXiv preprint quant-ph/0604163 (2006).
- [173] D. Achilles, C. Silberhorn, C. Sliwa, K. Banaszek, and I. Walmsley, *Fiber-assisted detection with photon number resolution*, Optics Letters, **28**, pp. 2387–2389 (2003).
- [174] K. Garay-Palmett, H. J. McGuinness, O. Cohen, J. S. Lundeen, R. Rangel-Rojo, M. G. Raymer, C. J. McKinstrie, S. Radic, A. B. U'Ren, and I. A. Walmsley, *Photon pair state preparation with tailored spectral properties by spontaneous four-wave mixing in photonic-crystal fiber*, Accepted for publication in Optics Express (2007).
- [175] M. G. Raymer, J. Noh, K. Banaszek, and I. A. Walmsley, *Pure-state single-photon wave-packet generation by parametric down-conversion in a distributed microcavity*, Physical Review A, **72**, 023825 (2005).
- [176] G. D. Emmerson, S. P. Watts, C. B. E. Gawith, V. Albanis, M. Ibsen, R. B. Williams, and P. G. R. Smith, *Fabrication of directly UV-written channel waveguides with simultaneously defined integral Bragg gratings*, Electronics Letters, **38**, pp. 1531–1532 (2002).
- [177] J. S. Koo, R. B. Williams, C. B. E. Gawith, S. P. Watts, G. D. Emmerson, V. Albanis, P. G. R. Smith, and M. C. Grossel, *UV written waveguide devices using crosslinkable PMMA-based copolymers*, Electronics Letters, **39**, pp. 394–395 (2003).
- [178] S. Mailis, C. Riziotis, I. T. Wellington, P. G. R. Smith, C. B. E. Gawith, and R. W. Eason, *Direct ultraviolet writing of channel waveguides in congruent lithium niobate single crystals*, Optics Letters, **28**, pp. 1433–1435 (2003).